ADIABATIC PULSE PREPARATION FOR IMAGING IRON OXIDE

NANOPARTICLES

A Dissertation
Presented to
The Academic Faculty

by

Steven S. Harris

In Partial Fulfillment
of the Requirements for the Degree
Doctor of Philosophy in the
School of Biomedical Engineering

Georgia Institute of Technology
May 2012

ADIABATIC PULSE PREPARATION FOR IMAGING IRON OXIDE NANOPARTICLES

Approved by:

Dr. Xiaoping Hu, Advisor
School of Biomedical Engineering
Georgia Institute of Technology

Dr. Hui Mao
Department of Radiology
Emory University

Dr. Gang Bao
School of Biomedical Engineering
Georgia Institute of Technology

Dr. Diego Martin
Department of Radiology
University of Arizona

Dr. Shella Keilholz
School of Biomedical Engineering
Georgia Institute of Technology

Date Approved: January 3, 2012

To Don, Amy, Kathy, and Meghan

ACKNOWLEDGEMENTS

First, I would like to thank my dissertation committee for their direction and support of this work. Obviously, Dr. Xiaoping Hu was a tremendous influence as a scientific mentor, and Drs. Diego Martin, Hui Mao, Shella Keilholz and Gang Bao provided wonderful insight, in addition to being available for the defense at the drop of a hat.

While all the current and past BITC members contributed to the great educational and social environment, I would like to specially acknowledge a few that made a personal impact: Govind Bhagavatheeshwaran, Cameron Craddock, Chris Glielmi, Katrina Gourdet, Keith Heberlein, Andy James, Roger Nana, Stephen LaConte, Jaekeun Park, Daniel Perez, Nashiely Pineda, Alexander Poplawsky, Brenda Robledo, Priya Santhanam, Jaemin Shin, Qin Xu, Xiaoyong Zhang, and Lei Zhou. Additionally, Xing Lv, Wen Song, Jing Wang, and Yue Zhang contributed invaluably to my research and wonderful experience in China, and I hope we will remain long distance friends. Also, Mary Horton and the Emory MD/PhD program were constant sources of guidance and support.

Finally, by far the greatest sources of support were my family: my wife, Meghan, my sister, Kathy, and mom and dad, Don and Amy.

TABLE OF CONTENTS

LIST OF FIGURES

LIST OF ABBREVIATIONS

AFP	Adiabatic full passage
AZP	Adiabatic zero passage
BW	Bandwidth
CT	Computed tomography
D	Diffusion constant
dB	Decibel
fMRI	Functional magnetic resonance imaging
FOV	Field of view
G	Gauss
GE	Gradient echo
HASTE	Half-Fourier acquisition single shot turbo spin-echo
Hz	Hertz
kHz	Kilohertz
mM	Millimolar
MR	Magnetic resonance
MRI	Magnetic resonance imaging
nm	Nanometer
RF	Radio frequency
SAR	Specific absorption ratio

SE	Spin echo
SPIO	Superparamagnetic iron oxide
T	Tesla
TE	Echo time
TF	Turbo factor
TR	Repetition time
TSE	Turbo spin echo
TSE	Turbo Spin Echo
US	Ultrasound
UTE	Ultrashort echo time

LIST OF SYMBOLS

$\vec{\mu}$	Magnetic moment
.	Dot product of vectors
a	Particle radius
B_0	Static magnetic field
B_1	Radio frequency magnetic field
B_{eff}	Effective magnetic field in rotating frame
M_0	Equilibrium magnetization
M_t	Transverse magnetization
M_x, M_y, M_z	Magnetization vector components
M_z	Longitudinal magnetization
r	Distance from particle center
R_1	Longitudinal relaxation rate
R_2	Transverse relaxation rate
t	Time
T_1	Longitudinal relaxation time
T_2	Transverse relaxation time
T_2*	T_2 star
T_E	Echo time
T_R	Repetition time

x′, y′, z′	Rotating frame axes
x, y, z	Laboratory frame axes
$\Delta\chi$	Susceptibility change
α	Flip angle
ϕ	Phase angle
γ	Gyromagnetic ratio
θ	Rotation angle
τ	Pulse duration
ω_0	Angular frequency of precession
ω_1	Applied radio frequency

SUMMARY

Iron oxide nanoparticles are of great interest as contrast agents for research and potentially clinical molecular magnetic resonance imaging (MRI). Biochemically modifying the surface coatings of the particles with proteins and polysaccharides enhances their utility by improving cell receptor specificity, increasing uptake for cell labeling and adding therapeutic molecules. Together with the high contrast they produce in MR images, these characteristics promise an expanding role for magnetic nanoparticles and molecular MR imaging for studying, diagnosing and treating diseases at the molecular level. However, these contrast agents produce areas of signal loss with traditional MRI sequences that are not specific to the nanoparticles and cannot easily quantify the contrast agent concentration. With the expanding role of magnetic nanoparticles in molecular imaging, new methods are needed to produce a quantitative contrast that is specific to the magnetic nanoparticle.

This dissertation presents a new method for detecting and quantifying iron oxide nanoparticles using an adiabatic preparation pulse. It is shown through numerical simulation and experimental results that the adiabatic condition fails for spins diffusing near the particles, leading to a change in the image intensity that is proportional to the particle concentration. Importantly, the adiabatic contrast is linearly correlated with the total iron concentration, making it ideal for quantitative molecular imaging. Further, it is

shown that the contrast is not very sensitive to inhomogeneities in the magnetic fields or magnetization transfer. This contrast was confirmed using 3 Tesla and 9.4 Tesla MR scanners, highlighting the translational potential of the approach for examinations and scientific research at clinical and ultra-high magnetic field strengths.

In the first aim, the theoretical foundation of the work is presented and a Monte Carlo simulation supporting the proposed mechanism of the contrast is described. Adiabatic pulse prepared imaging sequences are also developed for imaging at 3 Tesla and 9.4 Tesla, and the ability of the method to visualize and quantify the contrast is confirmed. Further, the physical characteristics of the nanoparticles and the preparation pulse and sequence parameters are modified to further characterize the approach. In the second aim, the contrast is characterized in more realistic phantoms, and a method to more accurately quantify nanoparticle concentration in the presence of magnetization transfer is presented. The sensitivity of the adiabatic contrast quantification to inhomogeneities in the magnetic fields and modifications to the pulse sequence parameters is also characterized. Finally, accelerated imaging methods are implemented to acquire the adiabatic contrast in a time compatible with *in vivo* imaging, and the technique is evaluated in several models of cellular and *in vivo* quantitative iron oxide nanoparticle imaging. Together, these aims present a method using an adiabatic preparation pulse to generate an MR contrast based on the microscopic magnetic field gradients surrounding the iron oxide nanoparticles that is suitable for *in vivo* quantitative, molecular imaging.

CHAPTER 1

INTRODUCTION

1.1 General Introduction

The use of Magnetic Resonance Imaging (MRI) for human disease diagnosis and monitoring has rapidly expanded over the past decades as a non-invasive, high resolution imaging modality. One of the greatest advantages of MRI is the ability to manipulate the pulse sequence to produce images sensitive to many different factors that can help physicians differentiate cancerous and non-cancerous lesions, for example. While MRI provides rich information from these changes in the tissue molecular environment, pertinent questions such as the number or presence of cancer signaling receptors on a cell surface cannot be asked with conventional imaging methods. Molecular MRI promises greater specificity and sensitivity than conventional MRI by producing images sensitive to specific molecules and using contrast agents to target specific cellular environments. These probes can either be endogenous contrast agents such as molecules or complexes made by the tissue of interest, or exogenous contrast agents that are administered to the subject to enhance a specific tissue. In either case, molecular contrast agents allow clinicians and researchers to visualize biomarkers of disease *in vivo*. The overall goal of this work is to diagnosis disease earlier with higher specificity, to monitor disease progression or treatment and to inform treatment decisions.

Iron oxide nanoparticles are one type of exogenous contrast agent that can be administered to subjects *in vivo* to provide contrast in magnetic resonance (MR) images. These agents have been of intense research interest because they provide strong contrast in MR images, have surface coatings that can be modified for targeting to a specific biomolecular environment, and are largely biocompatible *in vivo*. While most of these studies are currently aimed at animal systems, there is hope that these approaches can eventually be translated into the clinical setting. In developing methods for molecular MR there are two parallel tracts: developing the contrast agents and developing the methods to detect the agents with MRI. As previous emphasized, an MR image is a function of dozens of parameters that affect the physics in the tissue and change the image intensity. The presence of a contrast agent in a tissue is not sufficient to provide useful information for the researcher or clinician; choosing the appropriate pulse sequence is essential for interpreting the image contrast. Together, these parallel lines of research are expanding the ability of MRI to characterize a subject at all levels from diffusion, to function, to molecule, to anatomy.

1.2 Statement of Thesis

In this dissertation a new mechanism for detecting and quantifying iron oxide nanoparticles is presented. While this method adds to a number of methods for generating MR contrast from nanoparticles, generating contrast based on the microscopic environment of the particles has specific advantages that will be discussed. Additionally, the linear correlation of the contrast with iron oxide nanoparticle concentration is of particular note, as this straightforward relationship is of great importance for quantitative

molecular imaging. First, the theory underlying the method is presented along with numerical simulations and experimental results. Second, the technique is applied to more realistic phantoms and *in vitro* studies showing how the properties and parameters of the pulse sequence can be modified to increase the sensitivity and specificity of the quantification. Finally, *in vivo* studies are presented suggesting that the technique can be extended to animal, and eventually human, models of molecular MR. The accomplishment of these aims establishes and optimizes a new mechanism using adiabatic preparation pulses to detect and quantify iron oxide nanoparticles using MR imaging.

1.2.1   Developing a Technique for Imaging Iron Oxide Nanoparticles with
Adiabatic Pulse Preparation

As researchers develop an increasing number of iron oxide nanoparticle based contrast agents with increasing molecular and disease specificity, new mechanisms to detect and quantifying these contrast agents with complementary sensitivity and specificity are required. In this chapter, the theory of the adiabatic pulse prepared technique for imaging iron oxide nanoparticles is introduced. In order to characterize the mechanism, a Monte Carlo simulation is also developed suggesting that the failure of the adiabatic condition in the region surrounding the nanoparticle may be used as a contrast mechanism. The simulation results are confirmed by experiments on both clinical and research MR scanners, and the pulse parameters are modified suggesting approaches to

modulate the sensitivity and specificity of the contrast. This work presents a new contrast approach that is linearly increasing with increasing nanoparticle concentration and is appropriate for quantitative molecular MR.

1.2.2   Characterizing the Adiabatic Contrast in Phantoms and *In Vitro*

While numerical simulations and nanoparticles in solution present interesting results, in order to be applicable to *in vivo* models the quantitative characteristics of the method must be maintained in diverse molecular environments. In this chapter, the proposed method is extended to more realistic molecular environments, and a method to compensate for confounding magnetization transfer effects is developed. The robustness of the contrast is also characterized by investigating its sensitivity to changes in the molecular environment. Additionally, the sensitivity of the contrast to changes in the diffusion rate is characterized, and the ability of the method to quantify iron oxide nanoparticle labeled cells is demonstrated. Finally, the method is compared to other methods for detecting and quantifying nanoparticles, and its complementary role is emphasized. Here, the adiabatic pulse prepared method is shown to be insensitive to a number of factors that confound other methods of quantifying particles and applicable to models of endogenous and exogenous cellular imaging.

1.2.3   Investigating Adiabatic Contrast *In Vivo*

In the final aim, the contrast mechanism is extended to be applicable to *in vivo* models of molecular imaging. First, the general applicability of the technique is greatly aided by implementing accelerated image acquisition schemes that dramatically reduce the total imaging time without sacrificing image contrast. Finally, a model of *in vivo* animal imaging following iron oxide nanoparticle accumulation in the mouse liver is used to validate the linear correlation of image contrast with liver iron concentration measured *ex vivo*. The results show that the adiabatic pulse prepared contrast technique is suitable for *in vivo* imaging and remains a viable quantitative imaging method.

1.3 Background

1.3.1   Magnetic Resonance Imaging

Today MRI is a rapidly growing tool aiding clinical diagnosis around the world, but its basis if firmly planted in the discoveries of spectral line splitting by Zeeman (1) and nuclear magnetic resonance (2, 3) many decades ago. However, it was not until Lauterbur (4) and Mansfield and Grannell (5) that these discoveries were combined with methods to spatially localize the NMR signal that MR images were formed. Today, the numerous diseases and applications studied by MRI are a testament to the flexibility of

the underlying physics to provide diagnostic information safely and non-invasively. In this brief introduction, the origin of the MR signal will be defined as well as the effect of applied radiofrequency (RF) pulses and contrast agents. The following work applies these concepts to a specific application of adiabatic preparation pulses and iron oxide nanoparticles.

Hydrogen nuclei are ubiquitous throughout the body as the building blocks of water. These nuclei are very important for MRI because they possess the fundamental property of nuclear spin 1/2 due to their unpaired proton and no neutrons. This means that when placed in an external magnetic field, B_0, the spin precess about the external field at a frequency proportional to the static field, B_0, and the gyromagnetic ratio, γ, of the nuclei (all equations in this chapter from (6)):

$$\omega_0 = \gamma B_0 \qquad (1.1)$$

However, we cannot detect the magnetization vector until it is rotated into the plane perpendicular to the external magnetic field where it can be detected by receiver coils. This relationship can be elegantly reduced to the equation of motion for a magnetic moment:

$$\frac{d\vec{\mu}}{dt} = \gamma \vec{\mu} \times \vec{B} \qquad (1.2)$$

By adding a second magnetic field perpendicular to the B_0 field, the spin can be rotated from its current position. Here we can simplify the mathematics by introducing a primed coordinate systems that rotates with the external magnetic field. It can further be derived that the rotation of the magnetic moment is a function of the effective applied magnetic field:

$$\left(\frac{d\vec{\mu}}{dt}\right)' = \gamma\vec{\mu} \times \vec{B}_{eff} \qquad (1.3)$$

By defining the frequencies of the spins based on equation 1.1 and the static magnetic field, ω_0, the rotating magnetic field, ω, and the frequency of the applied magnetic field, ω_1, the effective magnetic field for the MRI experiment can be defined:

$$\vec{B}_{eff} \equiv \frac{\hat{z}'(\omega_0-\omega)+\hat{x}'\omega_1}{\gamma} \qquad (1.4)$$

For most MR experiments the applied field is selected to be equal to the Larmour Frequency of the precessing spins, $\omega = \omega_0$. However this does not necessarily have to be the case, as will be shown for the adiabatic passage that is the primary interest in this dissertation.

Once an RF pulse rotates a spin system into the transverse plane the spins begin to precess about the static magnetic field, producing a magnetic flux through the receiver coil which in turn induces a current and a signal measurement. If each spin started with the same initial phase in a homogeneous magnetic field we would expect their phases

7

relative to one another to remain constant, since each spin would be precessing at exactly the same frequency. However, the magnetic field is never exactly homogenous. The accumulated phase at position r can be defined as:

$$\emptyset(\vec{r}, t) = -\gamma\left(B_0 + \Delta B(\vec{r})\right)t \qquad (1.5)$$

Thus, the addition of a magnetic field component that varies in space and time produces different phase accumulations over the region of interest. The greater the variation in the magnetic field or the longer the time that the phases accumulate, the greater the phase difference between two subsets of spins.

Additionally, after the magnetization vector has been rotated from the longitudinal direction into the transverse plane it will relax back towards its original state. If we simply consider the case where the entire longitudinal magnetization was tipped into the transverse plane, the recovery of the longitudinal magnetization can be given as:

$$M_z(t) = M_0\left(1 - e^{-t/T_1}\right) \qquad (1.6)$$

For this case, the recovery of the system is described by the time constant T_1, or the "spin-lattice" relaxation time. A second parameter related to the dephasing of the spins is the transverse relaxation time constant T_2, or the "spin-spin" relaxation. Here again, if the magnetization is tipped into the transverse plane at time, $t = 0$, and if the signal is refocused at an echo time TE:

$$M_+(T_E) = M_0 \left(1 - e^{-T_R/T_1}\right) e^{-T_E/T_2} \qquad (1.7)$$

Differential tissue relaxation rates, along with variations in spin densities, cause different tissues to have different intensities within a single MR image. In fact, it was recognized early in development of MRI that cancerous tissue may be distinguished from healthy tissue (7). Therefore, informed by the different properties of the tissue, pulse sequences can be designed to accentuate or quantify changes in the relaxation rates (8). While these tissue differences act as endogenous contrast, MR imaging is not limited to native tissue contrast. Exogenous contrast agents can be designed with these same physical principles in mind to aid in tissue characterization (9).

1.3.2 Contrast Agents for Molecular Magnetic Resonance Imaging

While MRI provides exquisite soft tissue contrast, simply due to changes in spin density and relaxation rates, contrast agents can add information based on the underlying cellular biology and physiology to which MR is not otherwise sensitive (10-12). These contrast agents can either be exogenously administered to the subject where they differentially accumulate to highlight a tissue of interest (13, 14), or they can be endogenously produced by the tissue either where their role as a contrast agent is secondary to their biological role, or as a reporter gene where their expression is controlled at the genetic level (15-17). Perhaps the most broadly applied endogenous

9

contrast is deoxyhemoglobin, where its correlation with neural activation is the basis for functional magnetic resonance imaging (fMRI) (18) and the dynamic mapping of brain activity (19). However, for molecular imaging most contrast agents are developed in the laboratory.

The overall goal of a molecular MR contrast agent is to affect the MR signal in an area based on low concentrations of a molecular target or small changes in the biochemical environment (20). While ultrasound agents affect sound reflection (21) and computed tomography uses changes in density (22), MR contrast agents often change the relaxation rates of the surrounding molecules (23). As previously described, changes in the longitudinal relaxation rate ($1 / T_1$) and transverse relaxation rate ($1 / T_2$) affect the measured MR signal. T_1 agents that increase the relaxation rate generally lead to an increase in signal on T_1 weighted images, while T_2 agents that increase the transverse relaxation rate lead to a decrease in signal in T_2-weighted images. Two of the most studied MR contrast agents are gadolinium and magnetic nanoparticles.

Gadolinium is a rare earth metal that is the most widely used paramagnetic contrast agent in the clinical setting since its application to cerebral brain tumors (24). Today, clinical applications of gadolinium include cardiac (25), vessel (26) and hepatic imaging (27). While gadolinium-based contrast agents have previously been associated with the development of nephrogenic systemic fibrosis in patients (28), more recent studies have shown a dramatic decrease in the complication rate by changing the type and method of contrast administration (29). An additional concern for molecular imaging is

the potential for gadolinium to effect cellular processes (30). However, gadolinium is still an essential part of many clinical exams, and since it is primarily a T_1 contrast agent, it produces increased signal intensity in T_1-weighted MR images. When used as a positive contrast agent it can be detected in the micromolar concentrations applicable to molecular imaging (31)

While the T_1 agents maintain inherent imaging advantages, T_2 agents such as iron oxide nanoparticles may have greater potential for molecular imaging. One natural advantage of iron-based contrast agents is that iron is a ubiquitous element in the body that plays an important chemical role in many oxidation-reduction reactions, and therefore cells have pathways for degrading iron into the hemoglobin pool (32). Biocompatibility studies in animals (33) and clinical experiences in humans (34) have lead to the clinical approval of an iron oxide as a contrast agent for hepatic imaging (35). Even without surface modifications to target the particles to specific cell receptors, circulating iron oxide nanoparticles provide useful information on the tissue molecular environment. This passive targeting results in image contrast based on nanoparticle uptake by immune cells present in healthy liver tissue but absent in cancerous tissue (36), accumulation of particles in normal lymph nodes (37, 38), and escape of nanoparticles from leaky tumor tissue vasculature (39).

While there is a broad range of molecular contrast agents, exogenous iron oxide nanoparticles are the most widely studied (40). Since these superparamagnetic iron oxide (SPIO) contrast agents have a significantly greater effect on the transverse relaxation rate

compared to the longitudinal relaxation rate, these agents produce a negative contrast that is difficult to localize and quantify. While SPIO nanoparticles have a measurable effect on the longitudinal relaxation rate, especially with ultrashort echo time imaging (41), changes in T_2^* and T_2 have been more widely applied (42). The effect of these contrast agents on the images is related to the size, composition and concentration of the nanoparticles.

The iron oxide core and surrounding coating combine to determine the tissue specificity and effect on the MR signal (43). Most nanoparticles have cores composed of magnetite (Fe_3O_4) and/or maghemite (γFe_2O_3) that have saturation moments of 127 emu/g Fe and 78 emu/g Fe respectively (44). While numerous methods have been developed to manufacture these iron oxide nanoparticles (14), coprecipitation of Fe(II) and Fe(III) under specific conditions is the most common (45). While the particles can be manufactured over a range of a few nanometers (46) to several microns (47), for *in vivo* applications the size range is limited by its interaction with the body. Generally, particles smaller than 7-10 nm are filtered through the kidney glomerulus where they are excreted in the urine (48, 49), while particles larger than 100 nm have an increased likelihood of being removed from circulation in the liver and spleen by the reticuloendothelial system (50).

In addition to the physiological advantages of this mid-size range, particles with diameters of 2 to 20 nm can be superparamagnetic. This means that while their

magnetization flips randomly in the absence of an external magnetic field (44), when an external magnetic field is applied, the magnetic moment quickly aligns with the direction of the applied magnetic field, and the saturation magnetization is achieved (51). These properties make the particles extremely useful in the MR experiment where the static magnetic field induces these changes and produces dramatic contrast given their small size.

An equally important part of the nanoparticle is the coating of the iron oxide core. The surface coating allows for particle stability in the aqueous environment of the body as well as providing a platform for surface modifications, including proteins and polysaccharides that can be added to target the particles to a specific molecular environment (52, 53). The primary particle coating is dextran (54), a polysaccharide of glucose, that increases the circulation time of the particles (55) while decreasing the chance of undesirable uptake by the immune system (56). Additionally, the coating can be modified to affect the relaxivity of the particle (57, 58). Combined, these changes make the surface coating of the particle a key modulator of the spatial localization of the particles and their affect on the MR signal.

Iron oxide nanoparticles produce contrast in MR images by creating inhomogeneities in the magnetic field. The magnetic nanoparticle changes the surrounding magnetic field where the spins contributing to the MR signal are located. For a spherical iron oxide nanoparticle, the change in the external magnetic field can be described by (59):

$$\Delta B_z = \frac{\Delta x B_0 a^3}{3} \left(\frac{a}{r}\right)^3 (3cos^2\theta - 1) \hspace{2cm} (1.8)$$

Where $\Delta\chi$ is the change in susceptibility, B_0 the external magnetic field, a the particle radius, θ the angle in spherical coordinates, and r the distance from the particle center. From this equation, it can be seen that the local magnetic field changes based on the physical properties of the nanoparticle (magnetic susceptibility and particle size) and spatial location (distance and orientation to the particle). Figure 1.1 shows that when these effects are plotted, the dipolar field extends well beyond the physical boundaries of the particle.
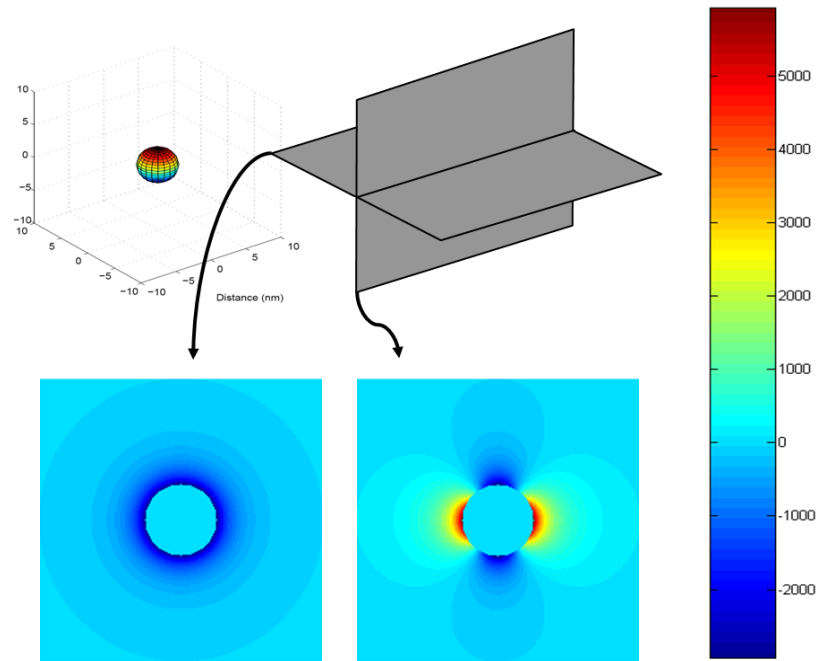
Figure 1.1: Iron-oxide nanoparticle of 4.8 nm diameter frequency change distribution (Hz)

With the colorbar on the right of Figure 1.1 showing the range of frequency change in the region surrounding the particle, the origin of the T_2-weighted contrast becomes apparent. As different spins precess at different frequencies they accumulated phase differences that lead to a decrease in phase coherence and a decrease in signal with increasing time. As the magnitude of the inhomogeneities or the number of nanoparticles increases, the signal intensity on T_2-weighted imaging decreases. However, this does not mean that there must be a decrease in image intensity for every MR sequence when iron oxide nanoparticles are present. As will be shown, by knowing the effects of the magnetic nanoparticles on their surroundings, schemes can be developed to enhance signal from the region surrounding the nanoparticle compared to the background.

1.3.3   Adiabatic Pulses

Adiabatic pulses are amplitude and phase modulated RF pulses that can be implemented on clinical and research MR scanners (60). Pulses modulated in phase (or frequency) were common in early NMR experiments where excitation was accomplished by sweeping the effective magnetic field in the presence of continuous wave RF irradiation (61). However, MR systems today are engineered to provide a uniform, static main magnetic field. In practice, the adiabatic passage is accomplished by modulating the amplitude and phase of an RF pulse in the presence of a constant main magnetic field.

One practical advantage of adiabatic pulses is that they are very insensitive to the homogeneity of the B_1 field, and these pulses are often used to produce uniform excitation and inversion pulses (62, 63). However, this uniformity comes at the expense of limiting the applications of adiabatic pulses compared to conventional RF pulses. For example, the rotation of the magnetization does not have the same relationship between power and time as a conventional pulse. In the case of a pulse applied at the Larmor frequency along an axis in the transverse plane, the resulting flip angle is defined by:

$$\theta = 2\,\pi\,\gamma\,\tau\,B_1 \tag{1.9}$$

Where τ is the duration and B_1 is the magnitude of the applied magnetic field. By this equation the duration and power of the pulse can be changed to produce not only an excitation, inversion, or refocusing pulse, but any intermediate flip angle can be achieved with the appropriate local parameters.

An adiabatic full passage pulse rotates the effective applied magnetic field and the magnetization 180 degrees provided the adiabatic condition is fulfilled (64). In order to explain how this occurs, a coordinate system is defined that rotates with the applied magnetic field (65). In Figure 1.2 the main magnetic field is aligned with the z' direction, and before the pulse is applied the magnetization precesses about the z' axis. For a conventional RF pulse applied at the Larmor frequency, the B_1 field would be applied in the transverse plane, and the magnetization would rotate about that direction. However, if a pulse begins off resonance, in the rotating frame this corresponds to a component along

16

the z′ direction – parallel with the magnetization vector. The magnitude of this vector is proportional to the distance off-resonance, so as the frequency approaches the on-resonance condition this magnitude diminishes. The second component is the magnitude of the applied magnetic field, which by vector summation forms the effective magnetic field vector.
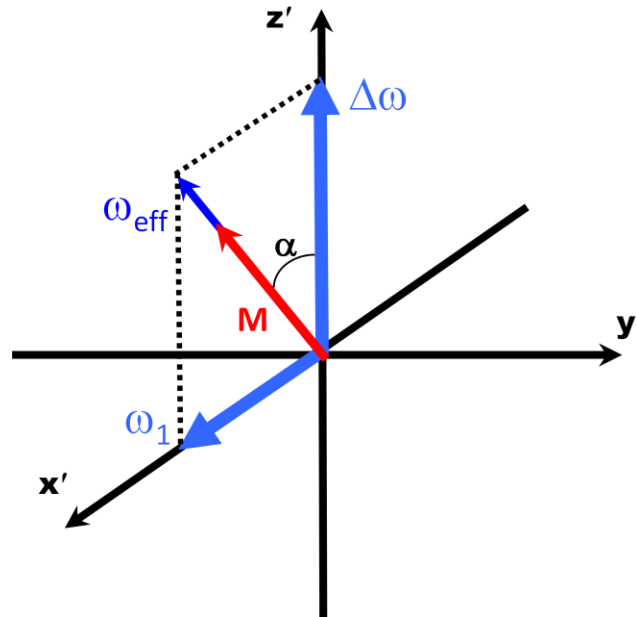
Figure 1.2: Spin follows the effective magnetic field during the adiabatic passage

When the adiabatic pulse begins far from resonance with a small magnitude relative to the off resonance, the magnetization and the effective applied field begin parallel, and the magnetization precesses about the applied magnetic field. Figure 1.2 shows that by modulating the frequency and amplitude of the adiabatic pulse, the magnetization follows the applied field as it rotates from its initial orientation. Many

methods for performing the adiabatic passage have been developed and optimized (66-70), but one of the most common adiabatic pulses is the hyperbolic secant pulse defined by the following amplitude and frequency modulation (64):

$$B_1(t) = B_1^0 \text{sech}\,(\beta t) \qquad\qquad (1.10)$$

$$\Delta\omega(t) = -\mu\beta\text{tanh}\,(\beta t) \qquad\qquad (1.11)$$

Here, β and µ define the bandwidth of the pulse frequency sweep. Figures 1.3 and 1.4 show the amplitude and phase modulation of a hyperbolic secant pulse. The bandwidth, as included in the phase modulation, can be optimized for the desired application. As will be formally described, both the magnitude and range of frequency sweep affect the performance of the pulse and have important implications for the contrast generated.
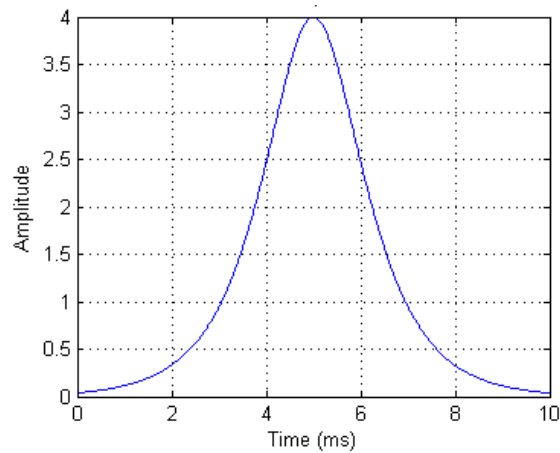
Figure 1.3: RF amplitude modulation of hyperbolic secant pulse
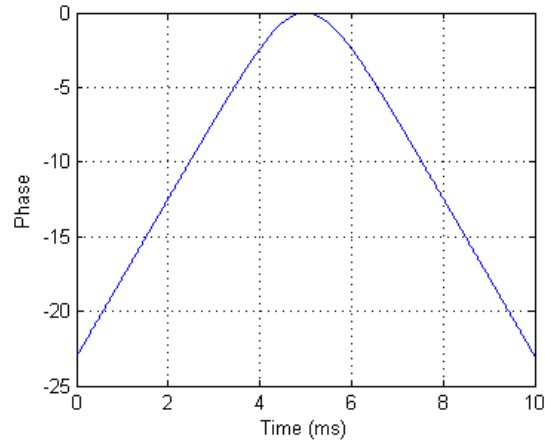
Figure 1.4: RF phase modulation of hyperbolic secant pulse

However, the adiabatic passage only occurs if the pulse rotates slow enough so that the effective magnetic field changes more slowly than the rotation of the magnetization about the effective field (71). This limitation is a function of the acceleration of the field rotation, which can be described by:

$$\alpha(t) = \arctan\left[\frac{\gamma B_1(t)}{\Delta\omega(t)}\right] \qquad (1.12)$$

This equation gives rise to the "adiabatic condition" that must be satisfied for the pulse to perform as desired:

$$\left|\omega_{eff}(t)\right| \gg |d\alpha/dt| \qquad (1.13)$$

19

From this equation we can see that the adiabatic condition may be fulfilled by either increasing the amplitude of B_1 or by decreasing the acceleration of the frequency sweep. The former condition highlights the characteristic of the pulse that once the adiabatic condition is fulfilled, further increases in power will not change the flip angle. As such, these pulses are often used in cases where the B_1 field may be very inhomogeneous, such as in transceiver surface coils (72).

Simulation with the Bloch equation highlights the uniformity and frequency selection of the adiabatic full passage. Figure 1.5 shows that for a pulse with a - / + 5 kHz frequency sweep, near uniform inversion is achieved for spins within this frequency range. For spins outside this range the magnetization remains as it was before the application of the pulse. Additionally, the transition between the two states is narrow and can be modulated by the pulse parameters.
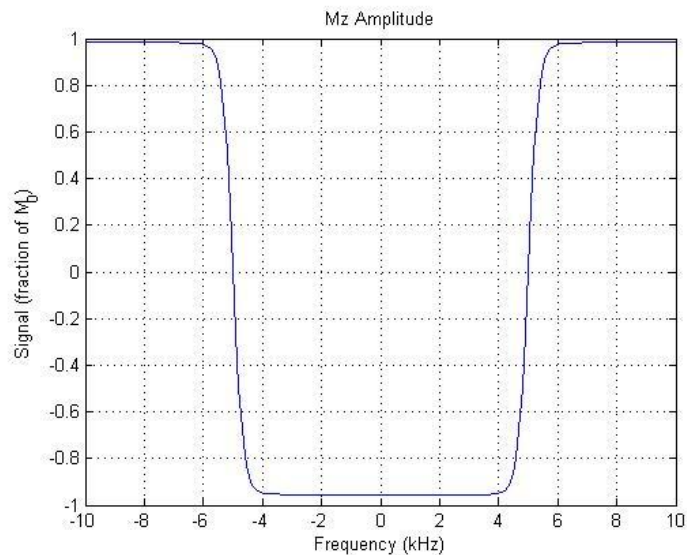
Figure 1.5: Simulated Mz magnetization after adiabatic full passage

20

Figure 1.6 shows the transverse component of the signal, which again demonstrates the ideal behavior of the pulse within the frequency range of the pulse. As will be shown in the following studies, the transition between the range within and outside the frequency sweep produces a variable transverse and longitudinal component. However, the ideal inversion profile for the spins that achieve the adiabatic full passage provides many advantages for developing robust imaging techniques.
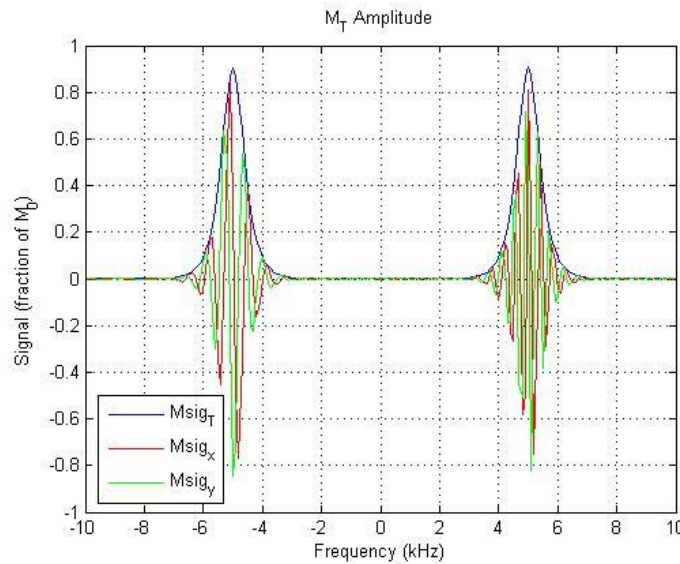
Figure 1.6: Simulated Mt magnetization after an adiabatic full passage

Though their uniformity provides many advantages, one drawback of these pulse is that they are most directly used to produce full (180 degree) and half (90 degree) rotations; however, multiple passages with phase offsets can be used to produce other flip angles (73, 74). While the adiabatic pulse principles have been applied to many MR

techniques including spectroscopy localization (75) and slice selection (76), and continuous labeling of flowing spins (77, 78), the adiabatic passage and the failure of the adiabatic condition has not previously been applied to the detection of iron oxide nanoparticles.

CHAPTER 2

DEVELOPING A TECHNIQUE FOR IMAGING IRON OXIDE NANOPARTICLES WITH ADIABATIC PULSE PREPARATION

Iron oxide nanoparticles have tremendous potential as magnetic resonance imaging (MRI) contrast agents to aid disease detection and treatment monitoring in the research and eventually clinical settings. This chapter introduces a new method for generating contrast from iron oxide nanoparticles using an adiabatic preparation pulse. First, the mechanism is validated with a Monte Carlo simulation, and then the pulse sequence is implemented on clinical and research MR scanners with magnetic field strengths of 3 Tesla and 9.4 Tesla. Images are created to visualize the positive contrast, and the contrast is quantified over a range of iron concentration used in molecular MR imaging. Next, iron oxide nanoparticles with specific core diameters are manufactured to characterize the effect of the physical parameters of the nanoparticles on the adiabatic contrast. Finally, the parameters of the pulse sequence are modulated to characterize the contrast and increase the sensitivity of the technique based on the proposed mechanism. This work represents the first report of the adiabatic pulse prepared contrast mechanism for quantitative iron oxide nanoparticle imaging.

2.1 Introduction

As the number of research applications of iron oxide nanoparticles grows and there is increasing hope that these discoveries will lead to clinical diagnostic tools, sensitive and specific methods for imaging iron oxide nanoparticles will become essential. While a number of methods for producing increased signal from the regions surrounding the particles have emerged, most of these methods rely on changes in the macroscopic magnetic field surrounding the particles. While increased signal alone may hold some advantages for contrast localization, such approaches do not inherently overcome all the challenges to detecting and quantifying the nanoparticles. With this in mind, our goal was to develop a technique for the quantitative imaging of iron oxide nanoparticles that is sensitive to the microscopic magnetic field surrounding the particles. We will show that an adiabatic preparation pulse can be used to produce a signal that is both linearly increasing with increasing iron concentration and sensitive to the local microscopic magnetic field.

While many methods have been able to successfully detect the nanoparticles using MRI, challenges to increasing sensitivity and optimizing quantification remain. One method for increasing the signal from regions containing iron oxide nanoparticles is an approach using unbalanced gradients called the white marker method. In this approach, unbalanced gradients are used to selectively refocus the signal surrounding a region of SPIO nanoparticles using a mechanism similar to that which recovers MR

signal in regions with susceptibility changes in a T2* weighted image (79). Specifically, unlike in a standard imaging sequence where the slice select gradient is completely refocused to maximize signal from excited spins, the white marker method incompletely refocuses the slice selection gradient. As a result, the signal from regions having a homogenous field is suppressed by incomplete refocusing, while the bulk magnetization in some regions inside the SPIO's negative dipolar field achieves a more complete refocusing, producing a brighter signal. While improvements to this technique have been made using positive and negative gradients to decrease the sensitivity to partial volume effects, the region of increased signal intensity extends beyond the localized contrast agent making extension to molecular imaging applications more challenging (80).

Another approach to producing signal from the off-resonance components is to use spectrally selective RF pulses to selectively image the off-resonance spins. In one method a -800 Hz off resonance pulse is used to excite and refocus the spins surrounding iron oxide labeled cell (81). This method is able to manipulate the larger macroscopic magnetic field to produce a dumbbell shaped signal intensity corresponding to a collection of SPIO labeled cells, while the off resonance pulse has little effect on the tissue that does not contain nanoparticles. Also, the slice selectivity of this approach has been updated to address the issues of off-resonance signal from adjacent slices by using self-refocused, spatial-spectral pulses to enhance slice selectivity (82).

Susceptibility mapping is also of growing interest, as a direct measurement of susceptibility may allow for the quantification of elements such as iron and calcium in

addition to exogenous contrast agents (83). Techniques for susceptibility mapping including susceptibility gradient mapping (84) and phase gradient mapping (85) rely on post processing to identify inhomogeneities in the local magnetic field. However, these techniques may be sensitive to the model parameters selected (86) and may not be ideal for quantifying continuous distributions of iron oxide such as in targeted models of cancer imaging (87).

Another method, Inversion-Recovery with ON-Resonant Water Suppression (IRON), uses a spectrally selective RF pulse to saturate the on-resonance magnetization and then image the off-resonance component (88). This method uses a pair of 180 degree pulses with delays for fat-suppression to null the short-T1 component. The sequence then applies a saturating preparation pulse with a 100 Hz bandwidth, a 50 msec duration and an excitation angle of 100 degrees (89). The narrow frequency of the preparation pulse is less effective at saturating the broadened frequency spectrum produced by the presence of the SPIOs as compared to the case of the narrower frequency spectrum in the absence of SPIOs. Following the saturation pulse, a broad-band pulse is used in the imaging sequence to capture the spins that were not saturated by the narrow, on-resonance preparation pulse, and an image is produced with increased signal from the tissue where SPIOs produce a broader frequency spectrum.

While these methods for imaging the off-resonance magnetization produce a positive contrast from the nanoparticles, they rely on the manipulation of the bulk magnetization. Because these mechanisms produce increased signal based on changes in

the macroscopic magnetic field, the quantification of the nanoparticle concentration is based on an area or volume of increased signal in the image (90). Thus, the measure is inherently not spatially specific and does not directly probe the microscopic biological environment. Additional technical challenges include incomplete background suppression due to inhomogeneity in the B_1 field and fat suppression from inhomogeneities in the B_0 field (88).

Next, the off-resonance saturation (ORS) technique uses the microscopic magnetic field inhomogeneities produced by the SPIO nanoparticles to selectively saturate a volume of spins surrounding the nanoparticle (91). In this technique a saturation pulse is applied at a frequency that is offset from water but found in a shell of the dipolar field surrounding the nanoparticle. The method's ability to detect targeted contrast agents in an *in vivo* cancer model demonstrates its low concentration detection limit (92). However, challenges for the technique include sensitivity to the B_0 field homogeneity as changes in the local frequency profile effect the quantification, and the correlation of the contrast with the nanoparticle concentration may not be linear over the range of nanoparticle concentrations used in molecular MR imaging. Finally, several methods of steady state imaging to enhance signal from iron oxide nanoparticles have also been described (93, 94).

While all of these techniques successfully produce signal from the iron oxide nanoparticles, accurate spatial localization and especially nanoparticle quantification remain active research areas. With the adiabatic preparation pulse method, we hope to

add a mechanism for detecting and quantifying iron oxide nanoparticles in phantoms, *in vitro* and *in vivo* that will address these continuing challenges.

2.2 Theory

As was previously described, an iron oxide nanoparticle in a static magnetic field produces a surrounding dipolar magnetic field that introduces inhomogeneities into the otherwise homogeneous magnetic field. While these inhomogeneities increase the transverse relaxation rate, R_2, as spins diffusing through different local magnetic fields loose phase coherence, it has also been shown that spins can be saturated as they diffuse through these microscopic magnetic fields to produce a contrast sensitive to these local changes (91). Since each spin starts at a different location and experiences a different time-varying magnetic field during its random walk diffusing throughout the spatially-varying molecular environment, a contrast sensitive to the diffusion of spins near the particles should be able to detect and quantify the number of nanoparticles. It is hypothesized that an adiabatic preparation pulse can be used to sensitize an image to the presence and concentration of iron oxide nanoparticles.

For pure water with a single resonance frequency, an adiabatic full passage preparation pulse inverts the magnetization according the previously described theory. Provided the pulse applies adequate power and the frequency modulation is sufficiently slow, the magnetization follows the effective magnetic field during its rotation. In this

case, the strength of the effective magnetic field remains much greater than the angular velocity of the applied magnetic field during the entire passage, and thus the adiabatic condition is fulfilled. However, for spins precessing at a frequency that is offset relative to the applied field, the ability of the pulse to rotate these spins is a function of their offset relative to the applied pulse and the frequency sweep (BW) of the adiabatic passage. It can be shown through sweep diagrams that spins within the frequency sweep will be inverted, and those outside the frequency sweep will be returned to their original orientation (95).

However, the presence of iron oxide nanoparticles does not simply create two spin populations: one within the frequency sweep and one outside. Rather, the presence of the magnetic dipoles creates an inhomogeneous molecular environment where spins experience temporally and spatially varying magnetic fields during their continuous diffusion. It is hypothesized that the failure of the adiabatic condition for spins diffusing near the nanoparticles can create a contrast that will allow for the detection and quantification of the particles. The basic concept of this method is presented in Figure 2.1, where the adiabatic passage performs as expected for spins that do not diffuse near the nanoparticles; however, the adiabatic condition fails for spins diffusing near the nanoparticles.
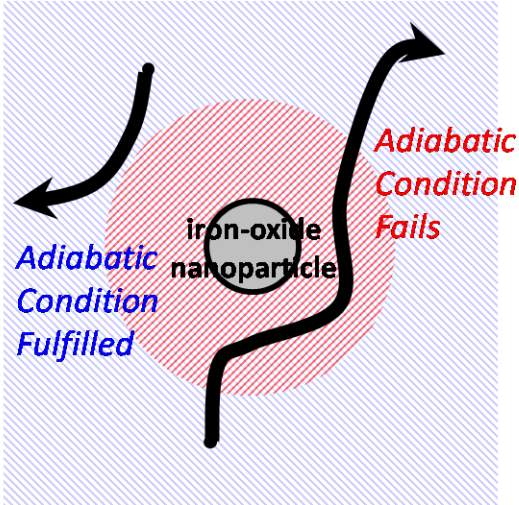
Figure 2.1: Simplified schematic showing the adiabatic contrast hypothesis

As spins diffuse through the rapidly changing magnetic field gradients near the particles, there is a corresponding variation in the effective B_1 that also contributes to the failure of the adiabatic condition. Once the adiabatic condition fails, the spin is no longer locked to the applied field, and the flip angle is defined by the more conventional function of time and B_1 pulse power:

$$\theta(t) = \gamma B_1 t \qquad\qquad (2.1)$$

As a function of time and power, the flip angle for a spin that fails the adiabatic condition is dependent on when the adiabatic passage was abandoned. However, since complete inversion maximizes the magnitude of the M_z magnetization, any other flip angle produces a decrease in the relative M_z magnetization magnitude compared to the complete adiabatic passage. By comparing images acquired with and without the adiabatic preparation pulse, the number of spins failing the adiabatic condition can be

quantified. This measure should be proportional to the concentration of nanoparticles, as the number and volume of local magnetic field gradients producing the contrast is proportional to the number of particles.

Therefore, it is proposed that the rapidly changing local magnetic field gradients near the iron oxide nanoparticles will lead to the failure of the adiabatic condition for spins diffusing near the particles. This failure should be proportional to the number of particles, since there is a direct relationship between the volume of these dipoles and the number of nanoparticles. This approach represents a new method for detecting and quantifying iron oxide nanoparticles based on the failure of the adiabatic condition on the nanometer scale near the particle. Also, since it is not sensitive to a single off resonance frequency the proposed technique should be less sensitive to changes in the macroscopic magnetic field.

2.3 Methods

The primary objectives of this chapter are to *(a)* support the proposed contrast mechanism with numerical simulation, *(b)* demonstrate the visualization and quantification of the adiabatic contrast at clinical and research magnetic field strengths, and *(c)* characterize the contrast produced by changing both the physical properties of the nanoparticles and the parameters of the pulse sequence. While the challenges confronted when imaging nanoparticles in diverse molecular environments, such as *in* vivo, will be

addressed in subsequent chapters, this work focuses on detecting and quantifying nanoparticles in solution.

2.3.1   Monte Carlo Simulation of the Adiabatic Contrast

A Monte Carlo simulation was developed in MATLAB in which spins diffused through a nanoparticle containing environment during the application of an adiabatic RF pulse. Iron concentrations consistent with those used in molecular imaging experiments were first defined, and then the distribution of the nanoparticles in the environment was derived from the assumption of 6070 iron atoms per nanoparticle (96). For the simulation, each spin was randomly assigned an initial spatial position within an environment of equally spaced particles. Then the spins were allowed to diffuse in three dimensions, with the diffusion distance in one dimension, Δ, during a given time-step, τ:

$$\Delta = \sqrt{2 \cdot D \cdot \tau} \qquad\qquad (2.2)$$

In this equation the diffusion constant, D, is assumed to be 2.5 x 10^{-9} m^2 / sec. Assuming a 10 millisecond adiabatic preparation pulse the spins will diffuse an average of 12.2 micrometers in three dimensions. For the simulation, the time step was decreased to 1 nanosecond, which gives an average diffusion distance of 3.9 nm in each dimension. Since increasing the spatial resolution increases the computational power required for the simulation, as well as contributing to the rounding error in the calculation, this resolution

relative to a 6 nm diameter nanoparticle with a one radius length exclusion zone was determined to be sufficient for preliminary studies.

During the diffusion of the spin, a 10 msec hyperbolic secant adiabatic full passage pulse with a -/+ 1000 Hz frequency sweep was applied, and the magnetization was calculated using the Bloch equation. For each time-step the local magnetic field was calculated based on the magnetic field produced by the nearest nanoparticle as well as the contributions to the total magnetic field from the neighboring particles. The maximum B_1 power was chosen to be 0.55459 G for the simulations, the B_1 used in the following phantom experiments at 3 Tesla. The longitudinal magnetization at the conclusion of the pulse was averaged for 500 spins at each iron concentration.

2.3.2 Preparing Sample Nanoparticles

Dilutions of iron oxide nanoparticles in water were prepared at iron concentrations appropriate for molecular imaging. For the initial visualization and quantification experiments Feridex (Advanced Magnetics, Inc., Cambridge, MA) was prepared with a total iron concentration ranging from 0 to 1 mM in a total volume of 1.5 mL. The samples were contained in 2.0 mM polypropylene, round bottom cryogenic vials (Corning Inc., Corning, NY). Due to the discontinuation Feridex manufacture, and the desire to characterize the contrast generated by particles of a narrower diameter, nanoparticles with iron oxide cores of 6.9, 11.0 and 15.0 nm were prepared in the

laboratory of Dr. Gang Bao. Since these particles had greater effects on relaxivity, a lower iron concentration range was chosen between 0 to 0.3 mM which produced transverse relaxation rates comparable to those of the Feridex phantoms.

2.3.3 Imaging at 3 Tesla

An adiabatic pulse prepared spin-echo imaging sequence was implemented within the Siemens IDEA programming environment. The adiabatic preparation pulse was computed in MATLAB based on the duration and frequency sweep desired. For the initial experiments, a 10 millisecond hyperbolic secant pulse with a -/+ 1000 Hz frequency sweep was used. For each subsequent combination of pulse duration and frequency sweep, a new pulse waveform was calculated in MATLAB and the pulse duration was entered on the MR scanner at runtime. All studies where performed on a 3 Tesla Siemens Magnetom Trio (Siemens Medical Solutions, Malvern, PA) using a transmit/receive wrist coil.

The pulse power required for adiabatic passage and the adiabaticity were determined and confirmed experimentally. Water phantoms were used, and the maximum peak power of the adiabatic full passage pulse was increased stepwise. With increasing power, the signal eventually plateaued at a maximum intensity and remained constant as the power was increased beyond this level. This nonconventional relationship of pulse power with flip angle is theoretically expected and confirms that the full passage

inversion was successful. To ensure that the adiabatic condition was fulfilled, the power chosen for the quantification experiments was approximately 20% greater than the power at which the adiabatic condition was fulfilled in the water phantom. Imaging parameters for the phantom experiments at 3 Tesla included: TE: 15 ms, TR: 10s, matrix: 128x128, acquisition time: 21 min, slice = 2 mm, FOV= 70x70 mm.

An adiabatic zero passage preparation pulse was also developed to increase imaging sensitivity. Here, two adiabatic full passage pulses are played back-to-back to return the magnetization to the original orientation. While the frequency sweep of the pulse is identical to the full passage pulse, the duration of the zero passage is twice as long. The increased diffusion time should theoretically increase the likelihood of the adiabatic condition failing, and this approach may increase the sensitivity for detecting very low concentrations of iron oxide nanoparticles.

The adiabatic contrast was quantified by the normalized difference of images acquired with and without the adiabatic preparation pulse. As the adiabatic condition fails for more spins in samples with higher nanoparticle concentrations, a decreased number of the spins are fully inverted, and thus the image intensity is decreased. By subtracting the adiabatic pulse prepared image from the image without the preparation pulse and normalizing it, an adiabatic contrast is defined. All image analyses were performed in MATLAB.

2.3.4   Imaging at 9.4 Tesla

In order to extend the proposed technique to magnetic field strengths increasingly used in molecular imaging studies, especially with small animals, an adiabatic pulse prepared sequence was similarly implemented on an ultra-high magnetic field MRI. All studies were conducted on a 9.4 Tesla Bruker Bio-Spec 94/20 (Bruker BioSpin Corporation, Billerica, MA) using a 3 cm transmit/receive volume coil. The Bruker optimized 10 millisecond hyperbolic secant pulse with a 1760 Hz bandwidth was used, and a 20 ms zero passage pulse was similarly constructed by applying two full passage pulses back-to-back. The adiabaticity and pulse power for the preparation pulse was determined experimentally with a water phantom. Imaging parameters for phantom studies at 9.4 Tesla for included: TE: 10.25 ms, TR: 10 s, matrix: 128x128, acquisition time: 21 min, slice 0.75 mm, FOV: 30x30 mm.

2.4   Results

2.4.1   Monte Carlo Simulation of Adiabatic Contrast

Numerical simulation confirmed that the adiabatic condition fails for spins diffusing near iron oxide nanoparticles. Figure 2.2 shows that for the lowest iron concentration, where the particles are spaced furthest apart, the average M_z magnetization at the conclusion of the preparation pulse is near -1, indicating a complete inversion. As

the iron concentration increases and the particles and their magnetic field gradients move closer together, the average magnetization decreases. In fact, it is exciting to note that the average longitudinal magnetization appears to be linearly correlated with the total iron concentration.
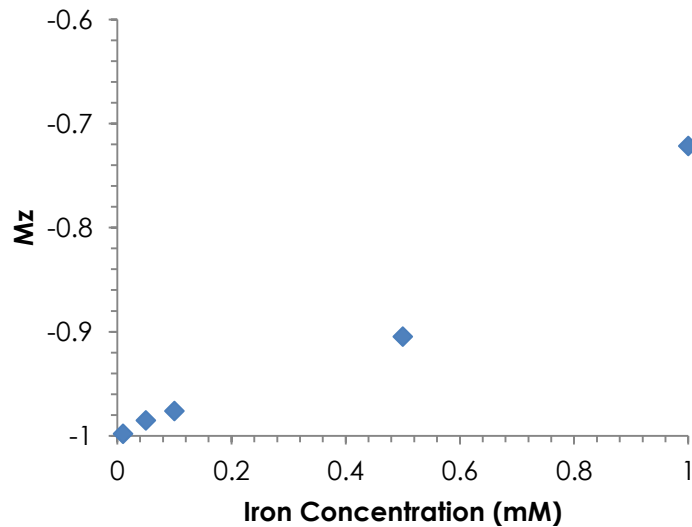
Figure 2.2: Average longitudinal magnetization following AFP

By plotting a histogram of the M_z magnetization at the conclusion of the preparation pulse, the failure of the adiabatic condition for the individual spins is more apparent. In Figure 2.3 at the lowest iron concentration nearly all the spins are inverted as expected, but as the nanoparticle concentration increases the number of spins that are not completely inverted increases as well. When examining higher iron oxide concentrations such as in Fig. 2.5, the expected behavior of the adiabatic full passage is absent. Since the adiabatic condition fails for most of the spins, the majority of the applied RF pulse

behaves as a conventional RF pulse rather than an adiabatic pulse. As the failure of the adiabatic condition is not simultaneous, the final flip angle is random without a predictable relationship between the spin and the RF pulse.
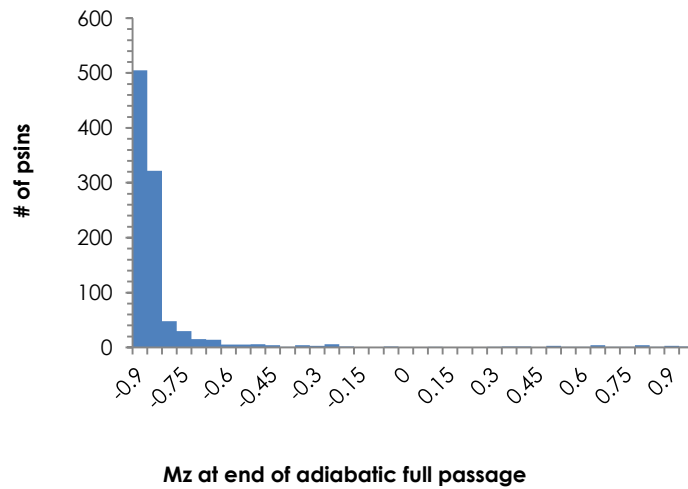
Figure 2.3: M_z of spins with iron concentration 0.01 mM
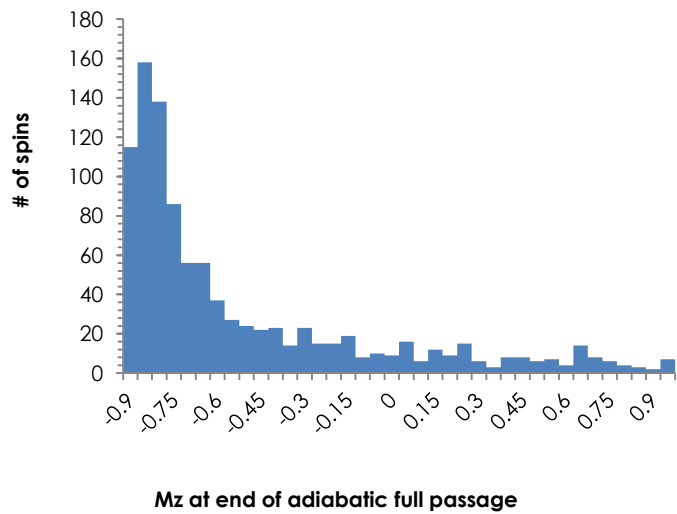
Figure 2.4: M_z of spins with iron concentration 0.05 mM
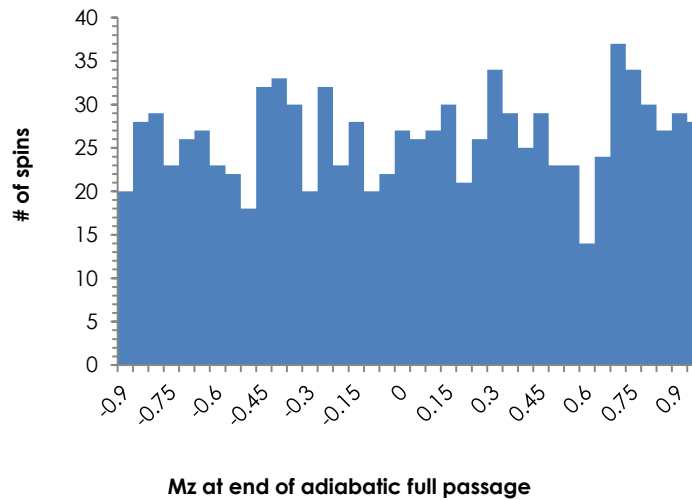
Figure 2.5: M_z of spins with iron concentration 1.0 mM

2.4.2   Visualizing and Quantifying the Adiabatic Full Passage Contrast at 3 Tesla

T2-weighted, spin-echo images showed decreased signal intensity with increasing iron concentration as expected. When the adiabatic full passage preparation pulse was applied there was an even greater decrease in image intensity at higher iron concentrations, but importantly, there was still sufficient signal from the highest iron concentrations to perform contrast quantification. While these images still show a decrease in signal, when the normalized difference between images with and without adiabatic preparation were computed to visualize the failure of the adiabatic condition, there was an increase in signal with increasing iron concentration. Figure 2.4 shows that

the T2-weighted image intensity (center) has an inverse relationship with the adiabatic contrast measurement (right), where the highest iron concentrations produce the brightest signal intensity.
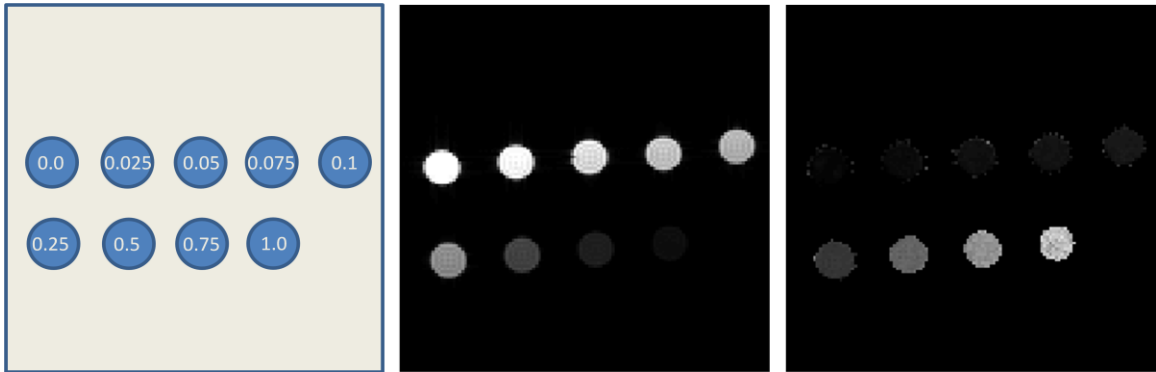
Figure 2.6: Iron-oxide nanoparticles (mM) in solution (left), T2-weighted spin echo (center) and AFP contrast (right) images at 3 Tesla

Quantifying the signal intensity in the adiabatic contrast image showed a highly linear correlation of iron concentration with adiabatic contrast over the range of iron concentrations studied (R^2 = 0.9951). In order to quantify the sensitivity of the method, the minimum detectable concentration, defined as the concentration with five times the contrast to noise ratio, was measured with extremely low nanoparticle concentration phantoms. For the adiabatic full passage experiment, the minimum detectable concentration was determined to be 0.05 mM. For iron concentrations beyond this range, very little signal remains with the sequence parameters used, inhibiting contrast quantification.
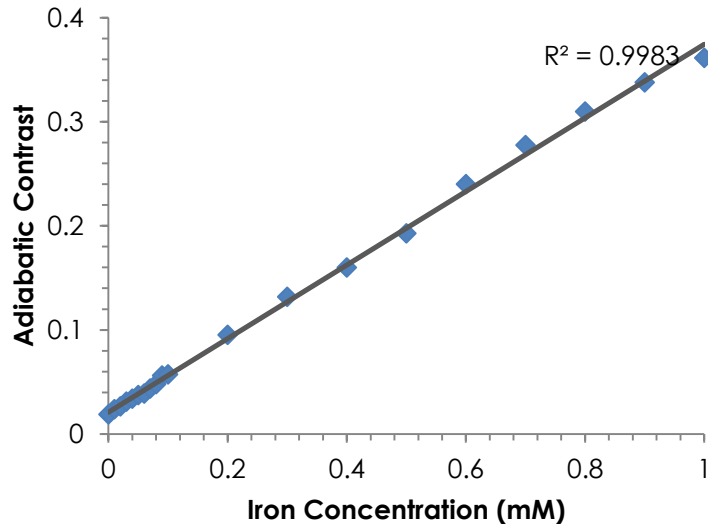
Figure 2.7: Linear contrast correlation with iron concentration in solution at 3 Tesla

2.4.3 Visualizing and Quantifying Adiabatic Full Passage Contrast at 9.4 Tesla

In order to facilitate the application of the proposed method to biological research models, the method was implemented on a 9.4 Tesla small-bore animal scanner. While magnets of this strength are not yet available for regular clinical applications, the increased signal and higher gradient strengths make them desirable for the *in vivo* study of disease processes in the wide variety of established animal models. While magnetic susceptibility becomes an even more significant factor at higher field strengths, this enhancement is not always advantageous when localizing and quantifying groups of iron oxides that may introduce significant inhomogeneities in the magnetic field.

41

Figure 2.8 shows that the adiabatic pulse prepared spin-echo acquisition achieves good image signal quality without geometric distortions, even at high iron concentrations. Similar to the images at 3 Tesla, the ultra-high magnetic field images exhibit the expected inverse relationship between the T2-weighted image intensity and adiabatic contrast with increasing iron concentration.
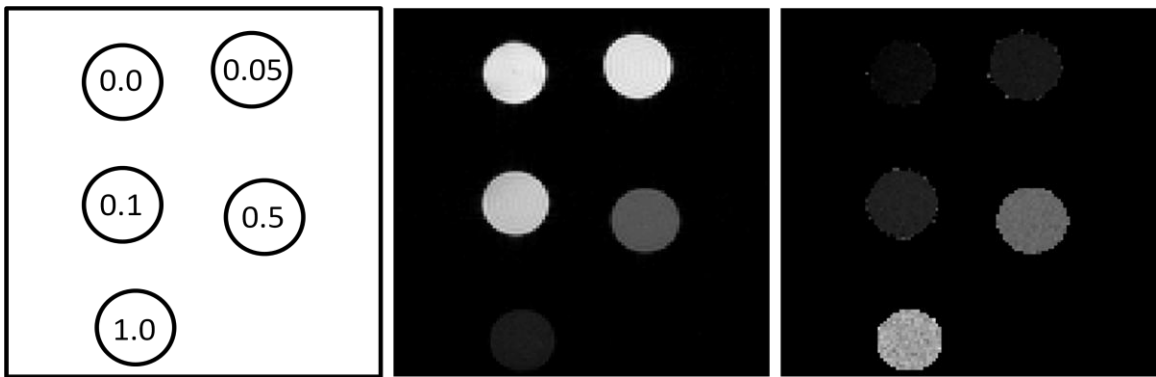
Figure 2.8: Iron-oxide (mM) nanoparticles in solution (left), T2-weighted spin echo (center) and AFP contrast (right) images at 9.4 Tesla

Quantifying the image contrast at 9.4 Tesla shows a similar linear relationship as well. Figure 2.9 shows that the adiabatic contrast is linearly increasing with increasing iron concentration. Similarly in this case, iron oxide nanoparticle concentrations were used up to the point where very little signal could be detected with the minimum echo time for the sequence. Even for these extremes, the contrast remained linearly correlated with the total iron concentration over the range of values studied.
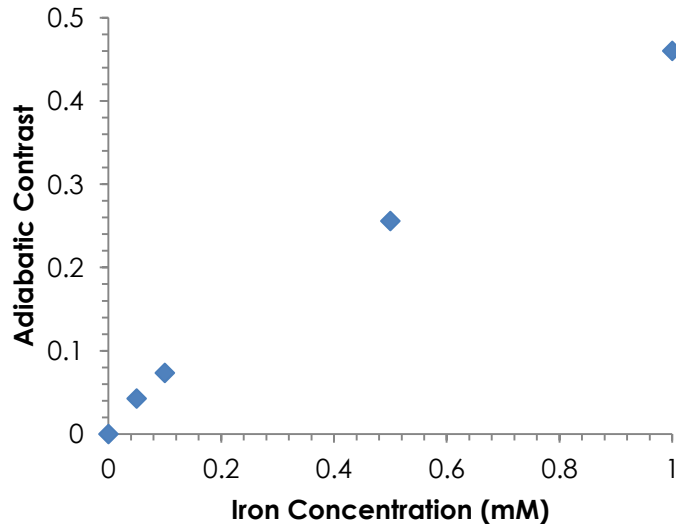
Figure 2.9: Concentration correlation with iron concentration in solution at 9.4 Tesla

2.4.4 Adiabatic Pulse Preparation Using an Adiabatic Zero Passage

A second approach based on the same contrast mechanism is to use an adiabatic zero passage preparation pulse, or two adiabatic full passages applied back-to-back. If the duration of the adiabatic full passage is kept constant, then the maximum B_1 power required to fulfill the adiabatic condition for the zero passage is identical to the full passage. Therefore by applying two passages the magnetization is returned to the original +z orientation, and total diffusion time for the spins is doubled. This doubling should increase the probability of the spins failing the adiabatic condition. This concept will also be used in the following chapter with method to compensate for magnetization transfer. Figure 2.10 shows that while the adiabatic zero passage contrast increases with increasing iron concentration, the correlation of contrast and total iron concentration is not linear

43

over the entire range of iron concentrations, unlike in the adiabatic full passage preparation studies.
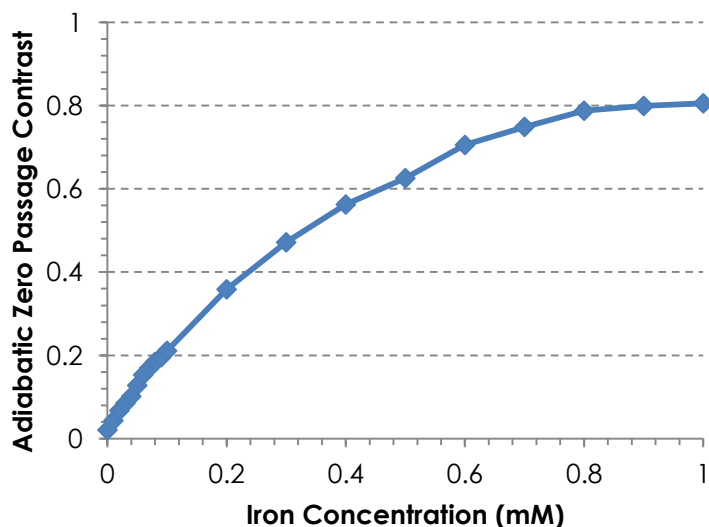
Figure 2.10: Contrast correlation with adiabatic zero passage in solution at 3 Tesla

However, the adiabatic zero passage contrast does appear to be linearly correlated with iron concentration at the lowest nanoparticle concentrations. Figure 2.11 shows that within the iron concentration range from 0.0 to 0.1 mM the contrast is highly linear ($R^2 =$ 0.9915). Using the previously defined sensitivity measure, the minimum detectable concentration was found to be decreased to 0.02 mM. While high sensitivity and linearity over the entire range of iron concentration would be ideal, quantification over a very broad range of nanoparticle concentrations may be less likely. In fact with the technique using a normalized difference image for contrast measurement, an asymptote will be reached at some point. While this appears to be the case above 0.5 mM for the 20 msec

zero passage preparation at 3 Tesla, this is a function of the pulse parameters and can be optimized for a specific application.
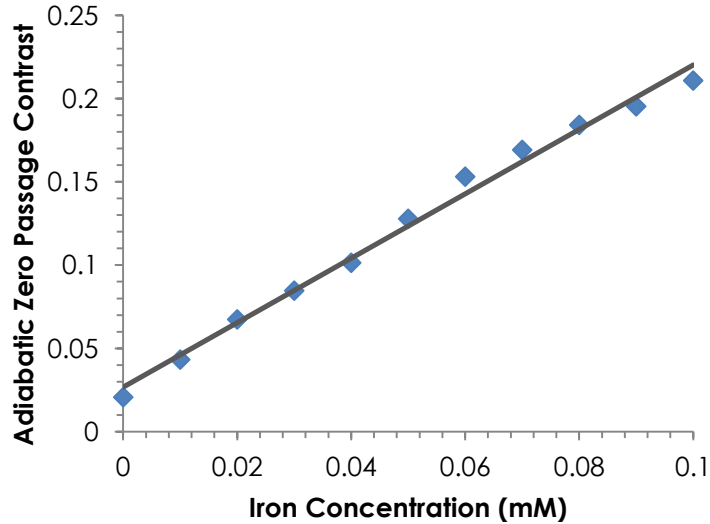
Figure 2.11: Adiabatic zero passage contrast at low iron concentration at 3Tesla

Plotting these data together illustrates their complementary potential. While the adiabatic full passage contrast remains linear for the entire range of iron concentrations studied, the adiabatic zero passage contrast is linearly correlated for very low concentrations of nanoparticles and is more sensitive than the full passage contrast. Since the expected iron concentration may be estimated in many applications, the two preparation techniques offer different approaches, based on the same underlying physics, to increase the sensitivity for detecting extremely low nanoparticle concentrations, or to increase the linear dynamic range of the contrast for quantifying total iron concentration. However, these are not the only ways in which the preparation pulse can be modified to

affect the contrast. It will also be shown that pulse parameters for either method, such as the pulse duration, can be tuned to specific contrast ranges.
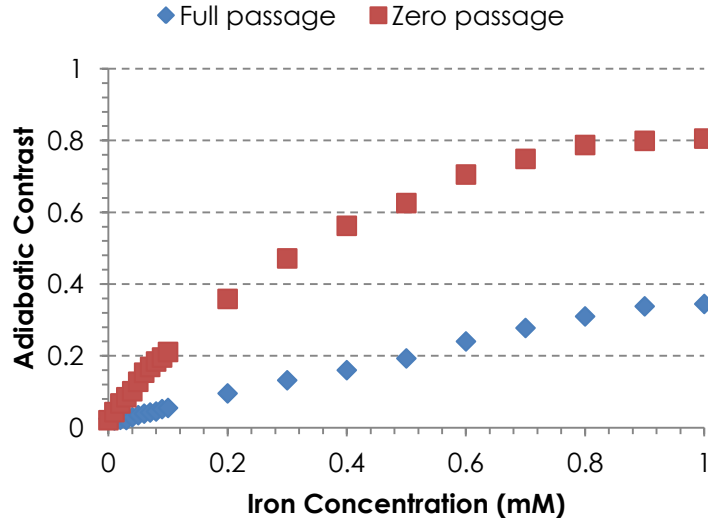
Figure 2.12: Adiabatic full and zero passage contrast in solution at 3 Tesla

2.4.5 Characterizing Adiabatic Contrast with Different Iron Oxide Core Sizes

Since the contrast is theoretically a function of both the pulse and nanoparticle parameters, different sized iron oxide cores were used to characterize the dependence of the contrast on iron oxide core size. Since the magnetic field gradients surrounding the particle are dependent on both the size of the particle and the magnetic susceptibility (59), the relationship between the contrast and total iron concentration is not straight forward. For a single total iron concentration, different sized nanoparticles produce different inter-particle spacing, which means that the probability of a spin encountering a

46

nanoparticle during its diffusion also changes. Additionally, increased susceptibility effects increase the volume of the strong magnetic field gradients surrounding the particle, which also change the probability of a spin diffusing through a sufficient magnetic field gradient.
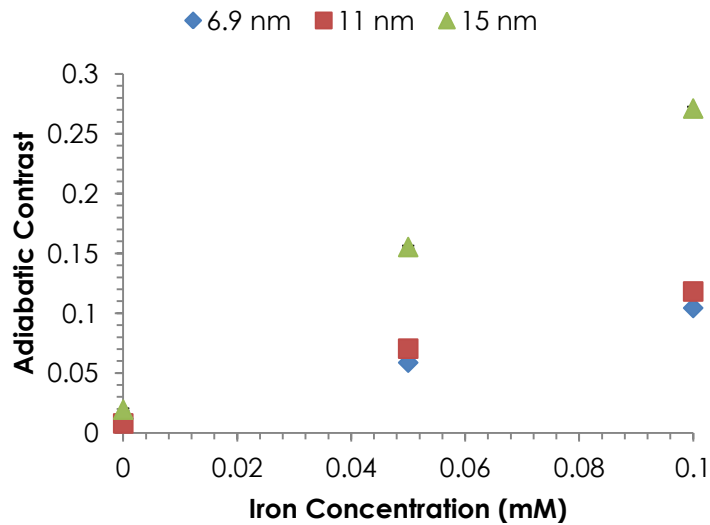
Figure 2.13: Full passage contrast with different iron oxide core sizes in solution at 3 Tesla

Overall, the adiabatic full passage contrast was linearly correlated with the total iron concentration for each iron oxide core size at 3 Tesla. Since the relaxivities of the new particles were much greater than the Feridex nanoparticles used in the previous experiments, insufficient signal was obtained from the spin-echo images of the higher iron concentrations. However, the there was a very high level of linear correlation below 0.1 mM for each iron oxide core diameter: 15 nm $R^2 = 0.9979$, 11 nm $R^2 = 0.9941$, 6.9 nm $R^2 = 0.9999$. The larger effects on the local magnetic field produced by the larger iron

oxide cores yielded greater changes in adiabatic full passage constant per iron concentration. This increase in sensitivity for larger particles did not affect the linear correlation of the contrast over the range of iron concentrations up to the point where the signal was lost in the spin-echo image.
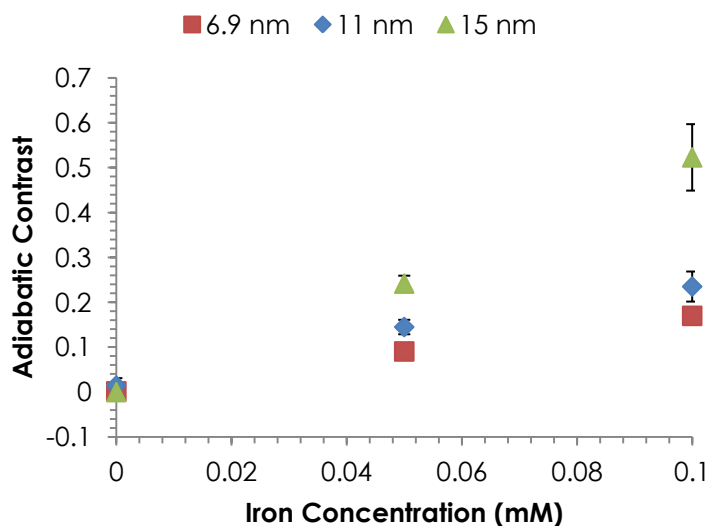
Figure 2.14: Full passage contrast with varying iron oxide core sizes in solution at 9.4 Tesla

These experiments were reproduced at 9.4 Tesla, and there was a similar loss of signal at high iron concentrations due to high relaxivity. However, the linear correlation of the adiabatic contrast with total iron concentration was preserved. The correlation coefficients for the linear fit of contrast and iron concentration for the different core sizes were 15 nm $R^2 = 0.9981$, 11 nm $R^2 = 0.9889$, 6.9 nm $R^2 = 0.9989$. It is notable that the standard deviations of the measurements were greater at 9.4 Tesla than at 3 Tesla; however, on average the contrast remained highly linear with the contrast at the zero iron

concentration statistically indistinguishable from zero. Otherwise, the relationship between the iron oxide core size and the adiabatic contrast was consistent between the experiments performed at 3 and 9.4 Tesla.

2.4.6 Characterizing the Effect of Varying Adiabatic Pulse Duration and Frequency Sweep on Adiabatic Contrast

As the results from the full and zero passage experiments demonstrated, the adiabatic contrast can be modulated by modifying the preparation pulse parameters, while the same mechanism is exploited. While the preceding data used a 10 msec preparation pulse because it provided sufficient diffusion distance relative to the nanoparticle spacing and was compatible with the total power applied to the sample, the same theory applies to pulses of different durations. However, the contrast produced is not expected to be identical for different preparation pulse durations. Figure 2.15 shows that different preparation pulse durations yield different linear concentration curves, especially for higher iron concentrations. The shortest pulse duration is the least sensitive, followed by the intermediate length, and the longest pulse duration is the most sensitive to the total iron concentration. This relationship is expected from theory, since the increased preparation pulse duration is directly related to the increased average diffusion distance of the spins. As the average diffusion distance of a spin increases, the probability of the spin diffusing though the strong magnetic field gradients surrounding the nanoparticles also increases.
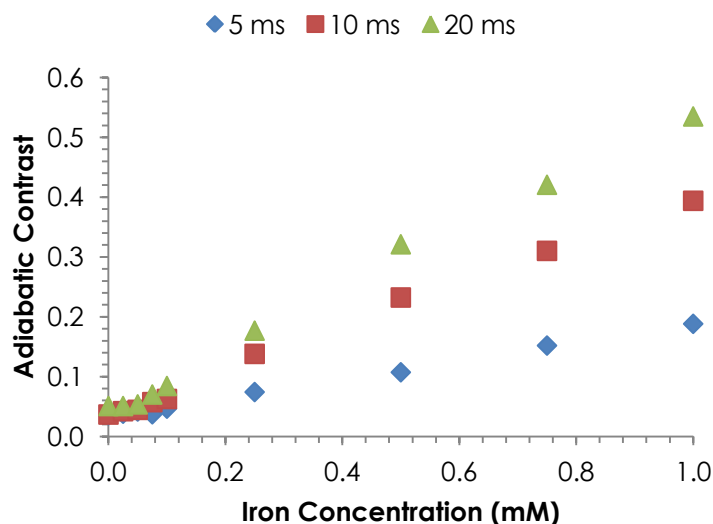
Figure 2.15: Adiabatic contrast with different hyperbolic secant pulse durations at 3 Tesla

A second pulse parameter that can be modulated is the frequency sweep covered by the adiabatic pulse. As was previously shown, this frequency sweep is related to the acceleration of the effective field during the preparation pulse and the fulfillment of the adiabatic condition. If we use a very high B_1 power (approximately 15 dB greater than the minimum power necessary to accomplish the adiabatic passage) to ensure that the adiabatic condition is fulfilled for all sample preparations, we see that a wider frequency sweep is able to successfully invert a greater proportion of the spins (Figure 2.16). As the frequency sweep narrows, the adiabatic contrast sensitivity increases. Here, more spins fail the adiabatic condition as they diffuse through the magnetic field gradients during the narrower bandwidth preparation pulse. The narrow frequency sweep is unable to invert these spins, and the net effect is that the preparation is more sensitive to the iron oxide

nanoparticles. Optimization using these frequency parameters may be especially important for applications where non-nanoparticle sources of off-resonance may be avoided with the adiabatic technique that would confound other methods of off-resonance measurement.
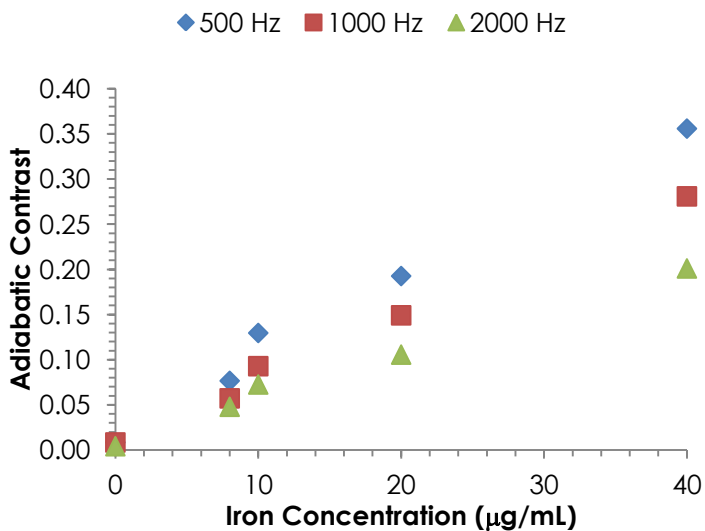
Figure 2.16: Adiabatic full passage contrast with different frequency sweep bandwidths

2.5 Discussion and Conclusion

This chapter introduced a method for detecting and quantifying iron oxide nanoparticles based on a new contrast mechanism. Monte Carlo simulation and experimental results support the proposed contrast mechanism described by the failure of

the adiabatic condition in the regions surrounding the nanoparticles. This approach produces a contrast that can be visualized as an adiabatic contrast image, and nanoparticles in concentration ranges appropriate for molecular imaging show a highly linear correlation of adiabatic full passage pulse prepared contrast with total iron concentration.

In addition to using an adiabatic full passage preparation pulse, several approaches were developed to modulate the contrast based on the sequence parameters. The adiabatic zero passage contrast may be especially useful, since doubling the diffusion time increases the probability of a spin encountering a nanoparticle. Also, the full rotation of the zero passage preparation returns the magnetization to its original orientation. The advantage of this property is highlighted by the nanoparticle quantification at 3 Tesla, where T_1 relaxation after the application of the full passage pulse may result in a measured contrast for pure water different from the expected zero measurement. In this case, quantification of pure water with the zero passage produces a near zero contrast. This is similar to the result for the full passage at 9.4 Tesla, where the T_1 relaxation rate of pure water is much longer, and thus there is very little relaxation in pure water for both the full and zero passage preparations. It will also be shown in the following chapter that the duration and power of the zero passage preparation pulse can be used in a technique to compensate for magnetization transfer effects.

Controlling the size of the iron oxide core presents an opportunity to change the size and strength of the magnetic field gradients surrounding the nanoparticles. By

comparing different core sizes with the same total iron concentration in the sample, both the size of the gradients and the average distance between the particles are affected. This is important because for molecular imaging applications there may be very low concentrations of contrast agents, and it is ideal to maintain contrast quantification as the susceptibility and size of the agents are increased. The results presented show that it is not until the signal detection limit of the image acquisition is reached that the quantification is compromised. As the contrast is more sensitive to the larger particles at a given total iron concentration, this may be an important parameter in choosing an agent for an experiment. However, the core size dependence of the contrast quantification means that the core size of the particles must be known to interpret the contrast measurement. This would not be a concern if a single core size is used, or if a range of well distributed sizes can be averaged on a voxel level, but if a range of sizes is administered with a narrow size band of particles preferentially accumulating in a tissue, the quantification could be compromised. The simplest solution would be to use particles of uniform size, though further studies are required to fully to characterize the core size dependence.

In the future, it would also be interesting to investigate the effect of the particle coating on the adiabatic contrast. This effect may be as significant as the iron oxide core size, since restricting spin diffusion near the particle could have the effects of both limiting spin access to the strong gradients surrounding the particles as well as slowing spins within these gradients. These effects may either restrict or enhance access to the strong magnetic field gradients that cause the adiabatic condition to fail, since the net

effect is determined by the physical interaction of the iron oxide core coating with the diffusing spins.

Perhaps of greater utility for an image contrast mechanism is the ability to tune the contrast sensitivity based on the prescribed sequence parameters. While many applications will be limited by the iron oxide nanoparticles available to the researchers, pulse and sequence parameters that can be modified during image acquisition present an opportunity to optimize contrast detection and quantification. In this chapter, both the duration and frequency sweep of the preparation pulse are shown to modulate the quantitative adiabatic contrast in agreement with the proposed theoretical mechanism. This is useful as the optimal pulse duration will be specific to the application and the contrast agent used. For quantification, staying within the linear range may be of primary importance, but as it has been shown, this range depends on the specific properties of the particles. On the other hand, the modulation of the frequency sweep may be especially important when other off-resonance effects are present. By defining the frequency sweep to be sensitive to the nanoparticles while avoiding these other components, optimal quantification can be achieved.

Overall, the adiabatic pulse prepared technique yields a contrast that is linearly correlated with iron concentration. By modifying both the nanoparticles and the pulse sequence, the sensitivity of the contrast can be optimized while maintaining the desired linear correlation of the nanoparticles with the contrast. The utility of this approach is also greatly aided by the fact that the contrast is achieved during the short duration of the

preparation pulse. As will be shown in the following chapters, this allows for a number of

accelerated imaging techniques to be implemented that generate a reproducible contrast

that is also generally applicable to *in vivo* studies.

CHAPTER 3

CHARACTERIZING ADIABATIC PULSE PREPARED CONTRAST

IN PHANTOMS AND IN VITRO

In the previous chapter, a mechanism for producing MR contrast from iron oxide nanoparticles that is linearly correlated with iron concentration was described. While the results using nanoparticles in solution are very encouraging, translating this work to *in vitro* and *in vivo* applications requires more realistic phantoms that reflect the challenges inherent in quantifying iron concentrations in varied molecular environments. The first part of this chapter describes using nanoparticles embedded in agarose phantoms to incorporate magnetization transfer and diffusion affects similar to the cellular environment. Here, the effect on the contrast is not only characterized, but a method for compensating for this effect is proposed and validated based on the molecular mechanism of the contrast. Second, the contrast quantification is further characterized by varying sequence and environmental parameters, and the approach is compared to other MR methods for imaging iron oxide nanoparticles. Finally, the method is applied to two complementary models of *in vitro* molecular imaging. The results show that the adiabatic pulse prepared method is not very sensitive to inhomogeneities in the magnetic fields or changes in the molecular environment that are not associated with the nanoparticles. While the nanoparticles in the cellular imaging studies are no longer uniformly distributed as they were in the solution phantoms, the *in vitro* results are also promising,

since the identification and quantification of the nanoparticles remains successful as confirmed with molecular iron quantification. Overall, with the development of the magnetization transfer compensated approach, a method that is already less sensitive to non-nanoparticle effects is able to quantify intracellular nanoparticle concentration in multiple cellular imaging applications.

3.1 Introduction

While quantifying iron oxide nanoparticles in solution with MR may be of limited utility, there is an ever expanding list of applications of nanoparticles for molecular and cellular imaging. Here, the inherent advantages of MRI as a clinically applied, non-invasive method for imaging with relatively high spatial and temporal resolution make it a natural fit for translational studies. However, as has been described, the sensitivity of MR is much lower compared to PET (97), even though the simultaneous acquisition of high resolution anatomical images with MRI provides complementary information and many diagnostic advantages. Applications including tracking SPIO labeled neural cells for the treatment of stroke (98) and cardiac stem cells for the treatment of myocardial infarction (99) combine the anatomical and functional information provided by traditional MR imaging with the ability to use cellular imaging to localize the therapeutic cells and evaluate treatment outcomes. With these exciting applications in mind, we aimed to

57

translate the adiabatic pulse prepared mechanism into cellular imaging applications with the goal of maintaining a quantitative molecular imaging method.

Cellular MR imaging encompasses a variety of methods from tracking SPIO labeled cells (100), to quantifying an increase in the expression of a cell surface receptor (101), and to detecting the upregulation of a gene (17). Additionally, nanoparticles can provide important information about the structure and function of tissues by passively accumulating in regions where there is a breakdown in vessel permeability (102). Perhaps the most straightforward cellular MR imaging application is to label cells with SPIO *ex vivo* and then either implant the cells near the therapeutic target, or administer them intravenously and allow them to circulate and passively or actively accumulate in the tissue of interest. While cells such as macrophages efficiently take-up the iron oxide nanoparticles when incubated with them (103), for many cell types of pathological interests such as cancer and stem cells more advanced techniques such as antibody conjugation (104) or cell membrane disruption (105, 106) may be required for sufficient cellular labeling.

Since the effect of the nanoparticle on the MR signal is a function of factors including the size, composition and coating of the particle, there are many parameters that can be modified within a cellular imaging application. In fact, much recent research has focused on developing paramagnetic and superparamagnetic nanoparticles that have an even greater effect on relaxivity, are more biocompatible, and can be more easily modified by surface chemistry for molecular imaging (107). However as these

modifications are made to increase the imaging effects, the contrast agent must maintain a minimal effect the normal molecular processes and differentiation of the cell. While most molecular imaging studies have shown minimal cytotoxicity (108), alterations to gene expression remain a significant concern, especially in stem cell studies and at higher iron concentrations (109). Some studies have shown changes in cellular differentiation (110) and function (111) attributed the interaction of the iron oxide nanoparticles and the transfection agents with the normal cellular processes. An additional challenge that is an active area of research is the correlation of cell fate with the fate of the image contrast (112). While these remain important issues for the development of molecular MR imaging, exciting applications have already been developed allowing SPIO labeled cells to ask and answer new questions regarding normal physiological development, pathological growth and treatment response.

While these *in vitro* techniques can efficiently label many cell types, the end use of these cells will be within a diverse molecular environment with many physiological and magnetic properties. One concern is that the adiabatic preparation pulse may saturate off resonance spins that are not associated with the nanoparticles and confound nanoparticle quantification through magnetization transfer effects (113). Other areas of interest include the sensitivity of the technique to changes in the static and applied magnetic fields, as well as the magnetic parameters of the tissue. Since the B_0 and B_1 magnetic fields are not exactly uniform, a quantification that is spatially dependent with the spatially varying magnetic fields is not ideal.

In this chapter the adiabatic pulse prepared technique is characterized in more realistic phantoms and cellular imaging models. Also, a method of compensating for the small magnetization transfer effects associated with the preparation pulse is developed based on the contrast mechanism. Next, the proposed technique is compared to previously proposed methods of iron oxide imaging both for their ability to quantify the nanoparticles as well as their sensitivity to environmental parameters. Finally, the *in vitro* cellular imaging potential of the technique is evaluated using two models: first by directly labeling cancer cells with SPIO nanoparticles and correlating the image contrast with the iron concentration as determined by *ex vivo* molecular measurement, and second by distinguishing cells cultured with iron with and without a reporter gene that promotes intracellular iron oxide nanoparticle formation.

3.2 Methods

The main objectives of this chapter are to *(a)* quantify magnetization transfer effects and develop a method to compensate for them, *(b)* characterize the dependence of the adiabatic contrast on parameters of the imaging system and the molecular environment, *(c)* compare the proposed technique to other methods of quantifying iron oxide nanoparticles, and *(d)* correlate the adiabatic contrast with the measured iron concentration in cellular imaging applications.

3.2.1 Iron Oxide Nanoparticle Phantoms

Dilutions of iron oxide nanoparticles in solution were prepared as in the previous chapter. For phantoms in agarose gel, dilutions of Feridex (Advanced Magnetic, Inc., Cambridge, MA) were prepared in water with 2% agarose (Sigma-Aldrich, St. Louis, MO) by weight. Nanoparticles were added to the hot agarose solution when it was in its liquid state and vortexed to combine. The well mixed samples were then allowed to set at room temperature. By visual inspection, the particles appeared well distributed, and the agarose was uniform after the phantoms solidified.

The diffusion dependence of the contrast was investigated by doping the phantoms with polyetheleglycol to reduce the diffusion rate. Polyethyleneglycol-400 (Sigma-Aldrich, St. Louis, MO) was added in specific ratios by weight as previously reported (114) to change the diffusion rate of the phantom. Five iron concentrations (0.0, 0.067, 0.133, 0.5, 1.0 mM) were prepared with five different diffusion rates (2.50e-09, 4.440e-10, 3.70e-10, 2.90e-10 m^2/sec).

3.2.2 Imaging at 3 Tesla

Adiabatic pulse prepared imaging was performed at 3 Tesla on a Siemens Magnetom Trio (Siemens Medical Solutions, Malvern, PA, USA) with a spin-echo sequence modified to include either a full or zero passage preparation pulse. A 10

millisecond hyperbolic secant pulse with a frequency sweep of -/+ 1000 Hz was used for adiabatic full passage, and a zero passage pulse was formed by combining two adiabatic full passage pulses back-to-back. Sequence parameters for the cell imaging experiments at 3 Tesla included: TE: 15 ms, TR: 10 sec, matrix: 128 x 128, slice: 2 mm, FOV: 100 x 100 mm.

For the off resonance saturation (ORS) technique, a Fast Low Angle Shot (FLASH) sequence was prepared with a 6 millisecond Gaussian saturation pulse. A frequency offset of 1000 Hz was found to provide good quantification for the particles used (91), and the power of the saturation pulse was determined experimentally. For the frequency selective inversion pulse, a 2 millisecond sinc pulse with a 180 degree flip angle was applied as a preparation pulse. Contrast calculation was performed in MATLAB using a same normalized difference method applied to the adiabatic contrast measurement.

3.2.3   Imaging at 9.4 Tesla

An adiabatic pulse prepared sequence was also implemented on a 9.4 Tesla Bruker BioSpec 94/20 (Bruker BioSpin Corporation, Billerica, MA). The vendor-provided, optimized hyperbolic secant pulse with frequency sweep -/+ 1760 Hz was used for full passage, and back-to-back full passage pulses were used to achieve a zero passage

preparation. Other sequence parameters for ultra-high field imaging at 9.4 Tesla were TE: 10.205 msec, TR: 10 sec, matrix: 128 x 128, slice: 1.00 mm, FOV: 30 x 30 mm.

The performance of the adiabatic full passage pulse was evaluated by applying a single pulse and acquiring the free induction decay (FID). The power of the preparation pulse was increased until a full inversion was achieved, and as the power was increased past this point there was no change in the signal. This experiment confirmed the adiabaticity of the pulse, as well as providing the range of B_1 power sufficient for adiabatic passage used in the following experiments. To characterize the effects of offsetting the pulse frequency from resonance, an irradiation offset was applied to shift the frequency of the applied pulse from on-resonance. A range of frequency offsets were selected within the frequency sweep, near the bandwidth limit, and beyond the frequency sweep to characterize the effect of frequency offset on contrast quantification.

3.2.4   Cell Sample Preparation

Human glioma U87 cells overexpressing the $\alpha_v\beta_3$ integrin were cultured in serum-free RPMI media, and SPIO nanoparticles with a core diameter of 10 nm that were conjugated to a small peptide RGD were prepared by Dr. Hui Mao's laboratory. The cells were then incubated with a 0.1 mM concentration of the iron oxide particles for two hours at room temperature. Next, the cells were washed with PBS, collected, and re-suspended in 1 mL of 2% agarose gel. To achieve different nanoparticle concentrations in

different samples, different numbers of cells were embedded in the same volume to establish a range of total iron concentrations.

For the endogenous contrast model, a gene with a suspected role in the crystallization of iron by magnetotactic bacteria was transfected into a mammalian cell line. The AMB-1 *mms6* gene was cloned into the pBudCE4.1 vector (Invitrogen, Inc, Carlsbad, CA) and transfected into 293T cells. Reporter protein expression, increased iron accumulation and increased transverse relaxivity were confirmed in other work. Control 293T cells and 293T cells transfected with the reporter gene were incubated with 200 μM ferric citrate for three days. The cells were then washed and re-suspended in 1 mL PBS. Cells were allowed to settle by gravity for 2 hours at 5 degrees Celsius. Imaging was then preformed at 9.4 Tesla as described for the phantom studies.

3.3 Results

3.3.1   Characterizing the Effect of Magnetization Transfer on Contrast

One challenge that is especially noteworthy for imaging techniques that detect off resonance components by saturation is that magnetization transfer (MT) effects that are not a function of the nanoparticles can obscure the desired contrast (115). Magnetization transfer describes the transfer of magnetization from of spins in a restricted state, often associated with macromolecules *in vivo*, to the mobile pools of spins that are imaged, and

the MT effects are detected indirectly (113). While these effects can produce a desirable contrast, when this transfer of magnetization is unintended it can confound the contrast interpretation. Therefore it is essential to quantify any MT effects that do not originate from the nanoparticle dependent mechanism and develop methods for compensating for the contrast to increase the accuracy and specificity for the iron oxide nanoparticle quantification.

To test the sensitivity of the adiabatic pulse prepared method to MT effects, nanoparticle concentrations identical to the previously described solution phantoms were embedded in 2% agarose gel. Replicating the sequence parameters and maximum B_1 power, Figure 3.1 shows that the spin-echo and adiabatic contrast images for the agarose phantoms appear similar to previously presented solution phantoms. In both, there is a decrease in T2-weighted image intensity with increasing nanoparticle concentration and an increase in adiabatic contrast with increasing particle concentration. Importantly, any affects introduced by the agarose gel are not significant enough to impede contrast visualization.
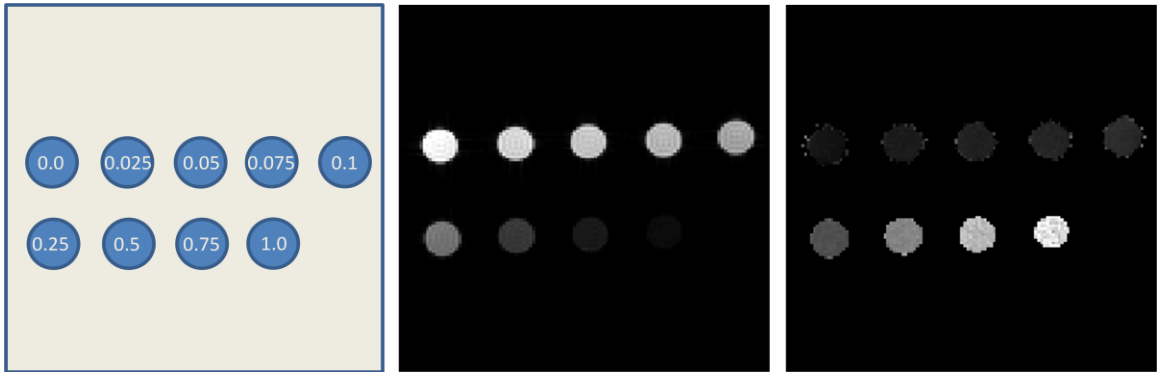
Figure 3.1: Iron-oxide in 2% agarose gel (left) with T2-weighted spin-echo (center) and adiabatic contrast (right) images at 3 Tesla

However, after quantifying the contrast, a contrast component appears in the agarose gel phantoms that is not present in solution data. Figure 3.2 shows that the contrast curve for the agarose appears vertically shifted compared to the contrast relationship in solution. However, when only considering the nanoparticles embedded in agarose, the adiabatic full passage contrast remains highly linearly correlated with iron concentration ($R^2 = 0.9979$). In this case, an absolute zero crossing for the contrast at a zero iron concentration is not only optimal for iron quantification, but it is necessary to develop a contrast mechanism that is specific to the iron content. While relative iron quantification within a homogeneous molecular environment may be compatible with the shifted contrast versus concentration relationship, a uniform MT effect cannot be assumed within an inhomogeneous sample. Since varied molecular environments produce spatially dependent MT effects throughout the sample, it is likely not possible to characterize these multiple curves.
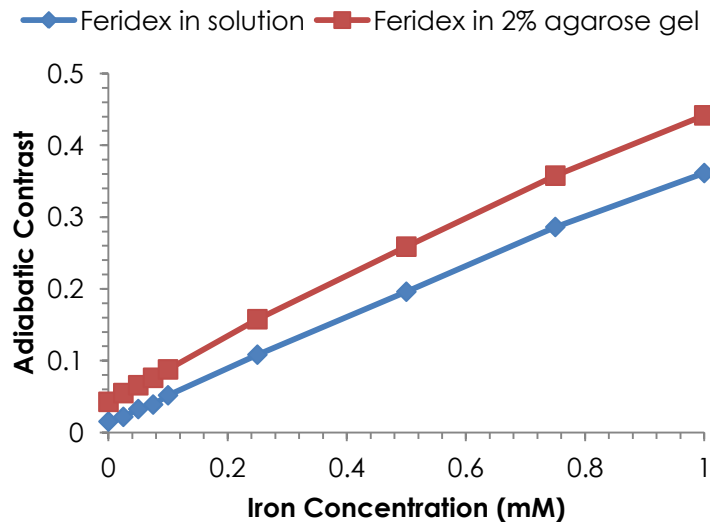
Figure 3.2: Adiabatic contrast in solution and 2% agarose gel at 3 Tesla

These phantoms where then imaged at 9.4 Tesla to investigate if the same effects would be present. Figure 3.3 shows similar results to those described at 3 Tesla, with the increase in adiabatic contrast visually apparent in the agarose phantoms. Additionally, the contrast appears quite homogeneous within the samples.
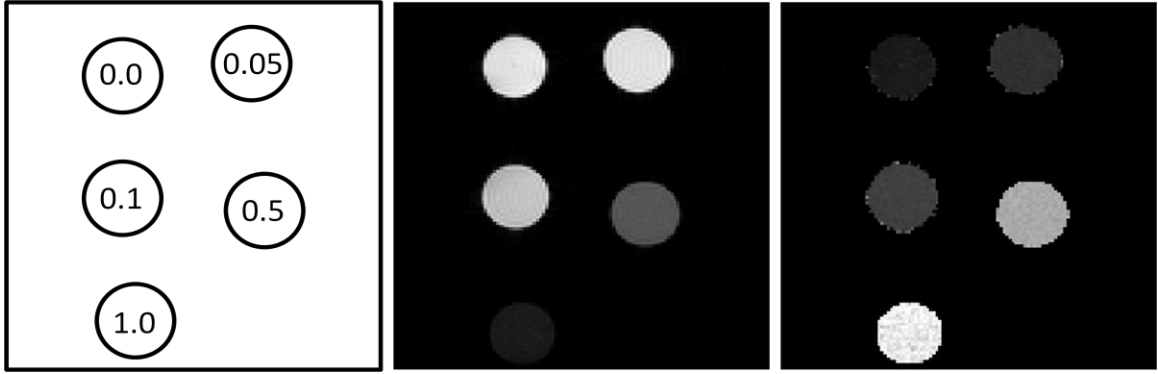
Figure 3.3: Different iron-oxide concentrations (mM) in 2% agarose gel (left) with corresponding T2-weighted spin-echo (center) and adiabatic contrast (right) images at 9.4 Tesla

In fact, quantifying the adiabatic full passage contrast and comparing the results to those from the nanoparticle solution phantoms also gives similar results to the experiments at 3 Tesla. Figure 3.4 shows the while the adiabatic contrast remains linearly correlated with iron concentration, there is an additional contrast component that adds a uniform level of contrast to each iron concentration. At 9.4 Tesla, the high degree of linear correlation (Feridex in water $R^2 = 0.9955$ and Feridex in 2% agarose gel = $R^2 = 0.9961$) and uniform concentration curve shifting is especially notable, since the zero iron concentration condition produces virtually zero contrast. The fact that the additional concentration components appear so uniform at both field strengths suggests that there may be a way to remove this effect.
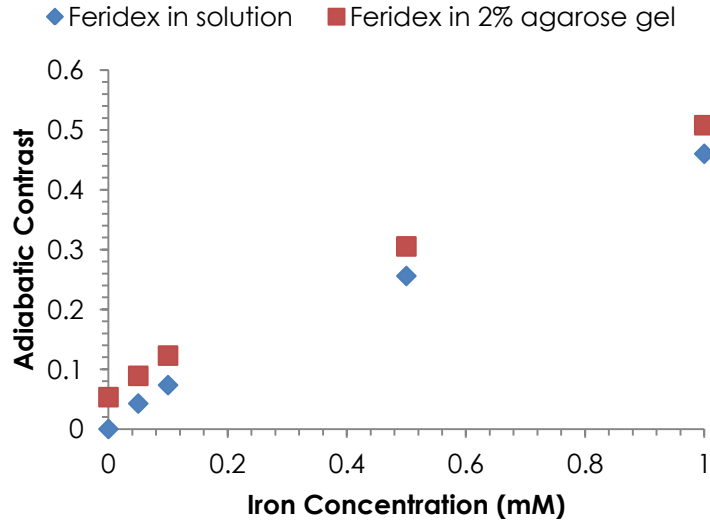
Figure 3.4:Adiabatic contrast in solution and 2% agarose gel at 9.4 Tesla

3.3.2 Compensating for Magnetization Transfer Effects with a Zero Passage Adiabatic Pulse

While the additional contrast component present for the iron oxide nanoparticles embedded in 2% agarose gel does not destroy the contrast, it does affect the specificity of the contrast and the quantification of the nanoparticles. Developing an iron oxide specific measurement method is especially important for *in vivo* applications, where inhomogeneous molecular environments will not provide uniform contrast components similar to the phantom experiments. In these cases, the measurements will be confounded by the interaction of the inhomogeneous spatial distributions of the MT effects combined with the effects of the nanoparticles themselves. With these challenges to quantification

69

in mind, the objective of this work was to develop a method to compensate for the magnetization transfer effects on the adiabatic contrast.

A first idea was to decrease the delivered off resonance RF power by simply decreasing the maximum power of the adiabatic pulse. While a pulse with greater power than minimally necessary to satisfy the adiabatic condition was used to ensure that the adiabatic condition was met for the entire imaging region, this peak power can be decreased to characterize the effect of RF power on the adiabatic contrast. It was not expected that this method would eliminate the additional contrast component, but given our hypothesis regarding the origin of the additional contrast component, the decreased peak RF pulse power should decrease the undesired contrast.
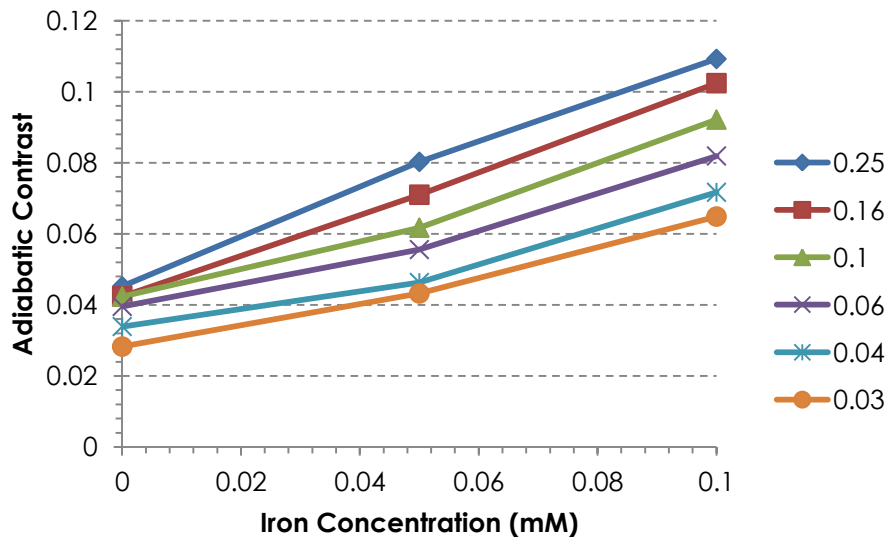
Figure 3.5: Contrast with decreasing fraction of full B$_1$ power in 2% agarose gel at 9.4 Tesla

Figure 3.5 shows that as the power decreases the contrast at the lowest iron concentration decreases monotonically as a function of peak RF power. This method is able to reduce the additional contrast component by nearly half. However, this approach has practical drawbacks that make it not ideal for normal experimental conditions. If the peak power is reduced to a point where the failure of the adiabatic condition is no longer solely a function of the iron concentration but is also dependent on the spatial distribution of the applied B_1 field, then any temporary gain in the specificity of the contrast for the nanoparticles due to decreasing the RF power and reducing the MT effects would be quickly lost if there was insufficient power for adiabatic passage over the entire region of interest. Again, while it was not expected that this approach would completely account for the MT effects, the characterization of this mechanism led us to develop the following more complete approach.

The objective in developing an MT compensated imaging approach was to decouple the desirable diffusion effects that produce the adiabatic contrast from the undesirable effects of off resonance power deposited in the sample. Here, the adiabatic zero passage introduced in the previous chapter was used, as it doubles the power with back-to-back adiabatic full passage pulses without doubling the average spin diffusion distance. Since the average diffusion distance increases by the square root of time, doubling the duration of the pulse does not lead to a doubling of the average diffusion distance. Figure 3.6 shows a schematic of the proposed method in which both adiabatic full and zero passage pulse prepared imaging sequences are applied. The full passage contrast is then doubled to equalize the power effects on the contrast to the zero passage

71

case; however, this doubling also doubles the diffusion effects. Since the diffusion effects of the zero passage adiabatic pulse are less than the doubling of the full passage, subtracting double the full passage from the zero passage should yield a contrast that is sensitive only to the diffusion effects. By keeping the duration and peak power of the two approaches consistent, the results are comparable between the two sequences.
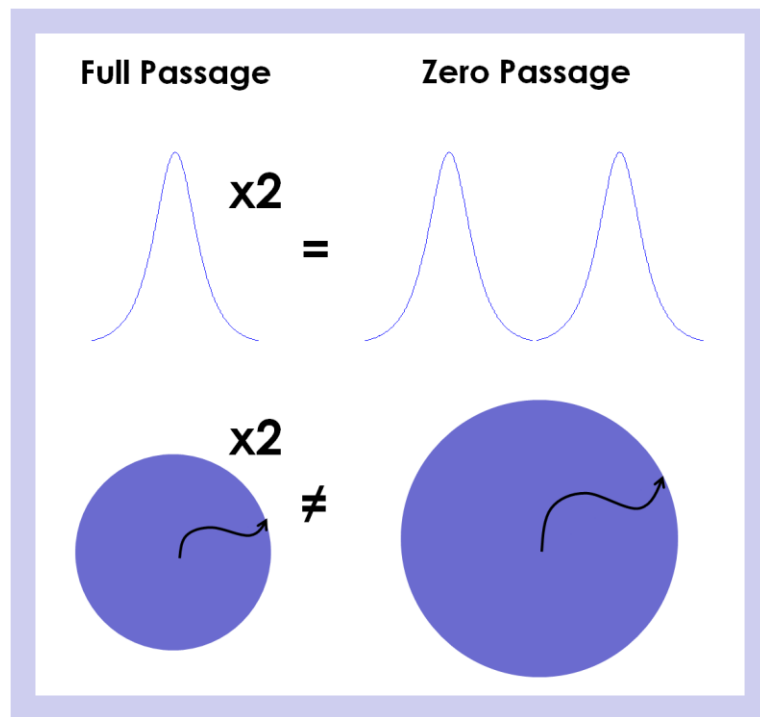
Figure 3.6: Schematic of magnetization transfer compensated adiabatic contrast

First, the full and zero passage pulse prepared adiabatic contrasts were quantified for iron oxide nanoparticles in 2% agarose gel. Figure 3.7 highlights two important findings. First, at the zero iron concentration the zero passage contrast is approximately double the full passage contrast, and second, especially for the highest concentration of

nanoparticles, the zero passage prepared contrast reaches an asymptote as previous described. The doubling of the zero passage iron contrast is especially encouraging, as this is what is predicted by theory. The linearity is also interesting as it may be a result of either the saturation of the contrast, or it is possible that the magnetization transfer effects between the samples are not uniform. In fact, subtle differences in agarose cooling can lead to local changes in the agarose composition and deviation from the assumed uniformity. By simply shifting the curve to a zero intercept and reducing the contrast by a relative amount, the zero passage contrast dependence is artificially modified; however, even this method does not address the linearity of the contrast dependence since it does not account for the individual variability of the samples. By developing a technique that compensates for the MT effects by being both sensitive to the nanoparticles and the inherent MT of the sample, a method can be developed that will be effective in conditions were the MT is spatially inhomogeneous.
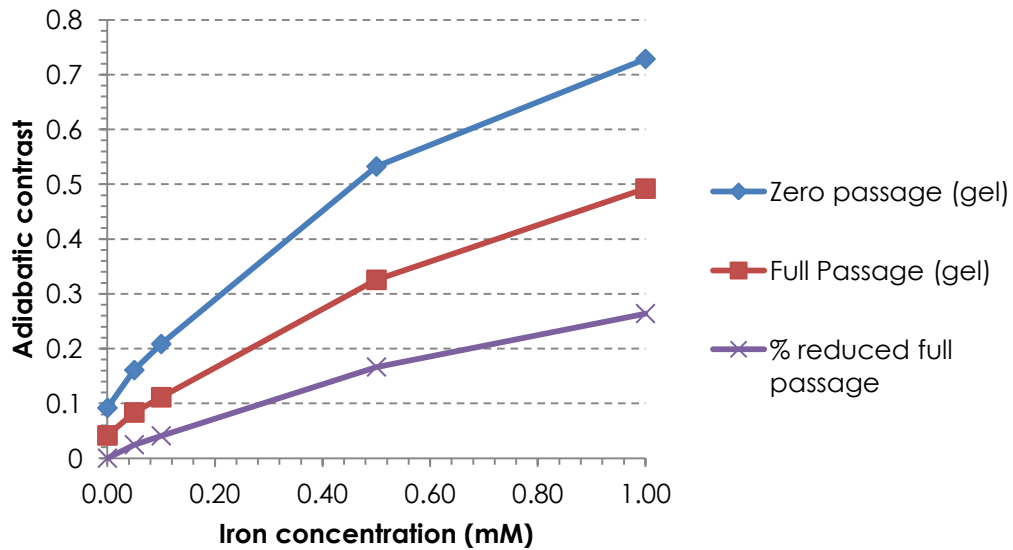
Figure 3.7: Relative reduction of adiabatic full passage contrast

73

When the previously proposed method of doubling the full passage contrast and subtracting the zero passage contrast is applied, the result is a contrast curve with a zero crossing and increased linearity. Figure 3.7 shows that even though the MT compensated measurement did not require any *a priori* sample information, the additional contrast component is nearly completely removed and the contrast is nulled for a zero iron concentration. In fact, compared to Figure 3.6 where an additional contrast component is assumed and the curve is shifted, the contrast measure from the proposed MT compensated approach appears more linearly correlated with iron concentration than either the full or zero passage pulse prepared contrast measurements.
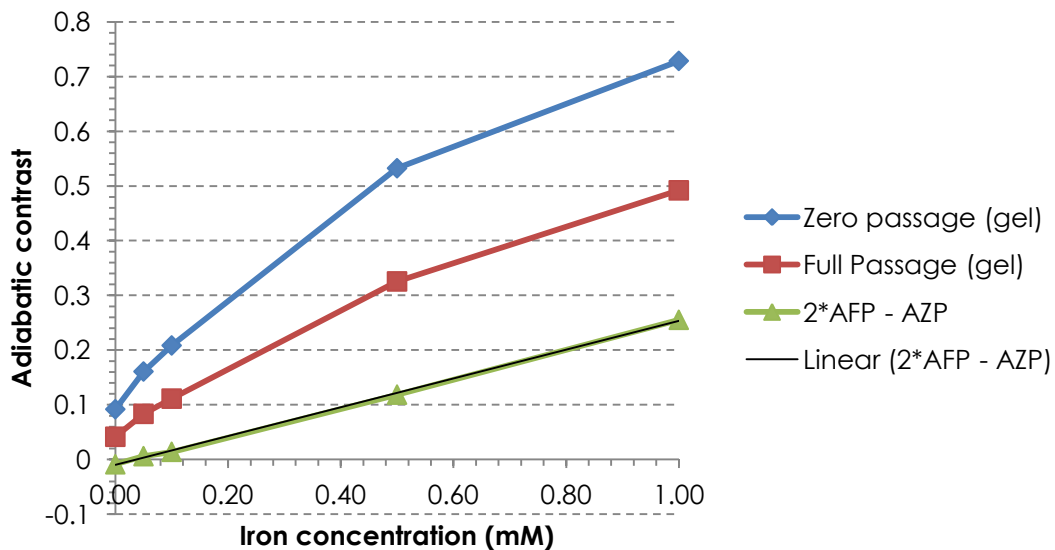
Figure 3.8: The magnetization transfer compensated method is more linear

Compared to the linear correlation coefficients of the full ($R^2 = 0.9842$) and zero ($R^2 = 0.9662$) passage pulse prepared techniques, the linear correlation of the MT compensated contrast is indeed increased ($R^2 = 0.9994$). However, Figure 3.9 shows that this high degree of linear correlation does include slightly negative contrast slightly at the zero iron concentration. This measurement may be a result of the decreased saturation effect of the second adiabatic pulse. But overall, these pulses achieve their desired effects and present a potential mechanism to increase the specificity of the contrast measurement to the presence of iron oxide nanoparticles while simultaneously acquiring contrast images weighted to both the zero and full passage pulses.
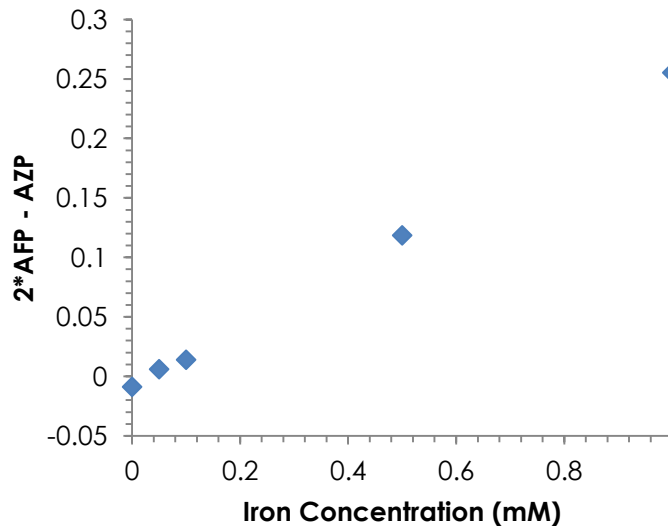
Figure 3.9: Magnetization transfer compensated adiabatic contrast

3.3.3 Characterizing the Effect of B_1 and Field Inhomogeneity

The sensitivity of nanoparticle quantification to the parameters of the imaging system is also important, affecting the accuracy of the measurement within an image acquisition as well as the reproducibility of the results between acquisitions. Though adiabatic pulses are often used with surface coils for RF transmission because of their relative robustness and uniformity, if the adiabatic preparation pulse approach is very sensitive to inhomogeneities in the static or applied fields, it would be a significant concern for translating a quantitative method. In this section, the sensitivity of the adiabatic contrast measurement to the peak power and frequency offset of the preparation pulse is characterized.

According to theory, once the adiabatic condition is fulfilled and adiabatic full passage is achieved, further increases to the maximum B_1 power will not affect the final flip angle. Therefore, for the case of nanoparticles in solution, increasing the peak pulse power past the level at which the adiabatic condition has been met should not greatly affect the contrast. Figure 3.10 confirms this hypothesis as doubling the minimum voltage necessary to fulfill the adiabatic condition does not dramatically change the measured contrast, even though the peak applied power is now near the voltage limit of the coil. However, there are more subtle changes in the quantification, as there does appear to be a trend of increasing contrast with increasing power. While the origin of this effect is not clear, the contrast converges for power beyond this threshold.
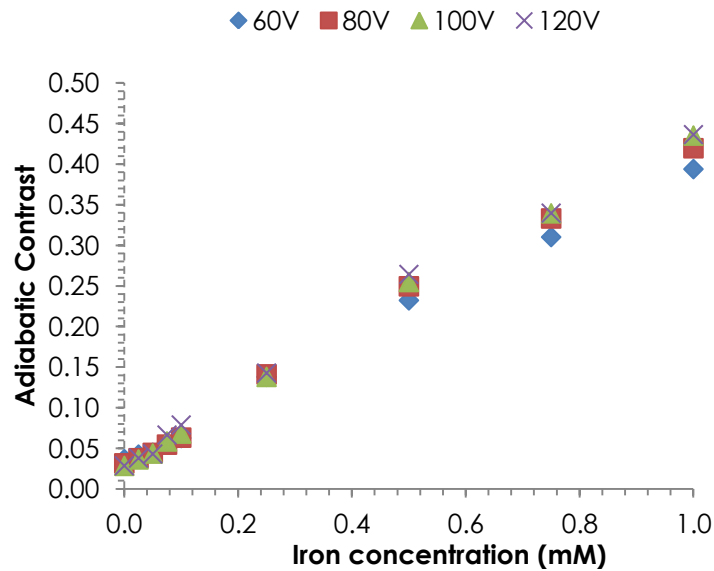
Figure 3.10: Adiabatic contrast in solution with increasing B1 power at 3 Tesla

Resonance frequency inhomogeneities and offsets over the imaging region of interest are a second factor that could confound nanoparticle quantification. For techniques where the off resonance is saturated, this can be a major concern, since the quantification is directly correlated with the single off resonance frequency. Inhomogeneities in the applied and static fields can lead to variable relationships between the applied and local resonances, and if these correlations are spatially or temporally varying, they can impede nanoparticle quantification either within or between sample measurements. Figure 3.11 shows that when the applied pulse is offset by 50, 100 and 250 Hz the contrast is indistinguishable from the zero frequency offset. Since the preparation pulse uses a 1760 Hz frequency sweep, the uniformity of the contrast for these offsets is expected. Within the bandwidth of the frequency sweep, the adiabatic pulse performs the inversion as expected while remaining sensitive to spins diffusing

77

through the fluctuating gradients around the particles. However, for frequency offsets beyond the bandwidth of the frequency sweep the contrast is substantially reduced. Using the frequency sweep, rather than a single saturation frequency, allows the adiabatic pulse prepared technique to produce robust nanoparticle quantification in the presence of magnetic field inhomogeneities, as are expected in *in vivo* applications.
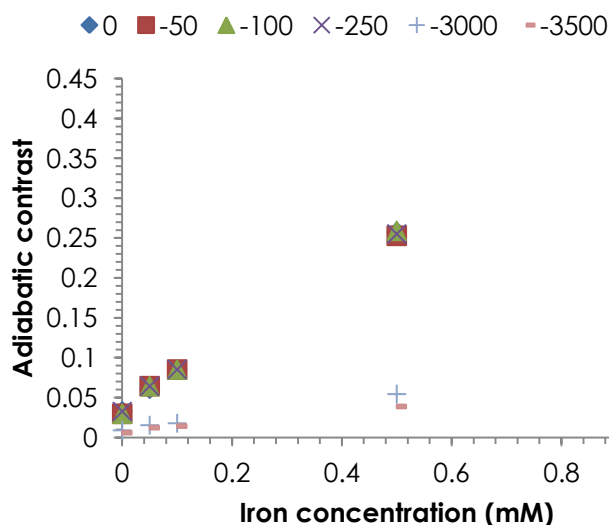
Figure 3.11: Adiabatic contrast frequency offset dependence (Hz)

In order to more fully characterize the relationship between contrast quantification and the applied frequency offset, the adiabatic contrast of pure water was measured at 9.4 Tesla with a smaller, stepwise increasing frequency offset. Figure 3.12 shows the expected near zero contrast for both offsets within the frequency sweep and outside the frequency sweep, as spins are either fully inverted or returned to their original orientation. However, near the cutoff frequency of the sweep there is a measurable

contrast. When the measured contrast is compared to the simulated M_z magnetization of the adiabatic inversion from the Bloch equation shown in Figure 1.5, the adiabatic contrast detected from pure water can be explained by the non-zero transition of average M_z magnetization between the flat regions inside and outside the frequency sweep. Within this region, spins do not perform within the adiabatic regime, and thus the apparent adiabatic contrast is a function this transition effect, rather than the presence of iron oxide nanoparticles. Importantly, since the range of the frequency sweep can be defined, a wide enough sweep for a given application can always be prescribed.
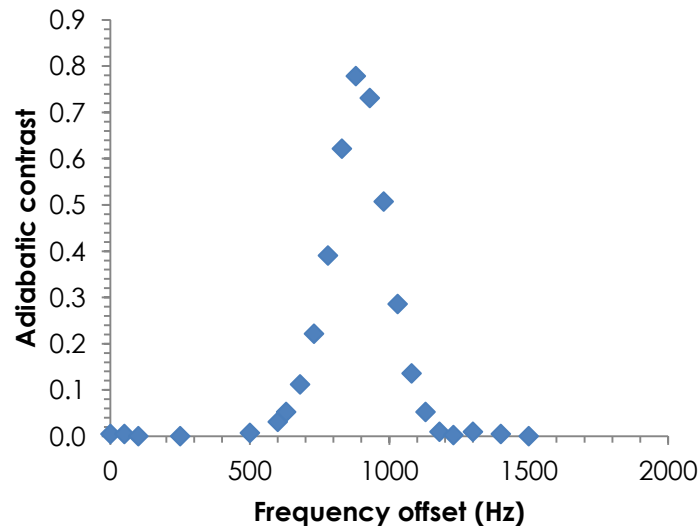
Figure 3.12: Adiabatic contrast in water phantom with varying frequency offset

3.3.4 Quantifying the Diffusion Dependence of Adiabatic Contrast

Changing the diffusion rate of the spins surrounding the nanoparticles may either increase or decrease the adiabatic contrast, since the diffusion rate affects the number of nanoparticles that are exposed to the strong magnetic field gradients surrounding the nanoparticles and the amount of time the spins spend near these gradients. To investigate whether the adiabatic approach was sensitive enough to detect changes in the diffusion rate, PEG-400 was added to the phantoms to increase the viscosity and decrease the diffusion rate. Figure 3.13 shows that while there is little change for the 0.0 mM samples without particles added, there is a clear trend of increasing adiabatic contrast with decreasing diffusion rate for each nanoparticle concentration.
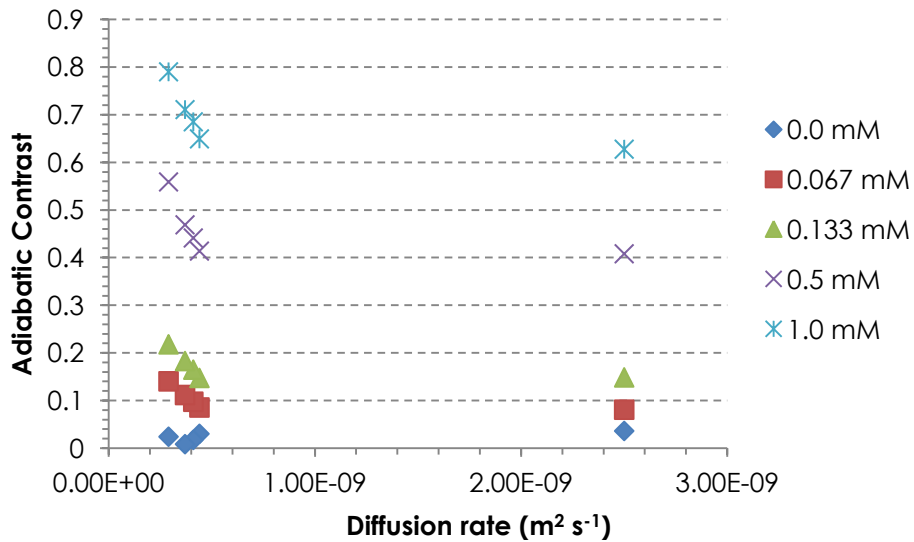
Figure 3.13: Adiabatic contrast as a function of diffusion rate

In order to quantify this relationship, the slope of each PEG-400 doped particle concentration was measured using a linear correlation. This slope represents the change

in adiabatic contrast as a function of the change in the diffusion rate, or the sensitivity of the contrast to the diffusion rate. Figure 3.14 shows that the sensitivity to diffusion rate increases with increasing iron concentration, with the highest two nanoparticle concentrations having the highest diffusion sensitivity.
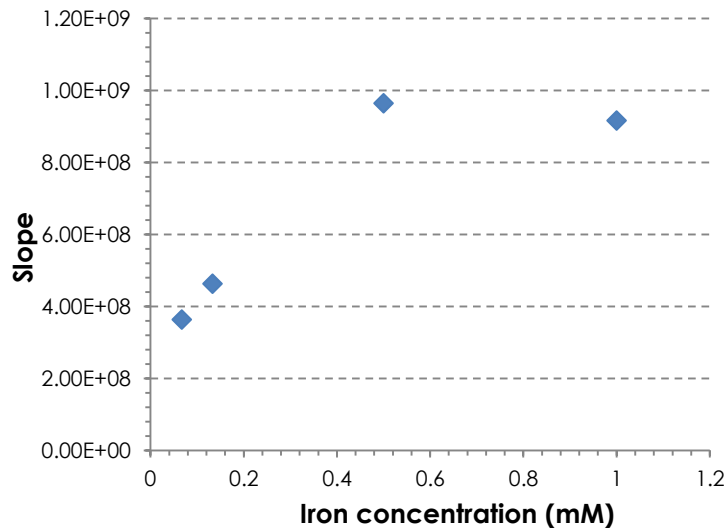
Figure 3.14: Sensitivity of adiabatic contrast to diffusion at varying iron concentrations

These results suggest that the decreased diffusion rates allow more spins, which would have otherwise diffused through the magnetic field gradients surrounding the particles, to remain long enough so that the local magnetic field gradients can cause the adiabatic condition to fail. The increased sensitivity of the higher iron concentrations to the diffusion rate may also suggest that there is an additive effect, since the distance between the nanoparticles is decreased. Perhaps as the diffusion rate is decreases, the effects of multiple nanoparticles combine to enhance the contrast generated.

3.3.5 Comparison of Adiabatic Contrast to Existing Methods

The contrast generated by the adiabatic pulse prepared technique was also compared to other methods of quantifying iron oxide nanoparticles such as transverse relaxation rate and off resonance saturation (ORS). Transverse relaxation rate ($R2 = 1 / T1$) was measured using a multi-echo, spin-echo sequence with subsequent exponential fitting for parameter estimation. Figure 3.15 shows that the there is a linear relationship between the adiabatic zero passage contrast and the transverse relaxation rate, especially for low iron concentrations. As was previously noted, at higher iron concentrations adiabatic zero passage contrast reaches an asymptote.
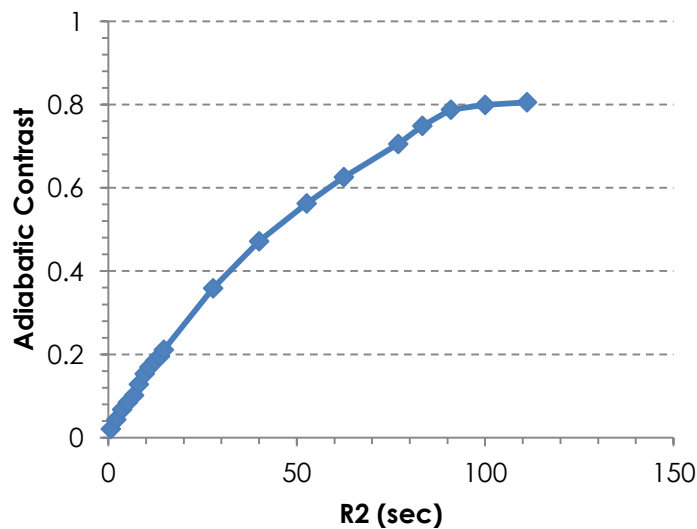
Figure 3.15: Correlation of adiabatic contrast with transverse relaxivity

Off resonance saturation is another method for generating contrast based on the microscopic magnetic field gradients surrounding the particles. In this approach, spins at a given off resonance frequency, corresponding to a shell surrounding the nanoparticle, are saturated. The number of spins that are saturated is dependent on the volume of the shell and the duration of the preparation pulse. Since with ORS the saturation can occur on a timescale shorter than the total preparation pulse duration, the effect on the contrast can be multiplied as spins continuously diffuse though the saturation shell and are replaced by fresh spins during the preparation, enhancing the contrast.
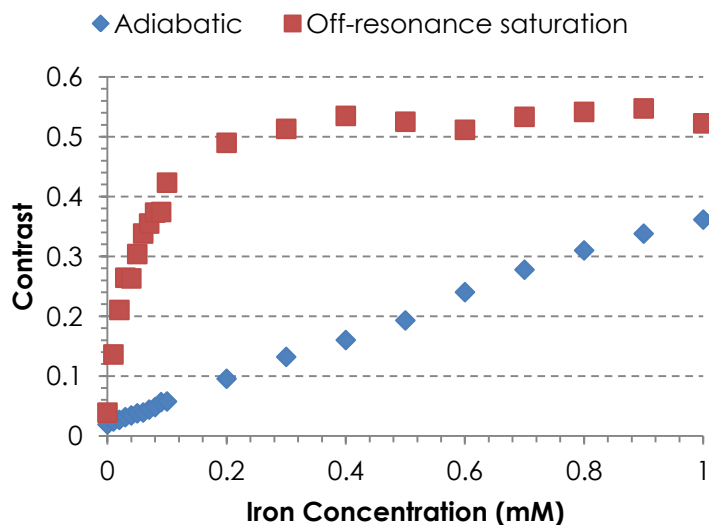
Figure 3.16: Adiabatic and off-resonance saturation contrast in solution at 3 Tesla

Figure 3.16 shows that while the adiabatic full passage contrast is linearly correlated with iron concentration over the entire range of iron concentration, the ORS

contrast is much more sensitive at very low iron concentration but becomes insensitive to iron concentrations greater than 0.2 mM. While the ORS technique reaches its asymptote significantly before an iron concentration of 1.0 mM, a linear contrast region can be identified between 0.0 and 0.1 mM. Even though the saturation of the contrast at higher iron concentrations is not ideal for iron quantification, the sensitivity of the technique to extremely low iron concentrations is an enormous advantage for targeted molecular imaging studies.
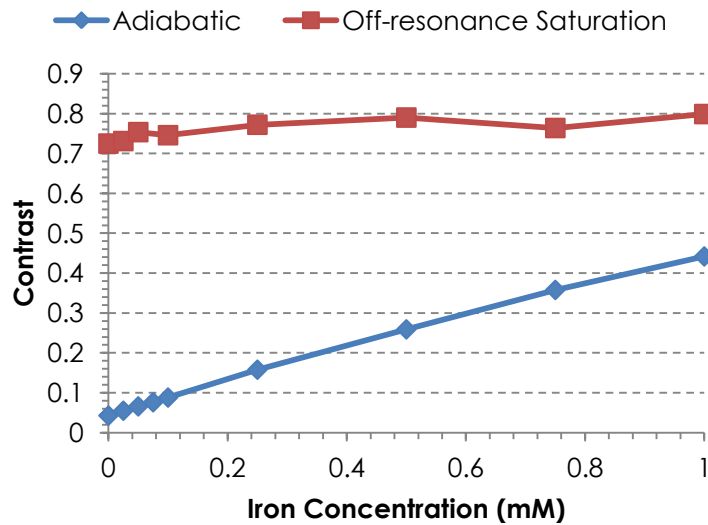
Figure 3.17: Adiabatic contrast and off-resonance saturation contrast in 2% agarose gel at 3 Tesla

However, a significant obstacle for the ORS approach is to only saturate the off resonance spins that are associated with the iron oxide nanoparticles. Figure 3.17 shows that when the nanoparticles are embedded in 2% agarose gel there is a substantial contrast component in the off resonance saturation contrast that is iron oxide independent. While

closer inspection reveals that the ORS contrast increases with increasing nanoparticle concentration, this change is largely masked by the additional off resonance contrast originating from the agarose. As has been described for the adiabatic contrast, even though there is a small additional contrast component, the overall relationship between contrast and iron concentration remains much more apparent.
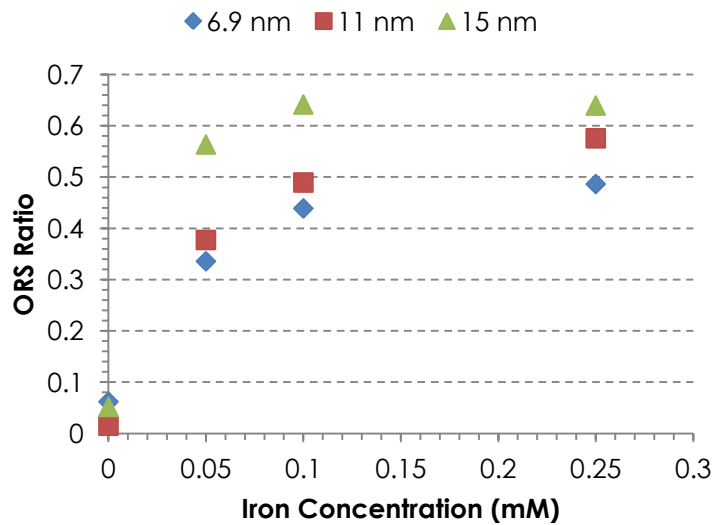
Figure 3.18: Off-resonance saturation contrast of varying iron-oxide core sizes in solution at 3 Tesla

These results were replicated with the nanoparticles of different iron oxide core diameters. Figure 3.18 shows that while the relative level of contrast is much greater with ORS compared to the adiabatic pulse prepared approach, the quantification still saturates within the range of concentrations studied. Notably, the larger iron oxide cores also produce the greater ORS contrast, as was the case for the adiabatic contrast.

3.3.6 Comparison to Frequency Selective Inversion

While the frequency selective properties of adiabatic pulses have been described theoretically and with Bloch equation simulations, other pulses have frequency selective properties and may be suggested to accomplish similar aims of generating nanoparticle contrast. In fact, the IRON method uses this concept to invert and null the on resonance signal for subsequent imaging the off resonance component. With this in mind, a 2 millisecond sinc pulse with a 180 degree flip angle was applied in place of the adiabatic full passage. The objective of this study was to test the hypothesis that the mechanism as described with the fulfillment of the adiabatic condition could not be replicated by applying a conventional, frequency selective 180 degree pulse. Samples with varying nanoparticle concentrations and diffusion rates were imaged, and the contrast measurement was calculated identically to the adiabatic contrast. While measurable contrast was expected from the frequency selected inversion in the presence of the iron oxide nanoparticles, the quantitative relationship between the measured contrast and the iron concentration was unclear.
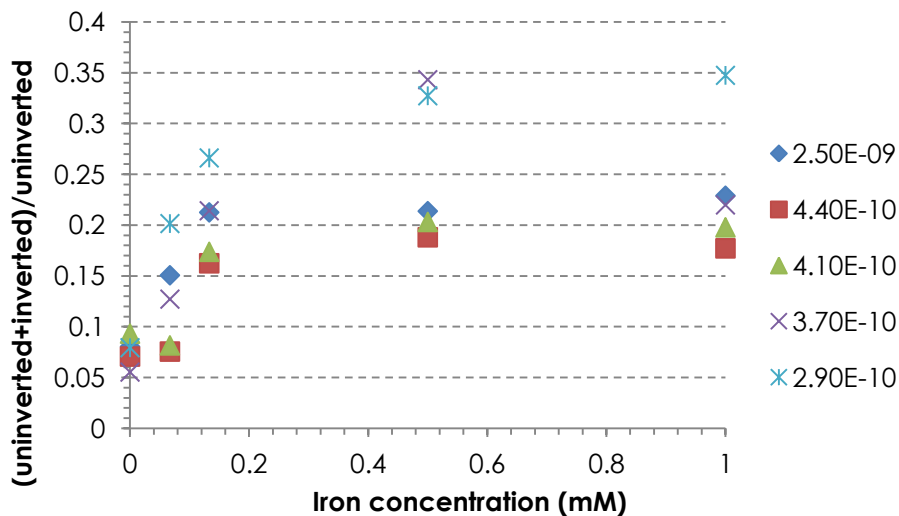
Figure 3.19: Frequency selective pulse prepared contrast in varying diffusion environments

Figure 3.19 shows that while the contrast generally increases with increasing iron concentration, the calculated contrast is neither monotonically increasing within each condition, nor linearly correlated with iron concentration for any of the conditions. These two factors highlight the robustness of the adiabatic contrast measurement to inhomogeneities and the linearity of contrast correlation, which are consequences of the adiabatic preparation pulse. While techniques sensitive to off resonance show increased intensity in the presence of the field inhomogeneities introduced by iron oxide nanoparticles, only the adiabatic preparation pulse that is able to generate a linear contrast that is insensitive to many other off resonance factors that are not reflective of the local nanoparticle concentration.

3.3.7   Adiabatic Contrast is Linearly Correlated with Intracellular Iron

Concentration *In Vitro*

In the final section of this chapter, two complementary applications will be used to test the potential of the adiabatic pulse prepared method for quantitative cellular imaging. First, cells incubated with iron oxide nanoparticles and embedded in agarose gel were imaged with the full passage preparation. This cellular model introduces both MT effects as well as non-uniformly distributing the nanoparticles within the cell after uptake. After imaging, biochemical analysis of the samples was used to quantify the true iron concentration. Figure 3.20 show that the adiabatic contrast remains linearly correlated with iron concentration ($R^2 = 0.9491$) in the cellular imaging experiment. While there are some MT effects present, as the iron concentration increased the contrast similarly increased and was detectable over the baseline contrast.
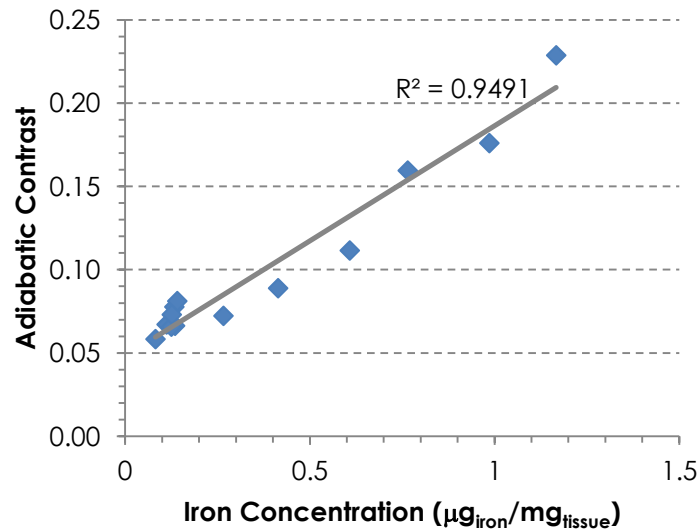
Figure 3.20: Adiabatic contrast correlation with intracellular iron concentration at 3 Tesla

One challenge arising from the cellular iron quantification was that while the iron concentration was measured over the entire sample, the adiabatic contrast measurement only interrogated a subset of the iron loaded cells in a 1 mm slice though the sample. In order to have another point of comparison, the R2 was calculated for the slice corresponding to the adiabatic contrast measurement. Figure 3.21 shows that the linearity of the correlation is increased ($R^2 = 0.9733$), especially for the lower iron concentrations. This is likely because for lower iron levels the inhomogeneous distribution of a smaller number of cells corresponds to a greater sensitivity to the imaging slice selected. By measuring the transverse relaxation rate and adiabatic contrast of the same subset of cells, the two methods of quantification are better correlated, as expected.
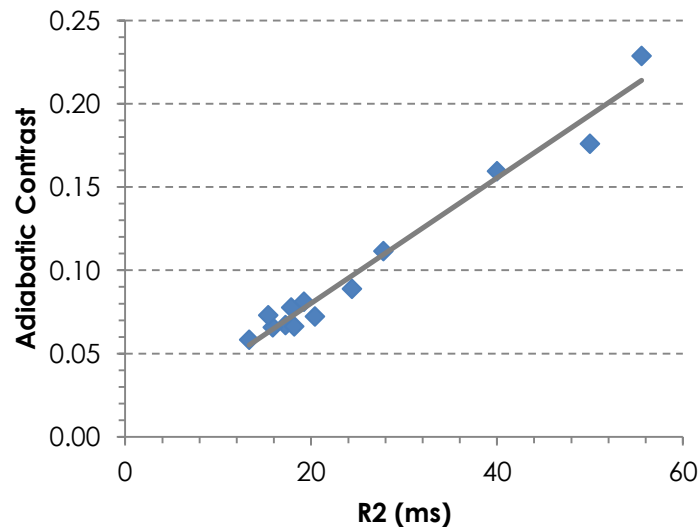
Figure 3.21: Adiabatic contrast correlation with transverse relaxivity of cell samples

For comparison, these cell samples were also imaged with the ORS technique. Figure 3.22 shows many similarities with the previous results using iron oxide particles embedded in agarose gel. For the cellular imaging application, ORS is again very sensitive to low iron concentrations, but the contrast measurement saturates at higher iron concentrations. It is also important to note that the absolute measure of the contrast starts with a high baseline measurement, and as was previously shown, this additional contrast that is due to the cell structure and agarose gel can confound nanoparticle quantification. Overall, optimizing the ORS technique may provide significant improvements by reducing the baseline level of contrast and increasing the sensitive, linear range, but the characteristics of the two techniques appear similar in the cellular imaging experiments as in the phantoms.
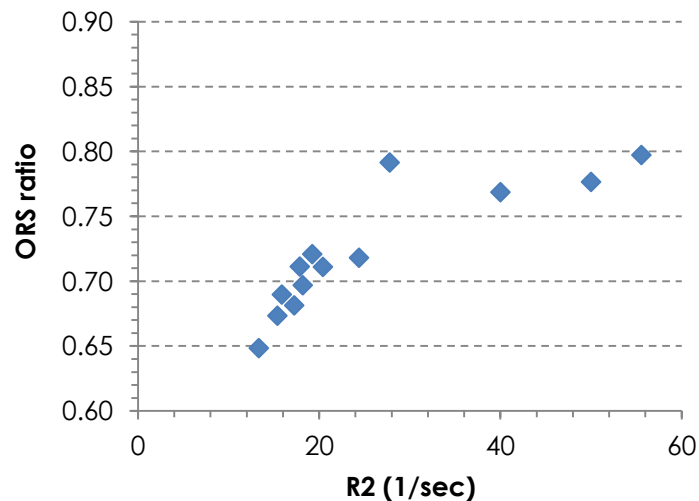
Figure 3.22: Off-resonance saturation contrast correlated with cell sample transverse relaxivity

Finally, the proposed technique was applied to an MR gene reporter that is being simultaneously developed. Figure 3.23 shows that there is a significant difference in adiabatic contrast for samples incubated with and without supplemented ferric citrate. By adding the iron supplement, the cells make nanoparticles that can serve as MR contrast agents. While not an extensive characterization, these results provide further evidence that the approach may be appropriate for molecular MR imaging.
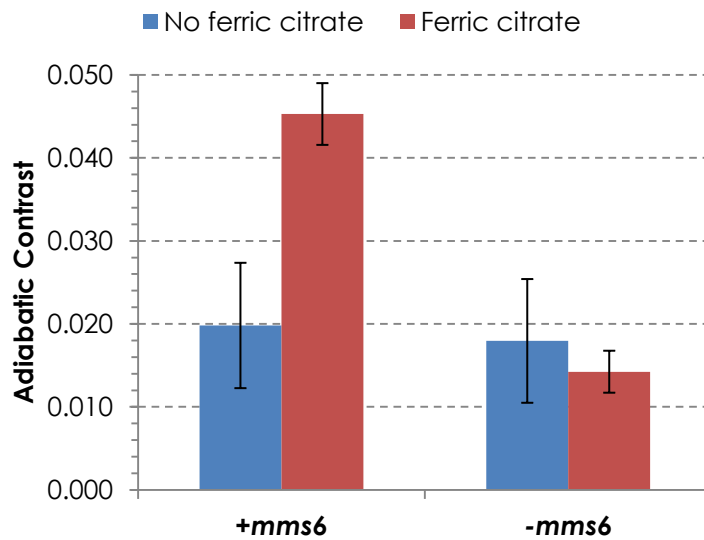
Figure 3.23: Adiabatic contrast detection of with the *mms6* MR reporter gene

3.4 Discussion and Conclusion

In this chapter the adiabatic pulse prepared mechanism was extended in more realistic models of iron quantification. It was shown both that the overall technique is relatively insensitive to several challenges to quantification as well as that new approaches can be developed, while remaining sensitive to the same underlying contrast mechanism. Finally, the ability of the method to quantify iron concentration *in vitro* suggests that it is appropriate for quantitative molecular imaging applications.

The proposed magnetization transfer compensated approach using adiabatic full and zero passage pulses produces a contrast that *(a)* does not have the additional contrast component present in the agarose phantoms, and *(b)* is more linearly correlated with iron concentration. The first point follows from the theory, and the second point is likely a due to the fact that the quantification is specific to the measured samples. If a single contrast component was assumed to be added to all the agarose samples, any individual variation between the samples would not be accounted for by the technique. However, since the diffusion and power effects on one sample quantification are independent from the effects on a second sample, the proposed method produces more accurate iron quantification even when comparing between samples with different molecular environments.

However, it is important to note that while this approach remains sensitive to the diffusion of the spins, the penalty for the decreased sensitivity to MT is a decrease in the nanoparticle specific contrast to noise ratio. If we assume an average diffusion distance for a preparation pulse, *d*, then the average diffusion distance for during a preparation pulse that is twice the duration is, *sqrt(2) · d*. Therefore from the theory proposed, the magnitude of the MT compensated contrast should be reduced by, *2 – sqrt(2)*. This yields an expected decrease in measured contrast by 58.6%, which is in good agreement with the experimental results. While the duration of the pulses can be changed, the main objective of the approach is to decouple the power and the diffusion distance, which

requires keeping many of these variables constant between the two measurements. Future developments may aim to quantify this additional component to create a map that can be subtracted from the contrast image, or this map may be of interest for independent MT measurement applications. In this approach only the relatively small MT specific contrast component is removed, rather than simultaneously sacrificing some of the desired diffusion based contrast.

The overall insensitivities to MT, B_1 and frequency offset are important in developing a method for quantitative imaging. This insensitivity is a function of both the mechanism of the contrast as well as the inherent properties of the adiabatic pulse. Since molecular imaging in animal models will likely be performed with transceiver surface coils, the uniform flip angle of the method alone is important. Other characteristics of the contrast measurement, like the sensitivity to the prescribed frequency sweep, present opportunities to define the pulse parameters and to modulate the detected contrast. Both the frequency at which the transition occurs and the steepness of the transition can be defined by the parameters of the hyperbolic secant pulse and tailored for the specific application.

The comparison of the adiabatic contrast with the ORS technique showed that the two approaches may be complementary. While ORS is extremely sensitive to very low iron concentrations, the adiabatic technique is linearly correlated over a much larger range of iron concentrations used in molecular imaging. This is not surprising when the theoretical foundations of the two techniques are compared. While in ORS spins are continuously cycled through and saturated in a shell surrounding the nanoparticle, in the adiabatic technique each spin's random walk diffusion during the adiabatic preparation pulse determines its state for the imaging sequence. While the adiabatic technique is more specific for the nanoparticles, the ORS method is especially intriguing for molecular

applications where very low particle concentrations are expected. Incidentally, both techniques have been shown to be sensitive to changes to the diffusion rate of the sample.

Finally, the adiabatic pulse prepared technique is able to quantify the iron concentration of cells incubated with iron oxide nanoparticles. These studies add several complicating factors including *(a)* the unequal distribution of nanoparticles within the cell including clustering in lysosomes, and *(b)* restricted diffusion associated with the cell and organelle membranes. However, the adiabatic approach is able to quantify the relative iron content present in varying numbers of cells as confirmed by molecular measurements. Future studies will aim at characterizing how the type of iron oxide nanoparticle and the type of cell affects the quantification.

In conclusion, the proposed adiabatic pulse prepared approach is able to quantify iron oxide nanoparticle concentrations appropriate for molecular imaging within realistic phantom and cellular models. The flexibility of the proposed mechanism allows for the measurement to remain sensitive to the desired diffusion effects while mitigating the undesired effects arising from the preparation pulse on the sample. Along with other techniques, the adiabatic pulse prepared method can be used as a robust method of nanoparticle quantification in molecular MR imaging.

CHAPTER 4

INVESTIGATING ADIABATIC PULSE PREPARED CONTRAST IN VIVO

While the adiabatic pulse prepared sequence produces a contrast sensitive to iron oxide nanoparticles that is both quantitative and robust, translating this approach into *in vivo* systems imaging is not simple. For a technique to be generally applied in research or clinical settings, technical limitations, in addition to the challenges of live animal imaging, must be addressed. Fortunately, since many of the initial studies were conducted on a 3 Tesla clinical MR scanner, some technical limitations such as the clinically regulated specific absorption limit (SAR) have always been fulfilled. However, imaging phantoms and *in vitro* samples has allowed for very long image acquisition times to maximize the SNR and the contrast quantification.

The first part of this chapter extends the utility of the adiabatic pulse prepared sequence by combining the same adiabatic contrast mechanism with methods of acquiring images much faster. This reduction in total scan time is not only necessary for clinical translation because of the limited availability of clinical scan time, but subject motion and the total number of slices acquired are also hurdles for translation. In addition to the initial adiabatic pulse prepared standard spin-echo (SE) sequence, adiabatic pulse prepared Turbo Spin-Echo (TSE), Half-Fourier Acquisition Single Shot Turbo Spin Echo

(HASTE) and Fast Low Angle SHot (FLASH) sequences are developed. These different image acquisition schemes yield consistent contrast quantification but with a dramatic reduction in image acquisition time. In the second section, an experiment is designed where iron oxide nanoparticles are intravenously administered to mice and allowed to accumulate in the liver over a period of 24 hours. Then the mouse liver is imaged, and the contrast measured by the adiabatic pulse prepared sequences is correlated with the total liver iron measured by biochemical analysis. Together, these studies show that the proposed approach can be modified and translated to *in vivo* imaging based on the theoretical foundation of the contrast mechanism.

4.1 Introduction

Targeted molecular imaging may be the most exciting and ambitious application of iron oxide nanoparticles. While in cell tracking the cell of interest is generally known and labeled, targeted imaging aims to hone the nanoparticles to cells in the body based on their physiological or molecular characteristics. When the contrast agents are combined with pharmaceutical therapy (116), these probes can characterize the pathophysiological molecular markers while simultaneously delivering therapy. As contrast agents are designed to target specific biomarkers of disease and changes in physiology, a natural disease of interest is cancer. Here, the expression of different cell surface proteins compared to healthy tissue provides disease specific targets for the nanoparticles (117). Additionally, by characterizing the molecular and physical characteristics of the tissue,

probes can be designed to selectively accumulate in the tissue of interest and provide contrast in MR images.

Targeted contrast agents for *in vivo* imaging can generally be divided into either passively or actively targeting (43). Passive targeting describes the process of contrast agents accumulating in tissues based on factors other than their molecular profile. Particles may be phagocytosed differently by different cell types, escape through the leaky vasculature of a tumor, or accumulate in tissues based on the physical parameters of the particles and the vessels. While these changes provide information about the state of the cells and the tissues, they are not designed to detect or quantify the expression of molecular markers of cancer. Active targeting conjugates a specific molecule to the nanoparticle coating that can bind to the target of interest. Once the contrast agent binds to the molecule, the complex may be taken up by the cell where the iron oxide nanoparticle will continue to decrease the transverse relaxation rate (118). Generating detectable contrast is a challenge for this approach. While a level of molecular specificity and sensitivity similar to PET remains a goal, new approaches may be required to enhance the accumulation of the particles and to amplify the changes in the MR signal.

Imaging macrophages after intravenous iron oxide nanoparticle injection was one of the first clinical applications of passively targeted particles (119). It was observed that the particles were phagocytosed by specialized macrophages in the liver known as Kupffer cells. These normal cells are absent in cancerous tissue, and therefore regions that are not responsive to the contrast agent raise the suspicion of malignancy (120).

Feridex IV (Advanced Magnetics, Lexington, MA) was approved by the FDA for aiding in the diagnosis of liver masses by MRI (121). Due to their predilection for phagocytosis and the ubiquitous roles of the immune system in the human body, studies characterizing many other disease processes including autoimmune (122) and atherosclerotic plaque formation (123) have been designed using the same principles but with particles selected for the specific disease application.

Changes in vascular physiology and vessel integrity can also be major drivers for nanoparticle accumulation. While particles can be designed to circulate for longer periods of time, by avoiding being trapped in the capillaries or excreted in the kidney, changes in vessel integrity can lead to the escape of the particles out of the circulation. Tumor angiogenesis produces leaky vessels where particles extravagate and passively accumulate in the tumor tissue (124). While such a crude method may have limited applications for clinical cancer screening, a complementary method has been explored for screening lymph nodes for metastatic disease based on nanoparticle accumulation (125). However in the case of lymph nodes, the MR intensity is less affected by the contrast agent in metastatic tissue (126). The advantage of these passive accumulation methods is that higher doses of contrast agent can drive the accumulation of more nanoparticles in the tissue, without the need for cellular binding and uptake. However, if the goal is to develop a method for quantifying tissue biology on the molecular level, passive targeting is insufficient.

Active targeting uses molecules conjugated to the surface of the nanoparticle to increase the binding and localization of the particles. For these approaches, antibodies and other proteins can be linked to the surface coating of the iron oxide to increase molecular specificity (127). Prominent examples include imaging cancer and angiogenesis by targeting the Her-2/neu receptor (128) and VCAM-1 (129). Non-invasive methods for quantifying receptor expression allow disease progression and treatment response to be monitored. As these molecular changes precede the anatomical and physiological changes conventionally measured by MRI, molecular imaging methods provide new biological insights. However while the number of potential molecular targets is as expansive as the diverse molecules expressed in the cell surface, the challenge generating sufficient MR contrast based on a relatively small number of molecules remains. Additionally, since the particles are often administered intravenously and then must be honed to the tissue of interest, localization of the contrast agent alone can be a significant obstacle.

Despite these challenges, MRI remains a promising modality for *in vivo* molecular imaging as a non-invasive and safe method for acquiring high resolution images with good soft tissue contrast. Also, the growth of MRI in the clinical setting cannot be underestimated for potential clinical translation. With these developing clinical and research applications for human and animal imaging in mind, the following work aims to develop an adiabatic pulse prepared approach appropriate for *in vivo* imaging and demonstrate it in an animal model. The sensitivity of the proposed method to the microscopic magnetic field inhomogeneities surrounding the nanoparticles should present

99

many advantages for contrast specificity to the nanoparticles as has been detailed. However, translation into *in vivo* models is challenging for nearly all imaging techniques, since the varied environments and cardiac and respiratory motion can significantly erode the quality of the images and the performance of the contrast mechanism.

In this chapter, the *in vivo* potential of the adiabatic pulse prepared contrast method is investigated first by overcoming a known technical challenge and second by testing a passive targeting model with *ex vivo* validation. Since a standard spin echo sequence requiring several minutes to acquire one image is insufficient for live animal imaging, adiabatic pulse prepared TSE and HASTE sequences are implemented. These imaging techniques maintain the adiabatic contrast by leaving the preparation module untouched, but they significantly reduce the total imaging time by acquiring multiple lines of k-spaces following a single adiabatic preparation. Finally, iron oxide nanoparticles that preferentially accumulate throughout the mouse liver are administered intravenous in different doses and allowed to circulate and accumulate before quantitative imaging. The livers are then removed and biomolecular methods are used to quantify the iron content in the liver, which is then correlated with the image contrast. Together, these aims demonstrate the flexibility of the approach and validate the quantification of the technique for *in vivo* imaging.

4.2 Methods

The *in vivo* potential of the proposed technique is investigated by applying the adiabatic contrast mechanism to a passive targeting model. To accomplish this objective *(a)* sequences with reduced total imaging times compatible with the *in vivo* studies but without compromising image contrast were implemented and validated, and *(b)* an *in vivo* passive targeting experiment was used with *ex vivo* quantitative tissue analysis to correlate the imaging results with the iron content.

4.2.1   Developing Alternative Imaging Strategies for Adiabatic Pulse Prepared Sequences

In order to decrease the total contrast acquisition time, multiple lines of k-space were acquired following a single adiabatic preparation pulse. Similar to the adiabatic pulse prepared spin-echo sequence, adiabatic pulse prepared Turbo Spin Echo (TSE) and Half-Fourier Acquisition Single-Shot Turbo Spin-Echo (HASTE) sequences were developed in the Siemens IDEA environment. For the TSE sequence, multiple refocusing pulses are applied following the excitation acquiring multiple lines of k-space within a single TR. The number of echoes acquired is defined by the Turbo Factor (TF), with a higher TF reducing the total scan time for a given TR. However, an important consideration, especially for higher TFs, is that the signal magnitude decreases in time with the T_2 decay envelope. HASTE is an extreme extension of this approach with all the echoes being acquired after a single excitation. The acquisition time is further decreased

by using the symmetry of k-space to reduce the total area of k-space acquired. The T_2 weighting of the HASTE approach is therefore even greater than for the TSE sequence.

All sequences were designed within the Siemens IDEA programming environment and implemented on a 3 Tesla Siemens Magnetom Trio (Siemens Medical Solutions, Malvern, PA). The preparation pulse parameters were identical to the previous spin-echo sequence with a 10 millisecond hyperbolic secant pulse applied prior to the imaging scheme. The TR was extended to 10 seconds to allow greater recovery of the spin system. Other imaging parameters were identical to the conventional spin-echo experiments with the notable exception of the echo time. Since the effective echo time of the accelerated imaging sequence is a function of the TF, the total imaging time and the effective echo time are correlated. However, since the echo time is the same for the prepared and non-prepared images, the calculated adiabatic contrast is only a function of the adiabatic preparation pulse and not the effective echo time. Iron concentrations were selected from 0 mM to 0.25 mM, a range in which sufficient signal remained for contrast calculation even at long effective echo times.

4.2.2   Iron Oxide Nanoparticle Administration for Mouse Liver Imaging

An experiment was designed to test the ability of the method to quantify low concentrations of nanoparticles in a living animal model. By experience, different doses of intravenously administered particles that predominantly accumulate the mouse liver

were used to generate different *in vivo* liver iron oxide nanoparticle concentrations. The nanoparticles used were amphipilic triblock copolymer coated iron oxide nanoparticles with a core size of 15 nm and a zeta potential of -30 mV (Ocean NanoTech, Springdale, AR). In each sample group, three 4-6 week old female balb/c mice received a single intravenous dose of nanoparticles (1, 2.5, 4, or 5 $mg_{iron}/kg_{body\ weight}$). The particles circulated and accumulated in the liver tissue for 24 hours before MR measurement.

Imaging was performed on a 3 Tesla Siemens Magnetom Trio (Siemens Medical Solutions, Malvern, PA). The animals were anesthetized with ketamine/xylazine and two animals were placed side-by-side inside the transceiver wrist coil. The imaging parameters used were similar to the phantom experiments at 3 Tesla: TR: 5 sec, TE: 14 msec, TF: 4, Field of View: 90 mm x 90 mm, Matrix: 128 x 128. The turbo factor used was a compromise between the objectives of decreasing the duration of the image acquisition and generating sufficient signal for accurate quantification despite T_2 decay. Additionally, an ultrashort echo time (UTE) sequence was used for comparison: TR: 8.19 msec, TE: 0.07 and 5.06, slice thickness: 0.52 mm, Matrix: 192 x 192, slices: 192, phase encode directions: 48000, Field of View: 99 x 99. The ultrashort echo time allows the T_1 effects of the iron oxide nanoparticles to be imaged, producing an increased signal.

Following the imaging experiments, the animals were sacrificed and the liver tissue was removed for biochemical analysis. The organ was digested with nitric acid and the 1,10-phenanthroline test was used to quantify the total iron content. A calibration curve of known iron concentrations was created within the range of liver iron

concentrations, and the liver iron was measured by spectrophotomeric comparison. The measured value for the animals administered iron oxide nanoparticles was then subtracted from the 0.32 mg_{iron}/g_{tissue} baseline liver iron concentration to yield a normalized iron concentration specific to the nanoparticles.

4.3 Results

4.3.1 Developing Different Adiabatic Pulse Prepared Imaging Techniques to Decrease Total Imaging Time

While the conventional spin-echo technique produces high quality images with relatively short echo time, the major disadvantage of this approach for translational work is the long image acquisition time. Since the total imaging time is a product of the number of k-space lines acquired and the repetition time, allowing for the relaxation of the spins before the next preparation requires at least 5 to 10 seconds for imaging at 3 and 9.4 Tesla. When this time is multiplied by an average matrix size of 128 or 256 lines, the total acquisition time for a single image quickly increases to more than 10 minutes. Since a second image is required without the preparation pulse, the total contrast imaging time may be impractical, especially for clinical translation. Fortunately, the adiabatic contrast is only a function of the preparation pulse, approximately 10 milliseconds in the current

studies. If the image acquisition period could be accelerated, the adiabatic contrast could be measured on the order of seconds rather than minutes.

Spin-echo based acquisitions were first explored, especially with the image quality gained in the presence of the large susceptibilities of the nanoparticles. Adiabatic pulse prepared TSE and HASTE sequences were implemented on a 3 Tesla clinical MR scanner to acquire multiple lines of k-space after a single preparation and excitation. With the TSE sequence, the number of k-space lines acquired after a preparation can be defined by the user at scan time. Increasing the number of lines increases the speed of the acquisition; however, it also increases the effective echo time of the image. This can be a significant tradeoff when imaging iron oxide nanoparticles as they can dramatically increase the transverse relaxation rate, and the adiabatic contrast calculation is not possible if there is no signal detected at the long effective echo time.

Adiabatic full passage contrast acquired with the TSE sequence and a turbo factor (TF) of 7 shows the familiar linear relationship of adiabatic contrast with iron concentration in Figure 4.1. The linear correlation of the contrast remains strong even though the total scan time has been decreased by a factor of 7: 15 nm $R^2 = 0.978$, 11 nm $R^2 = 0.9961$, 6.9 nm $R^2 = 0.9914$. Also, even though the effective echo time of the acquired images has increased and the signal intensity decreased, the calculated contrast is reproducible. Since the adiabatic contrast is the normalized difference of images of same effective echo time with and without the preparation pulse, the contrast is insensitive to the image acquisition parameters that affect the signal to noise ratio.
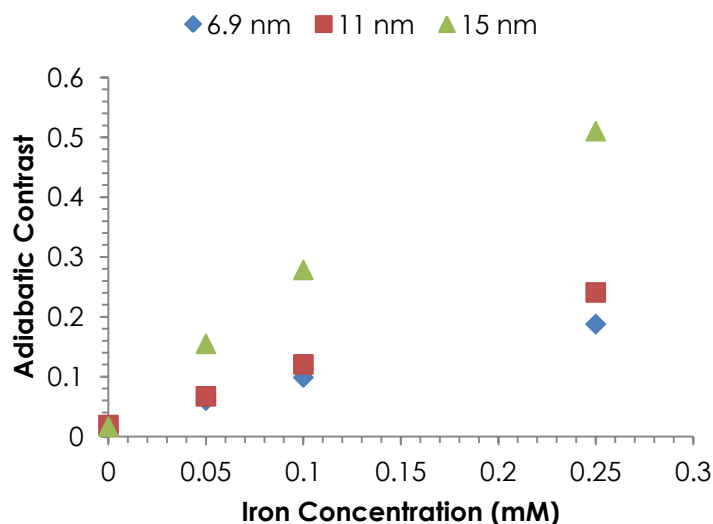
Figure 4.1: Adiabatic full passage contrast acquired with a Turbo Factor of 7 at 3 Tesla

To push the accelerated image acquisition further, an adiabatic pulse prepared HASTE sequence was implemented, using half-Fourier acquisition to acquire the entire image after a single preparation and excitation. Overall, Figure 4.2 shows a similar contrast relation to the TSE sequence, especially for the 6.9 (R^2 = 0.9932) and 11 nm (R^2 = 0.9977) iron oxide core sizes. However, the highest nanoparticle concentration does not maintain the linear relationship for the 15 nm iron oxide core size. For these conditions the high transverse relaxation rates and long effective echo times decrease the signal to noise ratio of the images, and the contrast asymptote begins to be reached. However, for the lower iron concentrations the HASTE sequence quantified the adiabatic contrast from images acquired in less than 5 seconds.
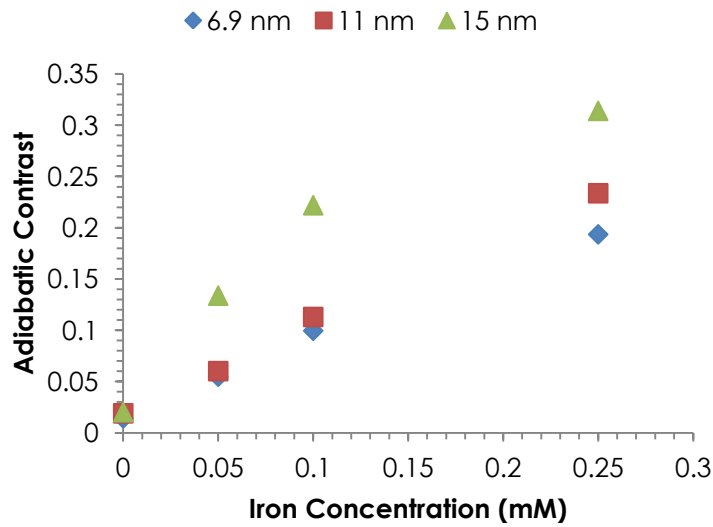
Figure 4.2: Adiabatic full passage contrast with single-shot HASTE acquisition

In order to test the hypothesis that the adiabatic contrast is only a function of the adiabatic pulse preparation, and not the image acquisition sequence, the contrast measurements of the conventional spin-echo, TSE with increasing TF and HASTE sequences were compared. Figure 4.3 shows that while there is nearly a factor of 100 difference between the longest and shortest image acquisition time, the contrast remains largely consistent. This is highlighted by focusing on the changes with increasing TF in the TSE and HASTE sequence in Figure 4.4. Here, it is clear that the particle quantification is not compromised by decreasing the imaging time. As long as sufficient image intensity can be acquired by the imaging sequence, measuring the contrast generated by adiabatic preparation pulse should be possible.
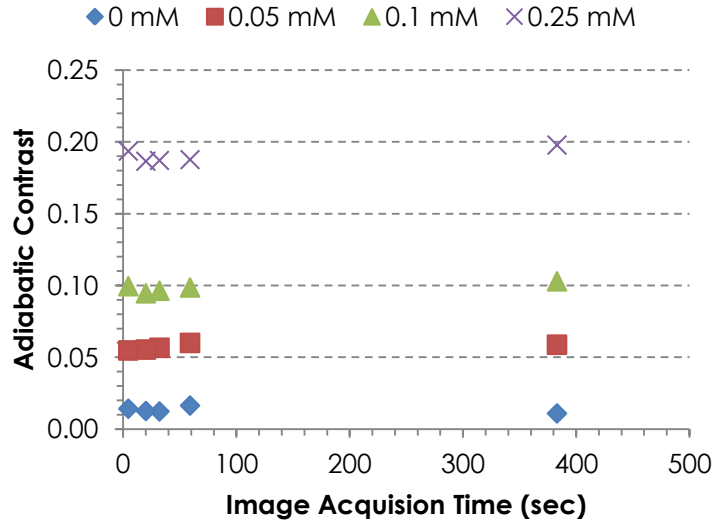
Figure 4.3: AFP contrast with varying acquisition time
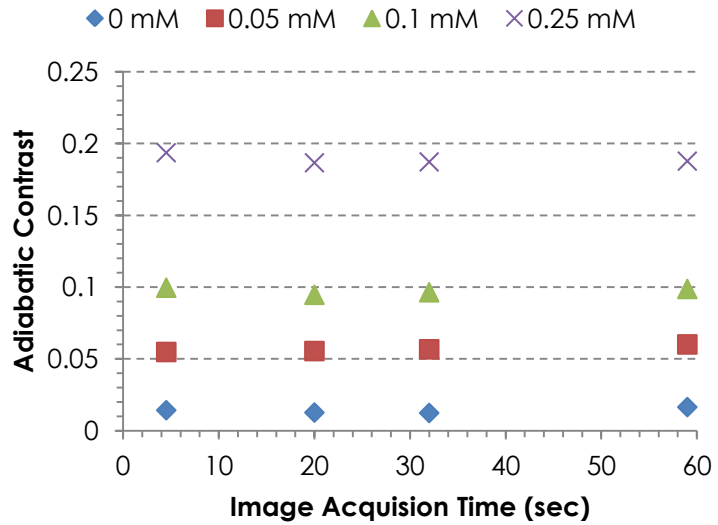
Figure 4.4: AFP contrast highlighting consistency with TSE and HASTE

Finally, an adiabatic pulse prepared gradient echo sequence was designed for imaging at 9.4 Tesla as a proof of concept. For these studies, an adiabatic zero passage

preparation was used to return the magnetization to the +z direction. While there is still one excitation of each repetition time, since this the magnetization is returned to the original orientation the repetition time can be decreased, unlike with the spin-echo method. Figure 4.5 shows that there is indeed a positive correlation of the adiabatic contrast with iron concentration that is especially linear for the longer repetition times of 5 seconds ($R^2 = 0.9979$) and 10 seconds ($R^2 = 0.9991$). However, the relationship is less linear for shorter repetition times such as 500 milliseconds ($R^2 = 0.896$) and 1 second ($R^2 = 0.9509$). While spins that do not fail the adiabatic condition are returned to their original orientation for the next preparation pulse, spins that fail the adiabatic condition require additional time to fully relax. While the contrast with the shorter repetition time is still apparent, iron quantification is compromised as the spin distribution is not identical for the consecutive excitations.
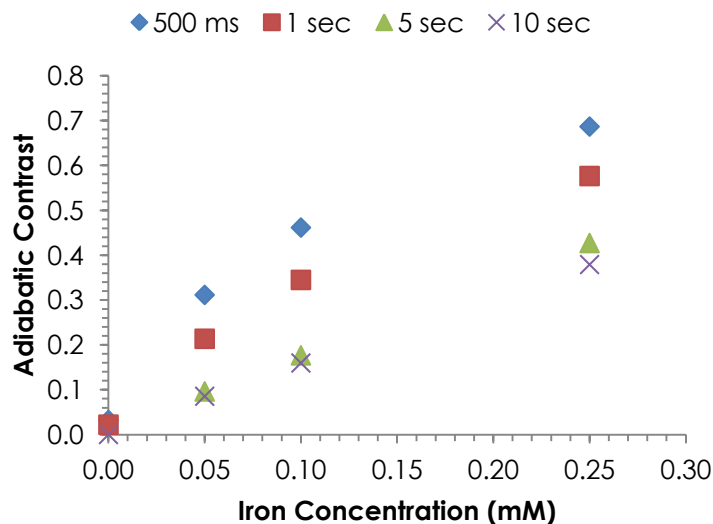
Figure 4.5: Zero passage gradient echo contrast in solution with varying TR at 9.4 Tesla

4.3.2 Quantifying Iron Oxide Nanoparticles *In Vivo*

In vivo molecular imaging presents many practical challenges including the interaction of the dynamic system with the imaging physics. To extend the proposed technique into an animal system, the passively targeted accumulation of iron oxide nanoparticles was used to emphasize the ability of the approach to quantify low concentrations of nanoparticles. Since the liver is a relatively large organ and the iron concentration can be measured *ex vivo* for imaging correlation, these principles were applied to correlate the iron concentration with the image contrast.

Spin echo and adiabatic contrast images were successfully acquired using the TSE accelerated imaging approach. Figure 4.6 shows both that the image quality of the animal images is sufficient to identify the liver in the spin-echo image and that the adiabatic contrast images show increased signal in the liver region. Using identical image scaling, it is apparent that the overall image intensity of the adiabatic contrast image (center panel) is greater than the MT compensated contrast (right panel). This decrease in contrast is especially noticeable in the anterior and posterior muscle, which should not include substantial concentrations of iron or nanoparticle.
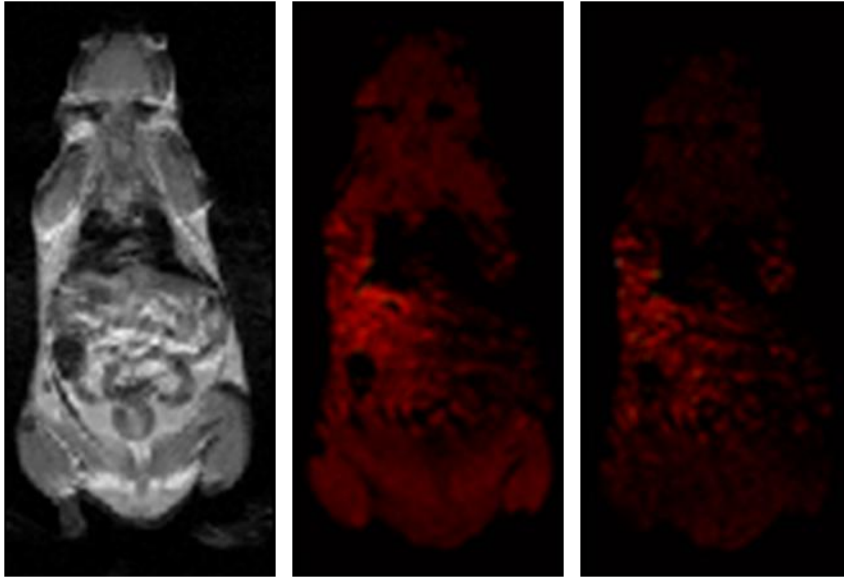
Figure 4.6: Spin-echo, adiabatic contrast and MT compensated animal images

While the visualization of the contrast is encouraging, the true test of the technique is to quantify low iron concentrations. In Figure 4.7 there is a clear linear trend of increasing adiabatic contrast with increasing iron concentration ($R^2 = 0.7366$). Equally noteworthy is that there is a near zero crossing of the adiabatic contrast at a zero normalized iron concentration. Also, even though the measured system and approach are different, the dynamic range of the adiabatic contrast remains consistent with the previous experiments, suggesting a comparison is appropriate.
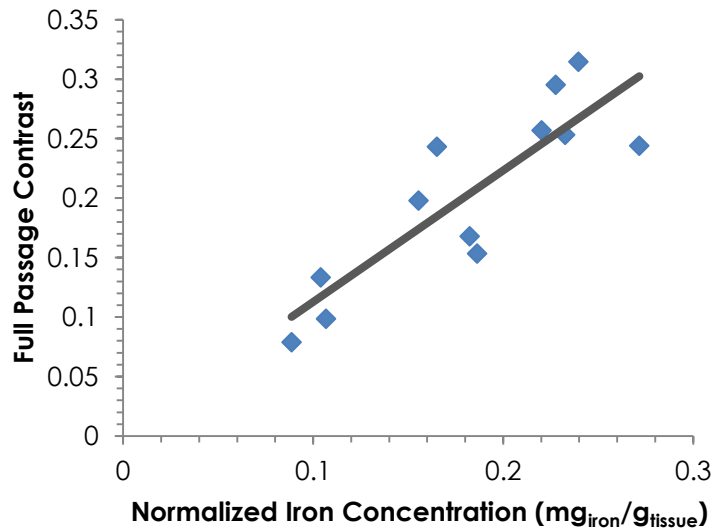
Figure 4.7: Adiabatic contrast is correlated with liver iron concentration

The MT compensated approach is a second approach to contrast quantification that is expected to yield a quantification that is more specific to the iron oxide nanoparticles. Figure 4.7 shows the linear correlation of image contrast with the measured iron concentration that is similar ($R^2 = 0.7398$) to the adiabatic full passage contrast. While the MT compensated approach does not appear to have significant advantages over the full passage method for quantification, the images in Figure 4.6 show the advantage of the MT compensated approach with the increased nanoparticle specificity. It is also notable that while extending the correlation to the zero iron concentration yields a negative contrast measurement, this is similar to the phantom experiments. As in the previous case, this negative contrast measurement is attributed to the fact that the MT effects are not exactly doubled with the contrast.
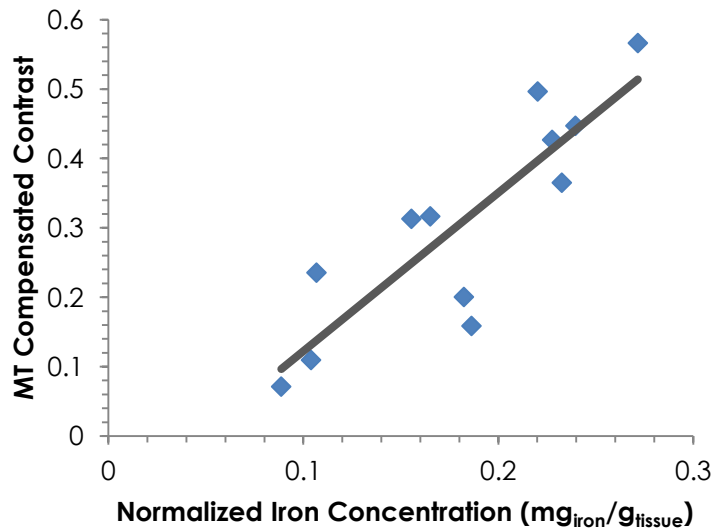
Figure 4.8: MT compensated adiabatic contrast is correlated with liver iron concentration

In an incidental finding, a region of increased adiabatic contrast was observed in one of the animals outside the liver. Using the simultaneously acquired anatomical images, the contrast region was identified as the bladder. This finding was not observed in any of the other subjects, and it was not expected that the nanoparticles would be significantly excreted in the urine within the circulation period. Figure 4.9 shows that while the region of increased intensity appears as a well demarcated area in the animal on the left, the corresponding region in the animal on the right has a lack of signal consistent with non-nanoparticle containing fluid.
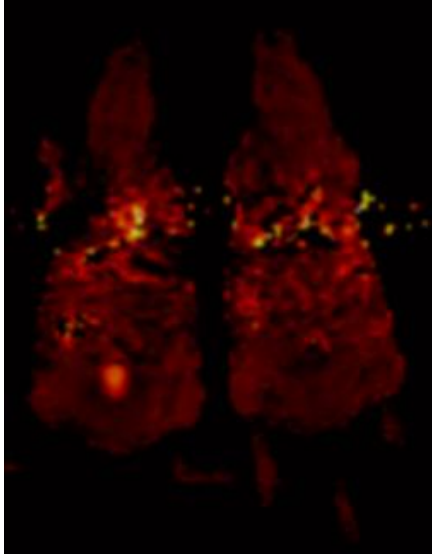
Figure 4.9: Adiabatic contrast image showing bladder hyperintensity

In order to further classify the contrast region, UTE images of the corresponding slice were acquired. Figures 4.10 and 4.11 show that while the right arrow highlights the dark region expected in the normal bladder fluid with a long longitudinal relaxation time, there is a dramatic increase in signal in the bladder of the animal on the left. In fact, using the two echo times it is apparent that there may be an accumulation of nanoparticles in the bladder that is causing a shortening of the longitudinal relaxation time. This effect causes the increased signal intensity on the UTE images. As with the increased adiabatic contrast intensity, the increased signal intensity in the UTE images was only found in this single subject. While the physiological or anatomical explanation of this result is not clear, the results taken together suggests that the iron oxide nanoparticles were filtered through the kidney and into the urinary tract where they accumulated in the bladder. These findings provide further evidence that the adiabatic pulse prepared approach can identify the nanoparticles *in vivo*.

114
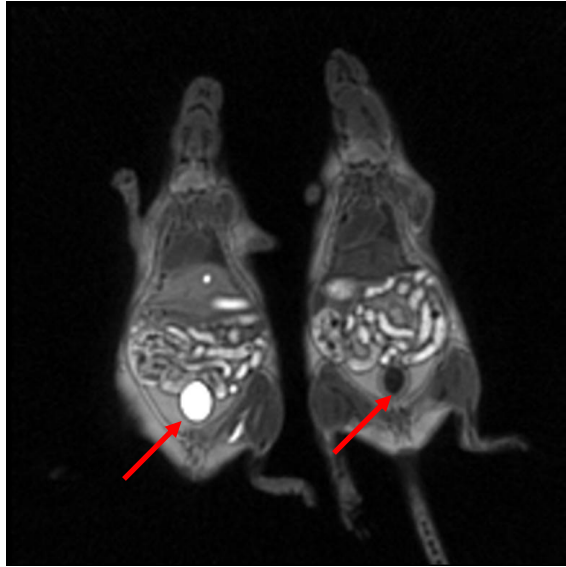
Figure 4.10: UTE with TE = 0.07 msec showing bladder hyperintensity
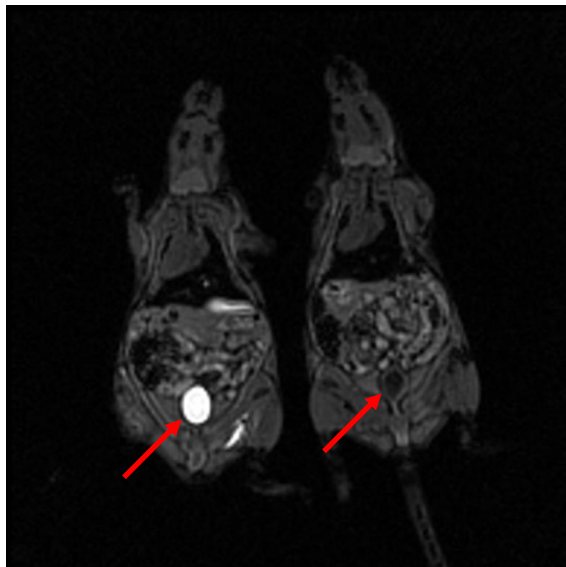
Figure 4.11: UTE with TE = 5.06 msec showing bladder hyperintensity

4.4 Discussion and Conclusion

The adiabatic pulse prepared contrast technique can be translated to *in vivo* imaging and can quantify low iron oxide nanoparticle concentrations. In the first part of this chapter, with knowledge of the contrast mechanism, the adiabatic approach was made compatible with *in vivo* experiments without affecting the nanoparticle quantification. Finally, an experiment was designed to show that *in vivo* nanoparticle concentrations are sufficient for contrast detection and quantification.

While the theoretical basis of the *in vitro* experiments of the previous chapter can be applied to the *in vivo* studies, there are practical challenges that stand as significant obstacles for translating MR imaging techniques to living systems. The most obvious challenge is often that the duration of the imaging sequence must be short enough to be compatible with *in vivo* studies. A primary advantage of the adiabatic approach is that the contrast is achieved during the preparation pulse, which is on the order of milliseconds. In theory, the image acquisition time can be decreased without affecting nanoparticle quantification. Even though the signal to noise ratios of images acquired with a conventional spin-echo and a HASTE sequence may be very different due to the different pulse sequences and different parameters, since the contrast quantification is a normalized difference of similar images the contrast is reproducible Using the TSE and HASTE sequences it was shown that the quantification was very reproducible even as the imaging time was decreased by a factor of nearly 100. The main concern with the accelerated imaging sequences is that sufficient signal is acquired after the preparation

pulse, and as is demonstrated by the extreme example of the HASTE sequence, if the effective echo time is increased too far the quantification is affected.

The successful implementation and results of the adiabatic pulse prepared TSE sequence lead directly to the *in vivo* experiments. While the results showed that the quantification was insensitive to either the TF of the TSE sequence or even the HASTE sequence, for the animal studies the image quality and effective echo time of the sequences was a consideration. Experimentally, it was found that a TF of greater than 4 resulted in a noticeable reduction in anatomical image quality obtained with the current parameters, and since this level of acceleration allowed images to be obtained within a reasonable anesthesia period it was used for the *in vivo* data. In the future, other technical additions such as parallel imaging may be able to further decrease the imaging time while maintaining SNR. It should also be noted that the contrast image quality was not noticeable effected by the macroscopic susceptibility effects of the nanoparticles or the air/tissue interfaces.

The adiabatic full passage and MT compensated sequences show a contrast that is linearly correlated with the *ex vivo* liver iron concentration. These data show the expected linear trend, but there is a greater deviation from the linear correlation than in the phantoms. However, this is not unexpected or necessarily an error in the measurement. The factors that effected the *in vitro* quantification, such as calculating a single contrast measurement for an entire organ, smooth the correlation of the contrast measurement and the nanoparticle concentration. As in the studies quantifying the whole volume iron

concentration based on a single slice, the measured contrast does not necessarily reflect the local concentration. The ability of the technique to localize nanoparticles in a more realistic model of iron oxide nanoparticle delivery will be explored in the final chapter.

The zero crossing of the adiabatic full passage contrast with the normalized iron concentration is also notable. In this measure the iron concentrations of the individual subjects were subtracted from an average mouse liver iron concentration to yield a more specific measure of mouse liver iron oxide nanoparticle concentration. This measure may be especially useful, since strong microscopic magnetic field gradients are a function of the properties of the iron oxide structure. Here, free iron or other iron oxides in the liver have a much smaller effect on the local magnetic field compared to the administered iron oxide nanoparticles that are composed of magnetite and optimized for their effects on the local magnetic field.

Finally, the incidental finding of the increased adiabatic contrast intensity in the bladder of a single subject provides a serendipitous positive control. Taken with the increased signal intensity on the UTE images, these data strongly suggest that iron oxide nanoparticles entered the urinary system and created a high nanoparticle concentration solution in the bladder. The well circumscribed region with high contrast intensity resembles the iron oxide solution phantom results. As previously described, it is not surprising that the localization and quantification of the nanoparticles in tissue is much more challenging compared to phantoms, but these results highlight the potential of using

the adiabatic preparation pulse method for imaging nanoparticles in other animal applications.

In conclusion, with the theoretical foundation provided by the previous chapters an adiabatic pulse prepared approach suitable of *in vivo* imaging was implemented on a clinical MRI scanner. Since the contrast is only a function of the very short preparation pulse period, robust contrast quantification with the acceleration of the imaging sequence is a major advantage for research and clinical translation. As the *in vivo* animal studies show, while the physiological motion of the animals presents challenges for image quality and contrast quantification, the adiabatic pulse prepared approach yields promising results for specifically quantifying iron oxide nanoparticles. This new mechanism for generating quantitative MR contrast from nanoparticles may have many applications as the number and range of molecular imaging studies rapidly expands.

CHAPTER 5

CONCLUSIONS AND FUTURE DIRECTIONS

5.1 Problem Statement

As the number of applications using iron oxide nanoparticles to explore the pathophysiology, diagnosis and treatment of diseases increases, new methods for detecting and quantifying the particles are required. While many methods have been proposed that are sensitive to macroscopic changes in the magnetic field surrounding the nanoparticles, these techniques may also be sensitive to other effects, and therefore the contrast is not specific to the nanoparticles. Also for applications such as quantifying molecular receptor number in a cancer model, quantification is essential. Ideally, an iron oxide nanoparticle contrast should be linearly correlated with iron concentration, reproducible, insensitive to fluctuations in the imaging system, and acquired on a time scale compatible with *in vivo* imaging.

5.2 Conclusions

This work presents a technique for the quantitative molecular imaging of iron oxide nanoparticles using adiabatic preparation pulses. This new contrast mechanism is supported by numerical simulation and experimental results. During the adiabatic

preparation pulse, the adiabatic condition is not fulfilled for spins diffusing through the rapidly changing microscopic magnetic fields surrounding the nanoparticles. The probability of the adiabatic condition failing is directly proportional to the distance between the nanoparticles, which is a function of the nanoparticle concentration. In Chapter 1, it is shown that the adiabatic contrast is linearly correlated with the total iron concentration for several preparations of iron oxide nanoparticles. Additionally, the technique can be implemented on clinical and ultra-high field research MR scanners, the adiabatic mechanism can be extended to produce a zero passage adiabatic contrast and the sequence and pulse parameters and be modified to increase the sensitivity of the measured contrast.

The approach is applied to more realistic molecular environments and cellular imaging in Chapter 2. A technique for magnetization transfer compensation is developed, the effect of diffusion on the contrast is quantified, and the linearity of the contrast for endogenous and exogenous iron oxide contrast agents is presented. Finally, in Chapter 3 accelerated imaging acquisition schemes to acquire adiabatic pulse prepared images in seconds without sacrificing contrast and a passive accumulation model of *in vivo* quantitative iron oxide imaging are demonstrated. This work greatly extends the demonstration of the technique for quantifying iron oxide nanoparticles in solution, since the molecular environment of the particles and their physical interactions is vastly different *in vitro* and *in vivo* compared to in well dispersed solutions. This work shows that not only is the proposed technique capable of quantitative molecular imaging under these conditions, but that modifications to the pulse sequence and the pulse parameters

can optimize the adiabatic approach in each application while maintaining the new contrast mechanism.

5.3 Future Directions

5.3.1 Receptor Targeted Cancer Imaging Using Iron Oxide Nanoparticles

While cell surface receptor targeted nanoparticles are an ideal application for quantitative, *in vivo* molecular MR imaging, these studies face many technical challenges including the transport of the nanoparticles to the site of interest, low particle concentration for imaging, and a continuous distribution of nanoparticles. In order to test the ability of the adiabatic technique to identify and quantify iron oxide particles within this challenging environment, tumors from animals that had received intravenous injection of targeted particles were kindly provided by C. Kessinger and J. Gao at the University of Texas Southwestern Medical Center in Dallas, Texas.

In this model, HT1080 (fibrosarcoma) cells were implanted and formed tumors in the dorsal flank of nude mice. Then cRGD encoded, SPIO-loaded micelles targeting the $\alpha_v\beta_3$ integrin on the tumor cells were injected intravenously through the tail vein and allowed to circulate for 1.5 hours. Following particle circulation, the animals were sacrificed and the tumors were excised, fixed in formalin and suspended in PBS for

imaging. Imaging was performed at 9.4 Tesla as previously described, and the tumor orientation was noted for correlation with Prussian Blue histological staining.

Figure 5.1 shows a region of corresponding decreased signal on T2-weighted imaging, increased adiabatic contrast and positive histological staining for iron. Taken together, these results suggest that the technique may be sensitive enough to detect nanoparticles in molecular MR applications. One notable finding is that the particles did not produce a large contrast region extending beyond the region where the nanoparticles were located, but rather the contrast resembles a continuous distribution of particles within a confined area. It is also important to note that while there is a heterogeneous signal from the surrounding tumor and PBS in the spin-echo image, these varied components are all nulled in the adiabatic contrast image. A technique that is sensitive to the nanoparticles is extremely important as very low concentrations of nanoparticles must be identified within the extremely inhomogeneous tumor molecular environment.

| T2-weighted image | Adiabatic contrast image | Prussian blue staining |
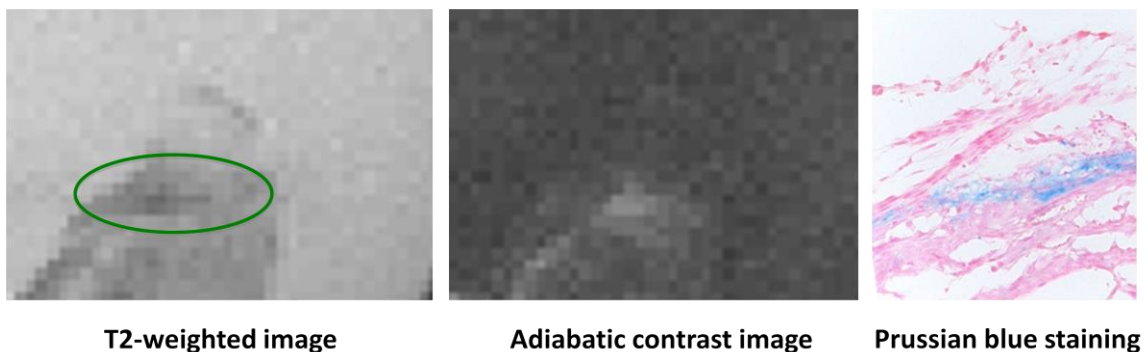
Figure 5.1 Preliminary targeted molecular imaging studies

However, many challenges exist for these applications including registering the MR images with the histological staining and validating the contrast quantification. In fact, a direct injection experiment where iron oxide particles are injected into a tumor or muscle, or where labeled cells are implanted, may be necessary to validate the local, quantitative distribution of nanoparticles. While targeted molecular models are still the ultimate goal, for the purposes of developing the technique it was necessary to reduce the confounding challenges of nanoparticle delivery and accumulation. In this way, the same approaches for optimizing the sensitivity and specificity of the contrast presented in Chapter 2 can be applied to *in vivo* molecular MR imaging.

5.3.2   Adiabatic Pulse Prepared Liver Iron Imaging

Finally, human imaging using the adiabatic pulse prepared technique is not limited to iron oxide nanoparticles being developed as contrast agents. Human iron imaging is of growing interest as iron accumulations and their deleterious effects are being recognized in a number of chronic diseases. MR is an ideal modality for disease surveillance as rich soft tissue information can be acquired over an entire organ, compared to the spatially limited information provided by invasive biopsy. One organ of interest is the liver, where both primary iron diseases, such as haemochromatosis, and non-alcoholic fatty liver disease can change the fat and iron composition of the organ and increase the probably of developing hepatocellular carcinoma.

Liver phantoms with 10% oil and varying iron concentrations were kindly provided by Drs. Nashiely Pineda and Diego Martin. Imaging was performed at 3 Tesla using the adiabatic pulse prepared HASTE sequence for accelerated imaging. The objective of this study was to see if the linear correlation of the adiabatic contrast and iron concentration was maintained in a realistic liver phantom. Figure 5.2 confirms that the linear correlation is preserved with $R^2 = 0.9928$. The liver phantoms presented several additional challenges including an increased number of molecular components in the phantoms, increased size compared to the previously used 1.5 mL phantoms, and since they were imaged simultaneously, a larger overall area for the B_0 and B_1 fields to cover for homogeneous quantification. Taking these facts into account, the technique performed well; however, the notable contrast at a 0 mM iron concentration highlights the need for developing additional methods to reduce magnetization transfer and increase the specificity of the contrast. Here, optimizing the RF pulse may be especially high-yield as the presence of off-resonance components in the liver phantoms that were not included in the previous experiments significantly confounded the quantification.
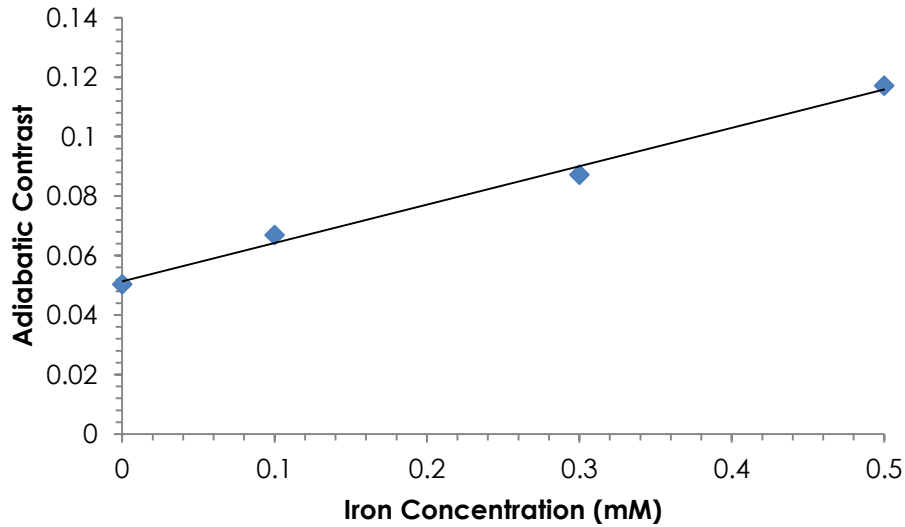
Figure 5.2 Adiabatic contrast in liver phantoms containing 10% oil

Further studies are needed to correlate human contrast measurements with biochemical measurements of iron, such as from longitudinal liver studies of iron content with biopsy or liver transplantation studies where organs undergo extensive MR imaging and histological analysis. However, it appears that the proposed technique can be translated to the clinical setting where adiabatic contrast images can be acquired simultaneously with high quality, T2-weighted images at no additional time cost. While there are several avenues for further optimization, the adiabatic pulse prepared approach appears to be a promising mechanism for quantitative molecular imaging.

REFERENCES

1.   Zeeman P. On the Influence of Magnetixm on the Nature of the Light Emitted by a Substance. Astrophys J. 1897;5:332-47.

2.   Bloch F, Hansen WW, Packard M. The Nuclear Induction Experiment. Phys Rev. 1946;70(7-8):474-85. PubMed PMID: ISI:A1946UB26500004.

3.   Purcell EM, Torrey HC, Pound RV. Resonance Absorption by Nuclear Magnetic Moments in a Solid. Phys Rev. 1946;69(1-2):37-8. PubMed PMID: ISI:A1946UB25600010.

4.   Lauterbur PC. Image Formation by Induced Local Interactions - Examples Employing Nuclear Magnetic-Resonance. Nature. 1973;242(5394):190-1. PubMed PMID: ISI:A1973P031700041.

5.   Mansfield P, Grannell PK. Nmr Diffraction in Solids. J Phys C Solid State. 1973;6(22):L422-L6. PubMed PMID: ISI:A1973R429800007.

6.   Haacke EM. Magnetic resonance imaging : physical principles and sequence design. New York: Wiley; 1999. xxvii, 914 p. p.

7.   Damadian R. Tumor detection by nuclear magnetic resonance. Science. 1971;171(976):1151-3. Epub 1971/03/19. PubMed PMID: 5544870.

8.   Lauffer RB. Targeted Relaxation Enhancement Agents for Mri. Magn Reson Med. 1991;22(2):339-42. PubMed PMID: ISI:A1991GV21100028.

9.   Jacques V, Desreux JF. New classes of MRI contrast agents. Top Curr Chem. 2002;221:123-64. PubMed PMID: ISI:000174162200005.

10.   Aisen AM, Martel W, Braunstein EM, Mcmillin KI, Phillips WA, Kling TF. Mri and Ct Evaluation of Primary Bone and Soft-Tissue Tumors. Am J Roentgenol. 1986;146(4):749-56. PubMed PMID: ISI:A1986A521400017.

11.   Ferrari M. Cancer nanotechnology: opportunities and challenges. Nat Rev Cancer. 2005;5(3):161-71. Epub 2005/03/02. doi: nrc1566 [pii]
10.1038/nrc1566. PubMed PMID: 15738981.

12.   Rogers WJ, Meyer CH, Kramer CM. Technology insight: in vivo cell tracking by use of MRI. Nat Clin Pract Cardiovasc Med. 2006;3(10):554-62. Epub 2006/09/23. doi: ncpcardio0659 [pii]
10.1038/ncpcardio0659. PubMed PMID: 16990841.

13.   Caravan P, Ellison JJ, McMurry TJ, Lauffer RB. Gadolinium(III) Chelates as MRI Contrast Agents: Structure, Dynamics, and Applications. Chem Rev. 1999;99(9):2293-352. Epub 2001/12/26. doi: cr980440x [pii]. PubMed PMID: 11749483.

14.   Gupta AK, Gupta M. Synthesis and surface engineering of iron oxide nanoparticles for biomedical applications. Biomaterials. 2005;26(18):3995-4021. Epub 2005/01/01. doi: S0142-9612(04)00931-7 [pii]
10.1016/j.biomaterials.2004.10.012. PubMed PMID: 15626447.

15.   Zurkiya O, Chan AW, Hu X. MagA is sufficient for producing magnetic nanoparticles in mammalian cells, making it an MRI reporter. Magn Reson Med. 2008;59(6):1225-31. PubMed PMID: 18506784.

16.   Cohen B, Dafni H, Meir G, Harmelin A, Neeman M. Ferritin as an endogenous MRI reporter for noninvasive imaging of gene expression in C6 glioma tumors. Neoplasia. 2005;7(2):109-17. Epub 2005/04/02. doi: 10.1593/neo.04436. PubMed PMID: 15802016.

17.   Genove G, DeMarco U, Xu H, Goins WF, Ahrens ET. A new transgene reporter for in vivo magnetic resonance imaging. Nat Med. 2005;11(4):450-4. Epub 2005/03/22. doi: nm1208 [pii]
10.1038/nm1208. PubMed PMID: 15778721.

18.   Ogawa S, Tank DW, Menon R, Ellermann JM, Kim SG, Merkle H, et al. Intrinsic Signal Changes Accompanying Sensory Stimulation - Functional Brain Mapping with Magnetic-Resonance-Imaging. P Natl Acad Sci USA. 1992;89(13):5951-5. PubMed PMID: ISI:A1992JC86800052.

19.   Kwong KK, Belliveau JW, Chesler DA, Goldberg IE, Weisskoff RM, Poncelet BP, et al. Dynamic Magnetic-Resonance-Imaging of Human Brain Activity during Primary Sensory Stimulation. P Natl Acad Sci USA. 1992;89(12):5675-9. PubMed PMID: ISI:A1992HY05300097.

20.   Sosnovik DE, Weissleder R. Emerging concepts in molecular MRI. Curr Opin Biotechnol. 2007;18(1):4-10. Epub 2006/11/28. doi: S0958-1669(06)00165-0 [pii] 10.1016/j.copbio.2006.11.001. PubMed PMID: 17126545.

21.   Ferrara K, Pollard R, Borden M. Ultrasound microbubble contrast agents: fundamentals and application to gene and drug delivery. Annu Rev Biomed Eng. 2007;9:415-47. Epub 2007/07/27. doi: 10.1146/annurev.bioeng.8.061505.095852. PubMed PMID: 17651012.

22.   Schoepf UJ, Becker CR, Ohnesorge BM, Yucel EK. CT of coronary artery disease. Radiology. 2004;232(1):18-37. Epub 2004/06/29. doi: 10.1148/radiol.2321030636
232/1/18 [pii]. PubMed PMID: 15220491.

23.   Hendrick RE, Haacke EM. Basic Physics of Mr Contrast Agents and Maximization of Image-Contrast. Jmri-J Magn Reson Im. 1993;3(1):137-48. PubMed PMID: ISI:A1993KJ72500022.

24.   Carr DH, Brown J, Bydder GM, Weinmann HJ, Speck U, Thomas DJ, et al. Intravenous chelated gadolinium as a contrast agent in NMR imaging of cerebral tumours. Lancet. 1984;1(8375):484-6. Epub 1984/03/03. PubMed PMID: 6142210.

25.   Kim RJ, Fieno DS, Parrish TB, Harris K, Chen EL, Simonetti O, et al. Relationship of MRI delayed contrast enhancement to irreversible injury, infarct age, and contractile function. Circulation. 1999;100(19):1992-2002. Epub 1999/11/11. PubMed PMID: 10556226.

26.   Prince MR. Gadolinium-enhanced MR aortography. Radiology. 1994;191(1):155-64. Epub 1994/04/01. PubMed PMID: 8134563.

27.   Krinsky GA, Lee VS, Theise ND, Weinreb JC, Rofsky NM, Diflo T, et al. Hepatocellular carcinoma and dysplastic nodules in patients with cirrhosis: prospective diagnosis with MR imaging and explantation correlation. Radiology. 2001;219(2):445-54. Epub 2001/04/27. PubMed PMID: 11323471.

28.   Kuo PH, Kanal E, Abu-Alfa AK, Cowper SE. Gadolinium-based MR contrast agents and nephrogenic systemic fibrosis. Radiology. 2007;242(3):647-9. Epub 2007/01/11. doi: 2423061640 [pii]
10.1148/radiol.2423061640. PubMed PMID: 17213364.

29.   Martin DR, Krishnamoorthy SK, Kalb B, Salman KN, Sharma P, Carew JD, et al. Decreased Incidence of NSF in Patients on Dialysis After Changing Gadolinium Contrast-Enhanced MRI Protocols. Journal of Magnetic Resonance Imaging. 2010;31(2):440-6. doi: Doi 10.1002/Jmri.22024. PubMed PMID: ISI:000274117200021.

30.   Kraitchman DL, Bulte JW. Imaging of stem cells using MRI. Basic Res Cardiol. 2008;103(2):105-13. Epub 2008/03/08. doi: 10.1007/s00395-008-0704-5. PubMed PMID: 18324366.

31.   Caravan P. Protein-targeted gadolinium-based magnetic resonance imaging (MRI) contrast agents: design and mechanism of action. Acc Chem Res. 2009;42(7):851-62. Epub 2009/02/19. doi: 10.1021/ar800220p
10.1021/ar800220p [pii]. PubMed PMID: 19222207.

32.   Weissleder R, Bogdanov A, Neuwelt EA, Papisov M. Long-Circulating Iron-Oxides for Mr-Imaging. Adv Drug Deliver Rev. 1995;16(2-3):321-34. PubMed PMID: ISI:A1995TD17100014.

33.   Weissleder R, Stark DD, Engelstad BL, Bacon BR, Compton CC, White DL, et al. Superparamagnetic iron oxide: pharmacokinetics and toxicity. AJR Am J Roentgenol. 1989;152(1):167-73. Epub 1989/01/01. PubMed PMID: 2783272.

34.   Anzai Y, Piccoli CW, Outwater EK, Stanford W, Bluemke DA, Nurenberg P, et al. Evaluation of neck and body metastases to nodes with ferumoxtran 10-enhanced MR imaging: Phase III safety and efficacy study. Radiology. 2003;228(3):777-88. doi: DOI 10.1148/radiol.2283020892. PubMed PMID: ISI:000184966400027.

35.   Schultz JF, Bell JD, Goldstein RM, Kuhn JA, McCarty TM. Hepatic tumor imaging using iron oxide MRI: comparison with computed tomography, clinical impact, and cost analysis. Ann Surg Oncol. 1999;6(7):691-8. Epub 1999/11/24. PubMed PMID: 10560856.

36.   Reimer P, Jahnke N, Fiebich M, Schima W, Deckers F, Marx C, et al. Hepatic lesion detection and characterization: Value of nonenhanced MR imaging, superparamagnetic iron oxide-enhanced MR imaging, and spiral CT-ROC analysis. Radiology. 2000;217(1):152-8. PubMed PMID: ISI:000089452500024.

37.   Lind K, Kresse M, Debus NP, Muller RH. A novel formulation for superparamagnetic iron oxide (SPIO) particles enhancing MR lymphography: Comparison of physicochemical properties and the in vivo behaviour. J Drug Target. 2002;10(3):221-30. doi: Doi 10.1080/10611860290022651. PubMed PMID: ISI:000175689100006.

38.   Mack MG, Balzer JO, Straub R, Eichler K, Vogl TJ. Superparamagnetic iron oxide - Enhanced MR imaging of head and neck lymph nodes. Radiology. 2002;222(1):239-44. PubMed PMID: ISI:000172884800036.

39.   Zimmer C, Weissleder R, Poss K, Bogdanova A, Wright SC, Enochs WS. Mr-Imaging of Phagocytosis in Experimental Gliomas. Radiology. 1995;197(2):533-8. PubMed PMID: ISI:A1995TB33600038.

40.   Laurent S, Forge D, Port M, Roch A, Robic C, Elst LV, et al. Magnetic iron oxide nanoparticles: Synthesis, stabilization, vectorization, physicochemical characterizations, and biological applications. Chem Rev. 2008;108(6):2064-110. doi: Doi 10.1021/Cr068445e. PubMed PMID: ISI:000256738100009.

41.   Girard OM, Du J, Agemy L, Sugahara KN, Kotamraju VR, Ruoslahti E, et al. Optimization of Iron Oxide Nanoparticle Detection Using Ultrashort Echo Time Pulse Sequences: Comparison of $T(1)$, $T*(2)$, and Synergistic $T(1)$-$T*(2)$ Contrast Mechanisms. Magn Reson Med. 2011;65(6):1649-60. doi: Doi 10.1002/Mrm.22755. PubMed PMID: ISI:000291115500015.

42.   Ward J, Chen F, Guthrie JA, Wilson D, Lodge JPA, Wyatt JI, et al. Hepatic lesion detection after superparamagnetic iron oxide enhancement: Comparison of five T2-weighted sequences at 1.0 T by using alternative-free response receiver operating characteristic analysis. Radiology. 2000;214(1):159-66. PubMed PMID: ISI:000084414400026.

43.   Thorek DLJ, Chen A, Czupryna J, Tsourkas A. Superparamagnetic iron oxide nanoparticle probes for molecular imaging. Ann Biomed Eng. 2006;34(1):23-38. doi: DOI 10.1007/s10439-005-9002-7. PubMed PMID: ISI:000236354800004.

44.   Xie J, Huang J, Li X, Sun S, Chen X. Iron Oxide Nanoparticle Platform for Biomedical Applications. Curr Med Chem. 2009;16(10):1278-94. PubMed PMID: ISI:000265692100008.

45.   Lutz JF, Stiller S, Hoth A, Kaufner L, Pison U, Cartier R. One-pot synthesis of PEGylated ultrasmall iron-oxide nanoparticles and their in vivo evaluation as magnetic

resonance imaging contrast agents. Biomacromolecules. 2006;7(11):3132-8. doi: Doi 10.1021/Bm0607527. PubMed PMID: ISI:000241941600029.

46.   Massart R, Dubois E, Cabuil V, Hasmonay E. Preparation and Properties of Monodisperse Magnetic Fluids. J Magn Magn Mater. 1995;149(1-2):1-5. PubMed PMID: ISI:A1995RR75100002.

47.   Wang YXJ, Hussain SM, Krestin GP. Superparamagnetic iron oxide contrast agents: physicochemical characteristics and applications in MR imaging. Eur Radiol. 2001;11(11):2319-31. PubMed PMID: ISI:000172277300030.

48.   Gupta AK, Wells S. Surface-modified superparamagnetic nanoparticles for drug delivery: Preparation, characterization, and cytotoxicity studies. Ieee T Nanobiosci. 2004;3(1):66-73.   doi: Doi   10.1109/Tnb.2003.820277.   PubMed   PMID: ISI:000220589500013.

49.   Choi HS, Liu W, Misra P, Tanaka E, Zimmer JP, Ipe BI, et al. Renal clearance of quantum dots. Nat Biotechnol. 2007;25(10):1165-70. doi: Doi 10.1038/Nbt1340. PubMed PMID: ISI:000250226600028.

50.   Neuberger T, Schopf B, Hofmann H, Hofmann M, von Rechenberg B. Superparamagnetic nanoparticles for biomedical applications: Possibilities and limitations of a new drug delivery system. J Magn Magn Mater. 2005;293(1):483-96. doi: DOI 10.1016/j.jmmm.2005.01.064. PubMed PMID: ISI:000229661400074.

51.   Xu CJ, Sun SH. Monodisperse magnetic nanoparticles for biomedical applications. Polym Int. 2007;56(7):821-6. doi: Doi 10.1002/Pi.2251. PubMed PMID: ISI:000247218700001.

52.   Jung CW. Surface-Properties of Superparamagnetic Iron-Oxide Mr Contrast Agents - Ferumoxides, Ferumoxtran, Ferumoxsil. Magn Reson Imaging. 1995;13(5):675-91. PubMed PMID: ISI:A1995RR82800003.

53.   Jung CW, Jacobs P. Physical and Chemical-Properties of Superparamagnetic Iron-Oxide Mr Contrast Agents - Ferumoxides, Ferumoxtran, Ferumoxsil. Magn Reson Imaging. 1995;13(5):661-74. PubMed PMID: ISI:A1995RR82800002.

54.   Molday RS, Mackenzie D. Immunospecific Ferromagnetic Iron-Dextran Reagents for the Labeling and Magnetic Separation of Cells. J Immunol Methods. 1982;52(3):353-67. PubMed PMID: ISI:A1982PB88200007.

55.   Moore A, Marecos E, Bogdanov A, Weissleder R. Tumoral distribution of long-circulating dextran-coated iron oxide nanoparticles in a rodent model. Radiology. 2000;214(2):568-74. PubMed PMID: ISI:000085023400039.

56.   Matuszewski L, Persigehl T, Wall A, Schwindt W, Tombach B, Fobker M, et al. Cell tagging with clinically approved iron oxides: Feasibility and effect of lipofection, particle size, and surface coating on labeling efficiency. Radiology. 2005;235(1):155-61. doi: DOI 10.1148/radiol.2351040094. PubMed PMID: ISI:000227952600024.

57.   Tong S, Hou SJ, Zheng ZL, Zhou J, Bao G. Coating Optimization of Superparamagnetic Iron Oxide Nanoparticles for High T(2) Relaxivity. Nano Lett. 2010;10(11):4607-13.   doi: Doi   10.1021/Nl102623x.   PubMed   PMID: ISI:000283907600053.

58.   LaConte LEW, Nitin N, Zurkiya O, Caruntu D, O'Connor CJ, Hu XP, et al. Coating thickness of magnetic iron oxide nanoparticles affects R-2 relaxivity. Journal of Magnetic Resonance Imaging. 2007;26(6):1634-41. doi: Doi 10.1002/Jmri.21194. PubMed PMID: ISI:000252012100033.

59.   Schenck JF. The role of magnetic susceptibility in magnetic resonance imaging: MRI magnetic compatibility of the first and second kinds. Med Phys. 1996;23(6):815-50. Epub 1996/06/01. PubMed PMID: 8798169.

60.   Garwood M, DelaBarre L. The return of the frequency sweep: designing adiabatic pulses for contemporary NMR. J Magn Reson. 2001;153(2):155-77. Epub 2001/12/13. doi: 10.1006/jmre.2001.2340
S1090-7807(01)92340-7 [pii]. PubMed PMID: 11740891.

61.   Bloch F, Hansen WW, Packard M. Nuclear Induction. Phys Rev. 1946;69(11-1):680-. PubMed PMID: ISI:A1946UB26100046.

62.   Garwood M, Nease B, Ke Y, Degraaf RA, Merkle H. Simultaneous Compensation for B-1 Inhomogeneity and Resonance Offsets by a Multiple-Quantum Nmr Sequence Using Adiabatic Pulses. J Magn Reson Ser A. 1995;112(2):272-4. PubMed PMID: ISI:A1995QG80600023.

63.   vanZijl PCM, Hwang TL, Johnson MO, Garwood M. Optimized excitation and automation for high-resolution NMR using B-1-insensitive rotation pulses. J Am Chem Soc. 1996;118(23):5510-1. PubMed PMID: ISI:A1996UQ51700037.

64.   Silver MS, Joseph RI, Hoult DI. Highly Selective Pi/2 and Pi-Pulse Generation. Journal of Magnetic Resonance. 1984;59(2):347-51. PubMed PMID: ISI:A1984TJ85100018.

65.   DeGraaf RA, Nicolay K. Adiabatic rf pulses: Applications to in vivo NMR. Concepts in Magnetic Resonance. 1997;9(4):247-68. PubMed PMID: ISI:A1997XG35900004.

66.   Ugurbil K, Garwood M, Rath AR. Optimization of Modulation Functions to Improve Insensitivity of Adiabatic Pulses to Variations in B1 Magnitude. Journal of Magnetic Resonance. 1988;80(3):448-69. PubMed PMID: ISI:A1988R844000005.

67.   Skinner TE, Robitaille PML. Adiabatic Excitation Using Sin(2) Amplitude and Cos(2) Frequency-Modulation Functions. J Magn Reson Ser A. 1993;103(1):34-9. PubMed PMID: ISI:A1993LJ62500006.

68.   Kupce E, Freeman R. Optimized adiabatic pulses for wideband spin inversion. J Magn Reson Ser A. 1996;118(2):299-303. PubMed PMID: ISI:A1996TZ08200020.

69.   Rosenfeld D, Panfil SL, Zur Y. Design of adiabatic pulses for fat-suppression using analytic solutions of the Bloch equation. Magn Reson Med. 1997;37(5):793-801. PubMed PMID: ISI:A1997WV93600021.

70.   Bendall MR, Pegg DT. Uniform Sample Excitation with Surface Coils for Invivo Spectroscopy by Adiabatic Rapid Half Passage. Journal of Magnetic Resonance. 1986;67(2):376-81. PubMed PMID: ISI:A1986C013200022.

71.   Tannus A, Garwood M. Adiabatic pulses. NMR Biomed. 1997;10(8):423-34. Epub 1998/05/23. doi: 10.1002/(SICI)1099-1492(199712)10:8<423::AID-NBM488>3.0.CO;2-X [pii]. PubMed PMID: 9542739.

72.   Garwood M, Ugurbil K, Rath AR, Bendall MR, Ross BD, Mitchell SL, et al. Magnetic resonance imaging with adiabatic pulses using a single surface coil for RF transmission and signal detection. Magn Reson Med. 1989;9(1):25-34. Epub 1989/01/01. PubMed PMID: 2709994.

73.   Staewen RS, Johnson AJ, Ross BD, Parrish T, Merkle H, Garwood M. 3-D FLASH imaging using a single surface coil and a new adiabatic pulse, BIR-4. Invest Radiol. 1990;25(5):559-67. Epub 1990/05/01. PubMed PMID: 2345088.

74.   Garwood M, Ke Y. Symmetrical Pulses to Induce Arbitrary Flip Angles with Compensation for Rf Inhomogeneity and Resonance Offsets. Journal of Magnetic Resonance. 1991;94(3):511-25. PubMed PMID: ISI:A1991GH88100007.

75.   Kinchesh P, Ordidge RJ. Spin-echo MRS in humans at high field: LASER localisation using FOCI pulses. J Magn Reson. 2005;175(1):30-43. Epub 2005/06/14. doi: S1090-7807(05)00095-9 [pii]
10.1016/j.jmr.2005.03.009. PubMed PMID: 15949746.

76.   de Graaf RA, Nicolay K, Garwood M. Single-shot, B1-insensitive slice selection with a gradient-modulated adiabatic pulse, BISS-8. Magn Reson Med. 1996;35(5):652-7. Epub 1996/05/01. PubMed PMID: 8722815.

77.   Dai WY, Garcia D, de Bazelaire C, Alsop DC. Continuous Flow-Driven Inversion for Arterial Spin Labeling Using Pulsed Radio Frequency and Gradient Fields. Magn Reson Med. 2008;60(6):1488-97. doi: Doi 10.1002/Mrm.21790. PubMed PMID: ISI:000261225100024.

78.   Detre JA, Zhang WG, Roberts DA, Silva AC, Williams DS, Grandis DJ, et al. Tissue-Specific Perfusion Imaging Using Arterial Spin-Labeling. Nmr in Biomedicine. 1994;7(1-2):75-82. PubMed PMID: ISI:A1994NL28000011.

79.   Seppenwoolde JH, Viergever MA, Bakker CJ. Passive tracking exploiting local signal conservation: the white marker phenomenon. Magn Reson Med. 2003;50(4):784-90. Epub 2003/10/03. doi: 10.1002/mrm.10574. PubMed PMID: 14523965.

80.   Seppenwoolde JH, Vincken KL, Bakker CJG. White-marker imaging - Separating magnetic susceptibility effects from partial volume effects. Magn Reson Med. 2007;58(3):605-9. doi: Doi 10.1002/Mrm.21304. PubMed PMID: ISI:000249260200021.

81.   Cunningham CH, Arai T, Yang PC, McConnell MV, Pauly JM, Conolly SM. Positive contrast magnetic resonance imaging of cells labeled with magnetic nanoparticles. Magn Reson Med. 2005;53(5):999-1005. Epub 2005/04/22. doi: 10.1002/mrm.20477. PubMed PMID: 15844142.

82.   Balchandani P, Yamada M, Pauly J, Yang P, Spielman D. Self-Refocused Spatial-Spectral Pulse for Positive Contrast Imaging of Cells Labeled with SPIO Nanoparticles. Magn Reson Med. 2009;62(1):183-92. doi: Doi 10.1002/Mrm.21973. PubMed PMID: ISI:000267404300020.

83.   Liu T, Spincemaille P, de Rochefort L, Kressler B, Wang Y. Calculation of susceptibility through multiple orientation sampling (COSMOS): a method for conditioning the inverse problem from measured magnetic field map to susceptibility source image in MRI. Magn Reson Med. 2009;61(1):196-204. Epub 2008/12/20. doi: 10.1002/mrm.21828. PubMed PMID: 19097205.

84.   Dahnke H, Liu W, Herzka D, Frank JA, Schaeffter T. Susceptibility gradient mapping (SGM): A new postprocessing method for positive contrast generation applied to superparamagnetic iron oxide particle (SPIO)-labeled cells. Magn Reson Med. 2008;60(3):595-603.   doi: Doi   10.1002/Mrm.21478.   PubMed   PMID: ISI:000259053900013.

85.   Langley J, Zhao Q. Quantification of SPIO Nanoparticles using Phase Gradient Mapping. Embc: 2009 Annual International Conference of the Ieee Engineering in Medicine   and   Biology   Society,   Vols   1-20.   2009:3605-8.   PubMed   PMID: ISI:000280543602267.

86.   Zhao Q, Langley J, Lee S, Liu W. Positive contrast technique for the detection and quantification of superparamagnetic iron oxide nanoparticles in MRI. Nmr in Biomedicine.   2011;24(5):464-72.   doi: Doi   10.1002/Nbm.1608.   PubMed   PMID: ISI:000291597200004.

87.   Langley J, Liu W, Jordan EK, Frank JA, Zhao Q. Quantification of SPIO Nanoparticles in vivo Using the Finite Perturber Method. Magn Reson Med. 2011;65(5):1461-9.   doi: Doi   10.1002/Mrm.22727.   PubMed   PMID: ISI:000289760800032.

88.   Stuber M, Gilson WD, Schar M, Kedziorek DA, Hofmann LV, Shah S, et al. Positive contrast visualization of iron oxide-labeled stem cells using inversion-recovery with ON-resonant water suppression (IRON). Magn Reson Med. 2007;58(5):1072-7. Epub 2007/10/31. doi: 10.1002/mrm.21399. PubMed PMID: 17969120.

89.   Korosoglou G, Tang L, Kedziorek D, Cosby K, Gilson WD, Vonken EJ, et al. Positive contrast MR-lymphography using inversion recovery with ON-resonant water suppression (IRON). J Magn Reson Imaging. 2008;27(5):1175-80. Epub 2008/04/22. doi: 10.1002/jmri.21337. PubMed PMID: 18425827.

90.   Suzuki Y, Cunningham CH, Noguchi K, Chen IY, Weissman IL, Yeung AC, et al. In vivo serial evaluation of superparamagnetic iron-oxide labeled stem cells by off-resonance positive contrast. Magn Reson Med. 2008;60(6):1269-75. Epub 2008/11/26.

doi: 10.1002/mrm.21816. PubMed PMID: 19030159; PubMed Central PMCID: PMC2597338.

91.   Zurkiya O, Hu X. Off-resonance saturation as a means of generating contrast with superparamagnetic nanoparticles. Magn Reson Med. 2006;56(4):726-32. Epub 2006/08/31. doi: 10.1002/mrm.21024. PubMed PMID: 16941618.

92.   Khemtong C, Kessinger CW, Ren J, Bey EA, Yang SG, Guthi JS, et al. In vivo off-resonance saturation magnetic resonance imaging of alphavbeta3-targeted superparamagnetic nanoparticles. Cancer Res. 2009;69(4):1651-8. Epub 2009/02/05. doi: 0008-5472.CAN-08-3231 [pii]
10.1158/0008-5472.CAN-08-3231. PubMed PMID: 19190328.

93.   Lebel RM, Menon RS, Bowen CV. Relaxometry model of strong dipolar perturbers for balanced-SSFP: Application to quantification of SPIO loaded cells. Magn Reson Med. 2006;55(3):583-91. doi: Doi 10.1002/Mrm.20799. PubMed PMID: ISI:000235858400016.

94.   Cukur T, Yamada M, Overall WR, Yang P, Nishimura DG. Positive Contrast with Alternating Repetition Time SSFP (PARTS): A Fast Imaging Technique for SPIO-Labeled Cells. Magn Reson Med. 2010;63(2):427-37. doi: Doi 10.1002/Mrm.22241. PubMed PMID: ISI:000273995200019.

95.   Conolly S, Nishimura D, Macovski A. Sweep-Diagram Analysis of Selective Adiabatic Pulses. Journal of Magnetic Resonance. 1989;83(3):549-64. PubMed PMID: ISI:A1989AD08800008.

96.   Nitin N, LaConte LEW, Zurkiya O, Hu X, Bao G. Functionalization and peptide-based delivery of magnetic nanoparticles as an intracellular MRI contrast agent. J Biol Inorg Chem. 2004;9(6):706-12. doi: DOI 10.1007/s00775-004-0560-1. PubMed PMID: ISI:000223956600008.

97.   Weissleder R, Mahmood U. Molecular imaging. Radiology. 2001;219(2):316-33. Epub 2001/04/27. PubMed PMID: 11323453.

98.   Guzman R, Uchida N, Bliss TM, He D, Christopherson KK, Stellwagen D, et al. Long-term monitoring of transplanted human neural stem cells in developmental and pathological contexts with MRI. Proc Natl Acad Sci U S A. 2007;104(24):10211-6. Epub 2007/06/08. doi: 10.1073/pnas.0608519104. PubMed PMID: 17553967; PubMed Central PMCID: PMC1891235.

99.   Amsalem Y, Mardor Y, Feinberg MS, Landa N, Miller L, Daniels D, et al. Iron-oxide labeling and outcome of transplanted mesenchymal stem cells in the infarcted myocardium. Circulation. 2007;116(11 Suppl):I38-45. Epub 2007/09/14. doi: 10.1161/CIRCULATIONAHA.106.680231. PubMed PMID: 17846324.

100.   Frank JA, Miller BR, Arbab AS, Zywicke HA, Jordan EK, Lewis BK, et al. Clinically applicable labeling of mammalian and stem cells by combining superparamagnetic iron oxides and transfection agents. Radiology. 2003;228(2):480-7. Epub 2003/06/24. doi: 10.1148/radiol.2281020638. PubMed PMID: 12819345.

101.   Morawski AM, Winter PM, Crowder KC, Caruthers SD, Fuhrhop RW, Scott MJ, et al. Targeted nanoparticles for quantitative imaging of sparse molecular epitopes with MRI. Magn Reson Med. 2004;51(3):480-6. Epub 2004/03/09. doi: 10.1002/mrm.20010. PubMed PMID: 15004788.

102.   Padhani AR. Dynamic contrast-enhanced MRI in clinical oncology: current status and future directions. J Magn Reson Imaging. 2002;16(4):407-22. Epub 2002/09/28. doi: 10.1002/jmri.10176. PubMed PMID: 12353256.

103.   Williams JB, Ye Q, Hitchens TK, Kaufman CL, Ho C. MRI detection of macrophages labeled using micrometer-sized iron oxide particles. J Magn Reson Imaging. 2007;25(6):1210-8. Epub 2007/05/24. doi: 10.1002/jmri.20930. PubMed PMID: 17520727.

104.   Bulte JW, Hoekstra Y, Kamman RL, Magin RL, Webb AG, Briggs RW, et al. Specific MR imaging of human lymphocytes by monoclonal antibody-guided dextran-magnetite particles. Magn Reson Med. 1992;25(1):148-57. Epub 1992/05/01. PubMed PMID: 1375703.

105.   Walczak P, Ruiz-Cabello J, Kedziorek DA, Gilad AA, Lin S, Barnett B, et al. Magnetoelectroporation: improved labeling of neural stem cells and leukocytes for cellular magnetic resonance imaging using a single FDA-approved agent. Nanomedicine : nanotechnology, biology, and medicine. 2006;2(2):89-94. Epub 2007/02/13. doi: 10.1016/j.nano.2006.01.003. PubMed PMID: 17292120.

106.   Qiu B, Xie D, Walczak P, Li X, Ruiz-Cabello J, Minoshima S, et al. Magnetosonoporation: instant magnetic labeling of stem cells. Magn Reson Med. 2010;63(6):1437-41. Epub 2010/06/01. doi: 10.1002/mrm.22348. PubMed PMID: 20512844.

107.   Bulte JW, Kraitchman DL. Iron oxide MR contrast agents for molecular and cellular imaging. NMR Biomed. 2004;17(7):484-99. Epub 2004/11/05. doi: 10.1002/nbm.924. PubMed PMID: 15526347.

108.   de Vries IJ, Lesterhuis WJ, Barentsz JO, Verdijk P, van Krieken JH, Boerman OC, et al. Magnetic resonance tracking of dendritic cells in melanoma patients for monitoring of cellular therapy. Nat Biotechnol. 2005;23(11):1407-13. Epub 2005/11/01. doi: 10.1038/nbt1154. PubMed PMID: 16258544.

109.   Zhang Z, van den Bos EJ, Wielopolski PA, de Jong-Popijus M, Bernsen MR, Duncker DJ, et al. In vitro imaging of single living human umbilical vein endothelial cells with a clinical 3.0-T MRI scanner. Magma. 2005;18(4):175-85. Epub 2005/08/13. doi: 10.1007/s10334-005-0108-6. PubMed PMID: 16096808.

110.   Kostura L, Kraitchman DL, Mackay AM, Pittenger MF, Bulte JW. Feridex labeling of mesenchymal stem cells inhibits chondrogenesis but not adipogenesis or osteogenesis. NMR Biomed. 2004;17(7):513-7. Epub 2004/11/05. doi: 10.1002/nbm.925. PubMed PMID: 15526348.

111.   Schafer R, Kehlbach R, Muller M, Bantleon R, Kluba T, Ayturan M, et al. Labeling of human mesenchymal stromal cells with superparamagnetic iron oxide leads to a decrease in migration capacity and colony formation ability. Cytotherapy. 2009;11(1):68-78. Epub 2009/02/05. doi: 10.1080/14653240802666043. PubMed PMID: 19191056.

112.   Briley-Saebo K, Hustvedt SO, Haldorsen A, Bjornerud A. Long-term imaging effects in rat liver after a single injection of an iron oxide nanoparticle based MR contrast agent. J Magn Reson Imaging. 2004;20(4):622-31. Epub 2004/09/25. doi: 10.1002/jmri.20175. PubMed PMID: 15390223.

113.   Henkelman RM, Stanisz GJ, Graham SJ. Magnetization transfer in MRI: a review. NMR Biomed. 2001;14(2):57-64. Epub 2001/04/26. doi: 10.1002/nbm.683 [pii]. PubMed PMID: 11320533.

114.   Sartorio R, Vergara A, Paduano L, Vitagliano V. Mutual diffusion in aqueous solution of poly(ethyleneglycol) samples. Some comments on the effect of chain length and polydispersity. Phys Chem Chem Phys. 1999;1(23):5377-83. PubMed PMID: ISI:000083918200016.

115.   Wolff SD, Balaban RS. Magnetization transfer contrast (MTC) and tissue water proton relaxation in vivo. Magn Reson Med. 1989;10(1):135-44. Epub 1989/04/01. PubMed PMID: 2547135.

116.   Chertok B, Moffat BA, David AE, Yu F, Bergemann C, Ross BD, et al. Iron oxide nanoparticles as a drug delivery vehicle for MRI monitored magnetic targeting of brain tumors. Biomaterials. 2008;29(4):487-96. Epub 2007/10/30. doi: 10.1016/j.biomaterials.2007.08.050. PubMed PMID: 17964647; PubMed Central PMCID: PMC2761681.

117.   Peng XH, Qian X, Mao H, Wang AY, Chen ZG, Nie S, et al. Targeted magnetic iron oxide nanoparticles for tumor imaging and therapy. International journal of nanomedicine. 2008;3(3):311-21. Epub 2008/11/11. PubMed PMID: 18990940; PubMed Central PMCID: PMC2626938.

118.   Kelly KA, Allport JR, Tsourkas A, Shinde-Patil VR, Josephson L, Weissleder R. Detection of vascular adhesion molecule-1 expression using a novel multimodal nanoparticle. Circulation research. 2005;96(3):327-36. Epub 2005/01/18. doi: 10.1161/01.RES.0000155722.17881.dd. PubMed PMID: 15653572.

119.   Stark DD, Weissleder R, Elizondo G, Hahn PF, Saini S, Todd LE, et al. Superparamagnetic iron oxide: clinical application as a contrast agent for MR imaging of the liver. Radiology. 1988;168(2):297-301. Epub 1988/08/01. PubMed PMID: 3393649.

120.   Reimer P, Jahnke N, Fiebich M, Schima W, Deckers F, Marx C, et al. Hepatic lesion detection and characterization: value of nonenhanced MR imaging, superparamagnetic iron oxide-enhanced MR imaging, and spiral CT-ROC analysis. Radiology. 2000;217(1):152-8. Epub 2000/09/30. PubMed PMID: 11012438.

121.   Runge VM. Safety of approved MR contrast media for intravenous injection. J Magn Reson Imaging. 2000;12(2):205-13. Epub 2000/08/10. PubMed PMID: 10931582.

122.   Dousset V, Delalande C, Ballarino L, Quesson B, Seilhan D, Coussemacq M, et al. In vivo macrophage activity imaging in the central nervous system detected by magnetic resonance. Magn Reson Med. 1999;41(2):329-33. Epub 1999/03/18. PubMed PMID: 10080281.

123.   Ruehm SG, Corot C, Vogt P, Kolb S, Debatin JF. Magnetic resonance imaging of atherosclerotic plaque with ultrasmall superparamagnetic particles of iron oxide in hyperlipidemic rabbits. Circulation. 2001;103(3):415-22. Epub 2001/02/07. PubMed PMID: 11157694.

124.	Zimmer C, Weissleder R, Poss K, Bogdanova A, Wright SC, Jr., Enochs WS. MR imaging of phagocytosis in experimental gliomas. Radiology. 1995;197(2):533-8. Epub 1995/11/01. PubMed PMID: 7480707.

125.	Harisinghani MG, Barentsz J, Hahn PF, Deserno WM, Tabatabaei S, van de Kaa CH, et al. Noninvasive detection of clinically occult lymph-node metastases in prostate cancer. The New England journal of medicine. 2003;348(25):2491-9. Epub 2003/06/20. doi: 10.1056/NEJMoa022749. PubMed PMID: 12815134.

126.	Will O, Purkayastha S, Chan C, Athanasiou T, Darzi AW, Gedroyc W, et al. Diagnostic precision of nanoparticle-enhanced MRI for lymph-node metastases: a meta-analysis. The lancet oncology. 2006;7(1):52-60. Epub 2006/01/04. doi: 10.1016/S1470-2045(05)70537-4. PubMed PMID: 16389184.

127.	Jun YW, Lee JH, Cheon J. Chemical design of nanoparticle probes for high-performance magnetic resonance imaging. Angewandte Chemie. 2008;47(28):5122-35. Epub 2008/06/25. doi: 10.1002/anie.200701674. PubMed PMID: 18574805.

128.	Artemov D, Mori N, Okollie B, Bhujwalla ZM. MR molecular imaging of the Her-2/neu receptor in breast cancer cells using targeted iron oxide nanoparticles. Magn Reson Med. 2003;49(3):403-8. Epub 2003/02/21. doi: 10.1002/mrm.10406. PubMed PMID: 12594741.

129.	Tsourkas A, Shinde-Patil VR, Kelly KA, Patel P, Wolley A, Allport JR, et al. In vivo imaging of activated endothelium using an anti-VCAM-1 magnetooptical probe. Bioconjugate chemistry. 2005;16(3):576-81. Epub 2005/05/19. doi: 10.1021/bc050002e. PubMed PMID: 15898724.